

MICROWAVE ENABLED DISPERSION OF HIGHLY CONDUCTIVE  
CARBON NANOMATERIALS AND THEIR INTERFACIAL  
ASSEMBLIES

By

Pui Lam Chiu

A Dissertation submitted to the  
Graduate School-Newark  
Rutgers, the State University of New Jersey  
in partial fulfillment of the requirements  
for the degree of  
Doctor of Philosophy  
Graduate Program in Chemistry  
written under the direction of  
Professor Huixin He  
and approved by

---

---

---

---

Newark, New Jersey

January, 2013

**COPYRIGHT**

**©2013**

**Pui Lam Chiu**

**ALL RIGHTS RESERVED**

## **ABSTRACT OF THE THESIS**

### **Microwave Enabled Dispersion of Highly Conductive Carbon Nanomaterials and Their Interfacial Assemblies**

**By PUI LAM CHIU**

**Dissertation Director:**

**Dr. Huixin He**

Due to its phenomenal mechanical characteristics and remarkable electrical properties, graphene, a perfect single-atomic thick two-dimensional lattice carbon layer, has attracted extensive attention in nanoscience and condensed matter physics. With all the similarities, it is believed that graphene can compete with or even surpass carbon nanotubes in many fields, and it is expected to replace silicon in many electronic applications and in other advanced technologies. A single layer of graphene sheet was first isolated in 2004 from highly oriented pyrolysis graphite with Scotch tape. The invention of “The Scotch-tape” method seems very simple, and it has enabled a whole new path in many graphene-based research areas. It also resulted in Andre Geim and Konstantin Novoselov’s winning the 2010 Nobel Prize in physics. This solvent-free method

however suffers from low yields, low repeatability, and being extremely labor intensive. Solution-based fabrications have shown to be able to overcome these problems. However, the next challenge in the graphene research field and applications is the tedious chemical path that is required to convert oxidized graphene using toxic chemicals, such as hydrazine.

In this thesis, we first developed a novel and an unprecedentedly fast and simple approach to directly exfoliate graphite flakes with the aid of both nitronium ion and microwave irradiation with the aim of solving the main research problems in the field. To utilize the produced graphene in practical applications, our knowledge of interfacial science was exploited to controllably self-assemble these wonderful materials into desired structures. The research results combined with an introduction of the development and future aspects of these fields will be presented in the five chapters of this thesis.

**Chapter 1** will include a general overview of basic but important information concerning the two main carbon-based materials, carbon nanotubes and graphene. Their structures, physical properties, methods of fabrications and applications will be discussed in depth. In addition, interfacial science for self-assembly of nanomaterials will be summarized.

In **Chapter 2**, an efficient, simple and promising way to prepare graphene sheets directly from graphite flakes with the aid of nitronium ions and microwave irradiation will be presented. Knowledge of the chemistries related to nitronium

ions and microwave has enabled us to purposely omit strong oxidants, such as  $\text{KMnO}_4$ , with an aim not to heavily oxidize the materials, as many methods are based on, thus reduction reactions can be completely avoided. Experimental results demonstrate that this non-destructive method resulted in concentrated stable dispersions of flat, high-quality, conductive graphene sheets in both aqueous and organic solvents. This mildly oxidized material was extensively characterized by atomic force microscope (AFM), Infrared spectroscopy (FTIR), ultraviolet-visible spectroscopy, thermo-gravimetric analysis (TGA), X-ray photoelectron spectroscopy (XPS), Raman spectroscopy, and transmission electron microscopy (TEM).

In **chapter 3**, we extended the nitronium ions and microwave enabled dispersed approach to carbon nanotubes. Different sources of both single-walled carbon nanotubes (SWNTs) and multi-walled carbon nanotubes (MWNTs) were tested and the results showed that all the CNTs from different sources can be quickly dispersed into aqueous solutions with remarkably high concentrations compared to those of graphene solutions even though the same parameters were applied during dispersion. We found that depending on the existence of a small amount of defects from the original CNT sources, the yield, and quality of the dispersed CNTs are varied.

With a long term aim of fabricating highly transparent and conductive films to replace Indium tin oxide (ITO) in a wide variety of optoelectronic devices, in **Chapter 4**, a new method referred to as an interfacial self-assembly approach is

developed to assemble the microwave dispersed graphene and CNTs into highly conductive films. The self-assembly behavior of graphene, CNT, and a mixture of graphene and CNT with different ratios were studied separately, and the knowledge obtained was used to fabricate graphene, CNT, and a hybrid of graphene-CNT thin films at an oil/water interface, respectively. Compared to the generally used vacuum filtration method, this new approach does not need any membrane, thus theoretically any size film can be easily fabricated. To transfer the formed films to substrates for practical applications, a simple film-transferring method was also developed. The films fabricated with different film fabrication methods will also be compared and a systematic study on how the compositions of these two materials affect the performance of the final films will be summarized.

The dispersed graphene sheets are often composed with graphene sheets of different sizes, to separate them for different applications. In **Chapter 5**, interfacial self-assembly reactions were also applied to separate the graphene sheets based on their size-and electronic-dependent surface energies

**Chapter 6** will then focus on fine-tuning the surface chemistry of the graphene sheets and the oil/water ratio to efficiently emulsify the graphene sheets into core-shell capsules for drug delivery applications. Poly(*N*-isopropylacrylamide) (PNIPAA), a thermally sensitive polymer is introduced to form a temperature-sensitive and stable oil-in-water microemulsion with the ability to release the encapsulated materials in a graphene/PNIPAA shell above

its transition temperature. Experimental observations show that the emulsion with graphene has a slightly increased transitional temperature from 34 °C to 38 °C.

## **DEDICATION**

### **To my family and friends**

Thank you for all the love, patience and everything



## **ACKNOWLEDGEMENT**

I would like to express my deepest and sincerest gratitude to my research advisor, Dr. Huixin He, for all the supports, advices and encouragement that she has provided during my Ph. D. study at Rutgers I would have never been able to accomplish what I have without Dr. He's guidance.

I would like to also thank all of my committee members, Dr. Phil Huskey, Dr. Richard Mendelsohn, and Dr. Ranganathan Shashidhar, for spending their precious time and effort in criticizing and correcting my thesis.

I thank Dr. Richard Mendelsohn and his group members, especially to Dr. Guangru Mao, Yu Guo, Peter Saad, Qi Hong Zhang, and Xin Xiao for their time to work with me on the IR, Raman and to discuss and explain to me the data we got.

Also, my special thanks need to be expressed to Professor Eric Garfunkel and his group members, especially to Daniel Mastrogiovanni. I appreciate their helps in designing and conducting in XPS studies, and their interpretation.

I would also like to express my appreciation to all the faculty and staff members in our department for making my years at Rutgers more enjoyable.

Finally, but not last, I want to express my gratitude to my parents, my sister, my family, my girlfriend and my friends for their unconditional loves, supports and trusts.

## TABLE OF CONTENTS

|  |      |
|--|------|
| ABSTRACT OF THE THESIS .....   | ii   |
| DEDICATION .....   | vii  |
| ACKNOWLEDGEMENT .....  | viii |
| TABLE OF CONTENTS .....  | ix   |
| LIST OF TABLES .....   | xv   |
| LIST OF FIGURES .....  | xvi  |
| Chapter 1: Introduction .....  | 1    |
| 1.1: Research background: .....  | 1    |
| 1.1.1: Carbon and hybridization.....                                     | 1    |
| 1.2: Graphene.....   | 1    |
| 1.2.1: Discovery of graphene.....  | 1    |
| 1.2.2: Morphology of graphene.....                                       | 3    |
| 1.2.3: Properties of graphene .....                                      | 4    |
| 1.2.4: Synthesis techniques.....   | 5    |
| 1.2.4.1: Mechanical exfoliation .....                                    | 5    |
| 1.2.4.2: Epitaxial growth and CVD of graphene.....                       | 7    |
| 1.2.4.3: Liquid phase exfoliation .....                                  | 9    |
| 1.2.4.4: Unzipping carbon nanotubes to make graphene<br>nanoribbons..... | 10   |
| 1.3: Carbon nanotube:.....   | 12   |
| 1.3.1: Discovery of carbon nanotube: .....                               | 12   |
| 1.3.2: Morphology of carbon nanotube .....                               | 12   |
| 1.3.3: Electronic properties of carbon nanotubes: .....                  | 15   |

|  |    |
|--|----|
| 1.3.4: Synthesis techniques:.....  | 18 |
| 1.4: Microwave chemistry: .....  | 20 |
| 1.5: Colloids at the liquid-liquid interface: .....  | 25 |
| 1.5.1: Interfacial chemistry:.....   | 25 |
| 1.5.2: Emulsions: .....  | 25 |
| 1.5.3: Pickering Emulsion .....  | 30 |
| 1.5.4: Self-assembly of nanoparticle films: .....  | 31 |
| 1.6: Objective of the dissertation: .....  | 34 |
| 1.7: References .....  | 36 |
| Chapter 2: Microwave and Nitronium Ion Enabled Rapid and Direct<br>Production of Highly Conductive Low Oxygen Graphene ..... | 41 |
| 2.1: Introduction.....   | 41 |
| 2.2: Result and discussions:.....  | 45 |
| 2.2.1: Large area sized single-layered graphene sheets .....   | 45 |
| 2.2.2: Cutting mechanisms: .....   | 45 |
| 2.2.2.1: Longitudinal cutting:.....  | 45 |
| 2.2.2.2: Nitronium ion attack:.....  | 47 |
| 2.2.3: Colloidal nature of graphene suspensions:.....  | 51 |
| 2.2.4: Effect of physical agitation and the length of microwave<br>exposure.....   | 53 |
| 2.2.5: Optical properties and surface morphologies of ME-LOGr<br>graphene sheets:.....                                       | 55 |
| 2.2.6: Thermally stable graphene sheets.....   | 65 |
| 2.2.7: Conductive nature of graphene sheets:.....  | 67 |
| 2.3: Conclusion.....   | 70 |

|  |    |
|--|----|
| 2.4: Materials and methods: .....  | 70 |
| 2.4.1: Materials .....   | 70 |
| 2.4.2: Using microwave heating to directly produce slightly oxidized<br>graphene sheets (ME-LOGr).....                         | 71 |
| 2.4.3: Synthesis of GO .....   | 72 |
| 2.4.4: Characterizations.....  | 73 |
| 2.4.4.1: Atomic force microscopy (AFM).....  | 73 |
| 2.4.4.2: Raman spectroscopy .....  | 73 |
| 2.4.4.3: TEM .....   | 74 |
| 2.4.4.4: X-ray photoelectron spectroscopy (XPS) and<br>Rutherford backscattering spectroscopy (RBS).....                       | 74 |
| 2.4.4.5: Thermogravimetric Analysis (TGA).....   | 75 |
| 2.4.4.6: Optical and electrical properties of dispersed<br>graphene sheets.....  | 76 |
| 2.4.4.7: SEM and STEM .....  | 76 |
| 2.5: References: .....   | 78 |
| Chapter 3: Extension of microwave and nitronium ion chemistry to directly<br>disperse highly conductive carbon nanotubes ..... | 85 |
| 3.1: Introduction .....  | 85 |
| 3.2: Results and discussion: .....   | 87 |
| 3.2.1: Optical characterizations (Coloration and UV-Vis).....  | 87 |
| 3.2.2: Thermal stabilities and purities .....  | 90 |
| 3.2.3: XRD for structural information .....  | 93 |
| 3.2.4: Raman spectroscopy .....  | 95 |
| 3.2.5: XPS for surface functionalization .....   | 98 |

|  |     |
|--|-----|
| 3.3: Conclusion:.....  | 98  |
| 3.4: Materials and Methods: .....  | 99  |
| 3.4.1: Materials: .....  | 99  |
| 3.4.2: Methods:.....   | 100 |
| 3.4.2.1: Synthesis of carbon nanotube .....  | 100 |
| 3.4.2.2: Characterizations:.....   | 100 |
| 3.5: References: .....   | 102 |
| Chapter 4: Self-assembled thin films of graphene and graphene/CNT<br>composites for electronics applications ..... | 106 |
| 4.1. Introduction:.....  | 106 |
| 4.2. Result and discussion:.....   | 107 |
| 4.2.1. Current issues with film preparations.....  | 107 |
| 4.2.2: Surface active nature of ME-LOGr graphene sheets....  | 112 |
| 4.2.3: Self-assembly of graphene thin film at a liquid/liquid interface<br>with ethanol as an inducer .....        | 113 |
| 4.2.4. Development of a simpler but better film transfer method  | 117 |
| 4.2.5. Comparison between films prepared by vacuum filtration and<br>by interfacial self-assembly .....            | 120 |
| 4.2.6. Graphene/Carbon nanotube composite films for superior<br>performance .....                                  | 121 |
| 4.2.7. Direct visual evidence of graphene/carbon nanotube<br>crosslinking.....                                     | 123 |
| 4.3. Conclusion:.....  | 127 |
| 4.4. Materials and methods: .....  | 127 |
| 4.4.1. Materials: .....  | 127 |
| 4.4.2. Synthesis of graphene (ME-LOGr) .....   | 128 |

|  |     |
|--|-----|
| 4.4.3. Synthesis of carbon nanotube .....  | 128 |
| 4.4.4. Graphene and graphene/CNT hybrid film via filtration ...  | 129 |
| 4.4.5. Self-assembly of graphene and graphene/CNT hybrid thin<br>films .....   | 129 |
| 4.4.6. Characterizations.....  | 130 |
| 4.5: References: .....   | 131 |
| Chapter 5: Size-dependent separation of graphene sheets .....  | 135 |
| 5.1. Introduction:.....  | 135 |
| 5.2. Results and discussion:.....  | 137 |
| 5.2.1. Self-separation in biphasic systems .....   | 137 |
| 5.2.2. Raman spectroscopy .....  | 139 |
| 5.2.3: Scanning electron microscopy (SEM).....   | 141 |
| 5.2.4. Size- and oxidation-dependent separation of graphene<br>sheets.....   | 143 |
| 5.3. Conclusion:.....  | 148 |
| 5.4. Materials and methods: .....  | 148 |
| 5.4.1. Materials: .....  | 148 |
| 5.4.2. Methods:.....   | 149 |
| 5.4.2.1. Synthesis of graphene .....   | 149 |
| 5.4.2.2. Interfacial separation of graphene .....  | 149 |
| 5.4.2.3. Characterizations:.....   | 150 |
| 5.5. References: .....   | 151 |
| Chapter 6: Thermally-responsive liquid-filled PNIPAM/graphene microsphere<br>via self-assembly by O/W emulsion for drug delivery applications. 154 |     |
| 6.1: Introduction.....   | 154 |

|  |     |
|--|-----|
| 6.2: Result and discussion:.....   | 155 |
| 6.2.1: Amphiphilicity of ME-LOGr at an oil-water interface .....   | 155 |
| 6.2.2: Effect of sonication .....  | 160 |
| 6.2.3: Modifying graphene with PNIPAM for improvement in stability<br>and thermal-controllability.....           | 162 |
| 6.2.4: Physical composition and morphological structures of<br>microspheres .....                                | 165 |
| 6.2.5: Thermal Controlled release study .....  | 169 |
| 6.3: Conclusion: .....   | 172 |
| 6.4: Materials and Methods: .....  | 173 |
| 6.4.1: Materials: .....  | 173 |
| 6.4.2: Methods: .....  | 173 |
| 6.4.2.1: Synthesis of graphene .....   | 173 |
| 6.4.2.2: Synthesis of PNIPAM/graphene composite via<br>EDC/NHS coupling reaction .....                           | 174 |
| 6.4.2.3: The preparation of O/W emulsion.....  | 174 |
| 6.4.2.4: Optimization of emulsion formations.....  | 175 |
| 6.4.2.5: Enhanced stability of graphene emulsion by<br>crosslinking with PNIPAM.....                             | 175 |
| 6.4.2.6: Characterization of morphological O/W emulsion<br>microstructure:.....                                  | 175 |
| 6.4.2.7: Characterization of thermo-responsive behaviors of<br>the composites and controlled release experiment. | 176 |
| 6.5: References: .....   | 178 |
| CURRICULUM VITA .....  | 181 |

## LIST OF TABLES

|   |     |
|---|-----|
| <b>Table 1.1:</b> Boiling point, dielectric constant, $\tan \delta$ , and dielectric loss ( $\epsilon''$ ) for 9 common solvents (measured at room temperature and 2450 MHz)..... | 21  |
| <b>Table 1.2:</b> A short list of typical mechanical methods in preparing emulsions. ...  | 27  |
| <b>Table 5.1:</b> List of positions of D band and G bands, and their ratios with various toluene-to-water (T:W) ratios.....   | 141 |
| <b>Table 5.2:</b> A summary of several square graphene species with various thicknesses and sizes, and their corresponding surface areas. ....                                    | 146 |



## LIST OF FIGURES

**Figure 1.1:  $sp^2$  hybridization of in carbon materials and their main forms. a)**

Three  $sp^2$  hybridized orbitals (in red) are in-plane with 2p orbitals perpendicular to the plane;  $\pi$  and  $\pi^*$  are the bonding and anti-bonding orbitals, respectively. b) Three different carbon-based materials: fullerene (left), carbon nanotube (center), and graphite (right), and graphene is the basic building block. .... 2

**Figure 1.2: A schematic showing the 1-D graphene hexagonal lattice. In**

such lattice, carbon atoms (filled circles) are about 0.142 nm away from each other. .... 3

**Figure 1.3: Energy dispersion of graphene..... 5**

**Figure 1.4: Microscope image of successful transfer of graphene from**

**HOPG onto a 300 nm  $SiO_2/Si$  substrate.** A number of layers can be identified by the contrast in color of the image. A single layer of graphene should have a faint violet-blue color. The color shifts to blue as the thickness increases. From [13]. Reprinted with permission from AAAS. .... 6

**Scheme 1.1: A chemical mechanism of cleavage of the carbon  $sp^2$  network.**

A defect bearing a manganate ester is first created on the sidewall of the carbon  $sp^2$  network in a permanganate oxidative environment. This defect can further oxidize in the dehydrating oxidative medium to form a dione species. The juxtaposed ketones cause a strong steric hindrance that

distorts the  $\beta,\gamma$ -alkenes (marked as red), making them severely more prone to the attacks by permanganate. After consecutive attacks, the  $sp^2$  network is eventually cleaved. .... 11

**Figure 1.5. Morphologies of carbon nanotubes.** a) A carbon nanotube can be technically viewed as a cylinder made up of a rolled up sheet of graphene. b) Schematic drawings of a single-walled carbon nanotube (SWNT) (left), and a multi-walled carbon nanotube (right). .... 13

**Figure 1.6: An unrolled honeycomb lattice crystal structure of carbon nanotubes.** This figure shows the structural relation between a graphene sheet and different potential types of carbon nanotube which can be formed if it is rolled up. The vectors  $\mathbf{a}_1$  and  $\mathbf{a}_2$  are the basis pair that defines the chiral vector  $\mathbf{C}_h = n\mathbf{a}_1 + m\mathbf{a}_2$ , where  $(n, m)$  is an integer pair. Every value of  $\mathbf{C}_h$  gives rise to a unique carbon nanotube. .... 14

**Figure 1.7:** a) Brillouin zone of a graphene unit cell (top). Dashed lines are the allowed wavevectors (electronic states) of two different carbon nanotubes: a metallic  $(5, 5)$  (left) and a semi-conducting  $(5, 4)$  (right) and are superimposed onto the graphene Brillouin zone to illustrate that the  $K/K'$  points are allowed in the  $(5, 5)$  metallic nanotube, while the  $K/K'$  points are forbidden in the  $(5, 4)$  semi-conducting nanotube. b) Plots of the density of states (DOS) for a metallic armchair  $(5, 5)$  SWNT, and for a semi-conducting chiral  $(5, 4)$  SWNT. .... 17

**Figure 1.8: Visualizations of carbon nanotube growth mechanisms by CVD.**

Typically, carbon nanotubes are grown by the precipitation of saturated carbon pyrrolyzed from carbon sources ( $C_xH_y$ ) at elevated temperatures. Depending on the interaction between the catalyst particles and the substrate, carbon nanotubes can grow in two mechanisms: top growth (a) and base growth (b)..... 19

**Figure 1.9: Microwave irradiation frequency range relative to electron**

**energy and wavelengths on electromagnetic spectrum.** Red shadow shows the full range of microwave irradiation in the frequency of 0.3 to 3 GHz, which lies between infrared and radio frequencies..... 20

**Figure 1.10: Schematic of microwave irradiation wave showing electric and**

**magnetic fields.** Reproduced from Practical Microwave Synthesis of Organic Chemists. Wiley-VCH, Weinheim, 2009..... 22

**Figure 1.11: Schematic of the difference of heating mechanisms between**

**conventional heating (left) and microwave heating.** With conventional heating (left), such as heating mantles and hot baths, temperature on the side surface of the vessel is greater than the internal temperature. With microwave heating (right), the microwave-absorbing reagents and solvents convert microwave irradiation into heat, and create localized superheating. .... 23

**Figure 1.12: Temperature gradients in microwave versus oil-bath heating. Same**

**substance after 1 minute of microwave irradiation (left) compared to**

treatment in an oil-bath (right). Microwave heating simultaneously raises the temperature of the entire volume, while the vessel wall is heated first in the oil-bath-heated with the internal temperature being not affected. Temperature scales in Kelvin. Reproduced from Practical Microwave Synthesis for Organic Chemists. *Wiley-VCH, Weinheim*, 2009..... 24

**Figure 1.13: Two major types of emulsion.** Oil-in-water (O/W) emulsion and water-in-oil (W/O) emulsion ..... 29

**Figure 1.14:** Most important mechanisms of the degradations of emulsion from a good emulsion (top middle): a) creaming; b) Ostwald ripening; c) breaking; d) flocculation; e) coalescence. .... 31

**Figure 1.15:** Gold nanoparticle monolayer. Micrograph of a monolayer formed by 6-nm gold nanocrystals. Reprinted by permission from Macmillan Publishers Ltd: [Nature Materials] (55), copyright (2006). .... 33

**Figure 2.1:** (a) Schematic drawing shows the proposed oxidation mechanism to directly produce highly conductive low oxygen containing amphiphilic graphene sheets. A nitronium ion forms a single electron transfer (SET) intermediate with a graphene layer, which is intercepted by a rapid oxygen transfer from molecular oxygen, affording an epoxy group; or from  $\text{NO}_2^+$  to form an OH group..... 43

**Figure 2.2:** a) FE-SEM image of a large graphene sheet deposited onto a  $\text{SiO}_2/\text{Si}$  substrate. b) STEM image of a graphene sheet deposited onto a holey carbon film on Cu from the same graphene dispersion. c) A magnified

|   |    |
|---|----|
| image of the circled area in figure 2.2b showing a side of a large graphene sheet.....  | 50 |
| <b>Figure 2.3:</b> Digital photographs of stable ME-LOGr solution in water and in DMF.  |    |
| The clear Tyndall effect from both solutions indicated the colloidal characteristic of these solutions. Figure 2.3a, ME-LOGr aqueous solution, Figure 2.3b and c are ME-LOGr in DMF.....  | 51 |
| <b>Figure 2.4:</b> Rrepresentative AFM images of ME-LOGr and GO. (a)ME-LOGr via bath sonication; (b) graphene oxide prepared by Hummer’s method; (c) ME-LOGr prepared by magnetic stirring. The arrows in figure (b) indicate foldings and wrinkles. The height profiles are shown in red lines in each image.....  | 53 |
| <b>Figure 2.5:</b> shows an AFM image of small graphene sheets obtained with 60 seconds of microwave irradiation. ....  | 55 |
| <b>Figure 2.6:</b> UV-Vis spectra of ME-LOGr (red) and GO (black). Inset: a digital photo showing the different colorations of ME-LOGr and GO solution in water.....  | 56 |
| <b>Figure 2.7:</b> A UV-Vis spectrum and digital photograph of the graphene solution obtained by adding a small amount of $\text{KMnO}_4$ in the mixture of $\text{H}_2\text{SO}_4/\text{HNO}_3$ . The $\lambda_{\text{max}}$ at 245 nm indicates that this material is heavy oxidized during the 30 seconds of microwave irradiation. The brownish yellow color indicates a high-degree of functionalization of the graphene surface. .... | 57 |

**Figure 2.8:** Raman spectra of ME-LOGr (red) and GO (black). The small intensity ratio of D/G bands and the high intensity of 2D in ME-LOGr are in contrast to the larger D/G band ratio and the absence of 2D band in GO, indicating ME-LOGr has more ideal graphitic structures without adsorbents induced surface modification. .... 58

**Figure 2.9:** A representative HRTEM image of ME-LOGr, which is consisted of many different crystalline-like domains with average lateral size of 6-10 nm, there is no nanometer sized holes was observed, which is in highly contrast to GO and rGO. The size of crystalline domains is also much larger than those observed in GO and rGO. b) Fast Fourier transform (FFT) pattern of the selected region, indicated in a). c) The reconstructed image of the same spot as b) after filtering with the frequency domain to include contributions from both sets of hexagons of the FFT pattern. The scale bar in (a) is 5 nm. .... 59

**Figure 2.10:** a) and b) show HRTEM images of a ME-LOGr sheet at two different positions. 1-6 are a series of reconstructed high-resolution images at different positions, as indicated by red boxes in figure S6b. The reconstructed images were obtained by filtering with the frequency domain to include contributions from both sets of hexagons of their respected FFT patterns. .... 60

**Figure 2.11:** Carbon 1s core XPS spectra for thin films of (a) ME-LOGr and (b) GO. The content of oxygen-free carbon of ME-LOGr was 79% which was

comparable with the reported value of fully reduced GO, while GO (b) contains only 49% of oxygen-free carbon. This is a direct evidence of much less oxidation in the ME-LOGr..... 62

**Figure 2.12:** ATF-FTIR spectra of ME-LOGr (red) and GO (black) showing that small amount of epoxy and hydroxyl groups in ME-LOGr, while GO is heavily decorated with a variety of oxygen-containing groups..... 64

**Figure 2.13:** (a) TGA curves of % weight loss plotted against temperature, showing that ME-LOGr (red) is thermally much more stable than GO (blue), and highly comparable with its parent graphite (black). (b) Percolation study of ME-LOGr and GO using a 4-point probe setup. After percolation threshold, the sheet resistivity of ME-LOGr (red) shows 5 orders of magnitude lower than the heavily oxidized GO films. .... 66

**Figure 3.1:** Photographs of microwave-enabled dispersions of different types of carbon nanotubes. a) HiPco single-walled carbon nanotubes, b) CNANO-single-walled carbon nanotubes, and c) CNANO multi-walled carbon nanotubes..... 87

**Figure 3.2:** UV-Vis spectra of aqueous dispersions of different types of HiPco single-walled carbon nanotubes (black), CNANO-single-walled carbon nanotubes (red), and CNANO multi-walled carbon nanotubes (blue)..... 88

**Figure 3.3:** TGA mass loss of three different carbon nanotubes: HiPco-SWNT (blue), CNANO-MWNT (black) and CNANO-SWNT (red). When the

|  |     |
|--|-----|
| pyrolysis was completed, HiPco-SWNT had about 18% of catalyst residual mass of remaining, .....  | 91  |
| <b>Figure 3.4:</b> X-ray spectra of HiPco (red), CNANO-SWNT (blue) and CNANO-MWNT (green).....   | 94  |
| <b>Figure 3.5:</b> Raman spectra of non-treated CNANO-MWNT (red), CNANO-SWNT (blue) and HiPco-SWNT (black), in powder form.....  | 95  |
| <b>Figure 3.6:</b> As collected Raman spectra of microwave treated CNANO-MWNT (red), CNANO-SWNT (blue) and HiPco-SWNT (black). All spectra were collected on dried products obtained after the microwave reactions. b) Spectra of CNANO-MWNT (red) and CNANO-SWNT (blue) were zoomed in 70 times, indicating that the signals from these samples were much lower than HiPco-SWNT. .... | 96  |
| <b>Figure 3.7:</b> Carbon 1s core XPS spectra for thin films of microwave treated dispersions of (a) CNANO-MWNT b) CNANO-SWNT and c) HiPco-SWNT. The content of oxygen-free carbon of CNANO-MWNT and CNANO-SWNT were comparable at 74% and 75%, respectively; while the content in HiPco-SWNT decreased to 70%. ....   | 97  |
| <b>Figure 4.1:</b> Three common film deposition methods used to fabricate thin films and their major drawbacks. ....   | 108 |
| <b>Scheme 4.1:</b> Schematic of the procedures involved in transferring a graphene film collected via vacuum filtration on an alumina membrane unit to a submerged substrate.....  | 109 |



|   |     |
|---|-----|
| <b>Figure 4.2:</b> photograph of a successful transfer of a graphene film on to a quartz substrate.....   | 110 |
| <b>Figure 4.3:</b> Digital photographs of two different attempts in fabricating graphene films on the filter membranes. It is obvious that the reproducibility of this filtration method is not perfect. ....   | 111 |
| <b>Figure 4.4:</b> A Top-view digital photograph of a ME-LOGr aqueous suspension<br>Some surface –active graphene sheets can be clearly seen at the air-water interface.....  | 112 |
| <b>Scheme 4.2:</b> Illustration of the steps involved in the interfacial self-assembly using ethanol as an inducer. Ethanol reduces the charge density of graphene, promoting self-assembly at the toluene/water interface, by forming hydrogen bonds with $-\text{COO}^-$ and $-\text{OH}$ groups on the graphene surface..... | 114 |
| <b>Figure 4.5:</b> Digital photographs of: (left) ME-LOGr suspension with toluene added and the same system with (from top to bottom) 1 mL, 2 mL and 5 mL of additional ethanol. ....   | 115 |
| <b>Figure 4.6:</b> a schematic drawing (left) depicting a similar “pull-up” technique similar to that in LB film deposition and a digital photograph (right) of an incomplete film transfer of a self-assembled film onto a glass substrate..   | 118 |
| <b>Figure 4.7:</b> Illustration of a film deposition on to a submerged substrate utilizing a syringe pump for slow but constant rate of removal the solvents .....  | 119 |

|   |     |
|---|-----|
| <b>Figure 4.8:</b> A plot of % transmittance of films formed by the vacuum filtration method (black) and by self-assembly (red).....  | 121 |
| <b>Figure 4.9:</b> A plot of sheet conductance of the hybrid films as a function of the weight percentage of microwave-dispersed CNANO-MWNT. ....   | 122 |
| <b>Figure 4.10:</b> SEM images of hybrid films deposited on alumina membrane with a weight ratio of (ME-LOMWNTs/ME-LOGr): (a)25/75, (b)50/50, and (c)90/10. (d) A SEM image of a bare alumina membrane. ....  | 123 |
| <b>Figure 4.11:</b> A series of representative SEM images showing crosslinking (in red circles) in carbon nanotube and graphene hybrid films. ....  | 124 |
| <b>Figure 4.12:</b> (Left) illustrations of the 1D and 2D electron transfer pathways for carbon nanotubes (top) and graphene (bottom).(Right) Huge contact resistances are caused by the gaps between two carbon nanotubes (top) and different layers in graphene (bottom).....   | 125 |
| <b>Scheme 4.2:</b> A possible mechanism of Fisher esterification for the crosslinking in the carbon nanotube and graphene hybrid films. ....  | 126 |
| <b>Scheme 5.1:</b> Schematic depicting a single suspension consists of graphene with various lateral sizes and thicknesses. ....  | 136 |
| <b>Figure 5.1:</b> A digital photograph of graphene suspension and toluene bi-phasic system after being vigorously mixed, showing three main regions: I) a clear graphene suspension in the aqueous phase, II) an organic phase with some visible bubbles in millimeter scale and III) a thick film of graphitic materials creeping up to the walls of the containers. .... | 138 |

|  |     |
|--|-----|
| <b>Figure 5.2:</b> A zoomed in digital photograph of region II in figure 5.1, showing large emulsion at the toluene/water interface. ....  | 139 |
| <b>Figure 5.3:</b> Raman spectra of different graphene samples after separations with biphasic systems prepared with different toluene/water ratios .....  | 140 |
| <b>Figure 5.4:</b> SEM images of (a) the thick film formed on the sidewalls of the glass test tube. b) a high magnification image of the area in the red box, showing a uniform film was underneath the unreacted graphite particles, and c) a spot on the sample consisting only large unreacted graphite particles.....  | 142 |
| <b>Figure 5.5:</b> a) A SEM image of the stable solution after mixing in the aqueous phase, showing no big unreacted graphite particles. b) A distribution plot for of the lateral sizes of the graphene sheets in a). ....  | 143 |
| <b>Figure 5.6:</b> Illustrations of two same-size graphene sheets with different oxidation state, thus different amount of oxygen-containing groups on the surfaces.....   | 145 |
| <b>Figure 6.1:</b> Digital photographs of a) two trials of emulsion formation experiments with varied phase volume ratios done in parallel after a gentle mixing by vortex for 2 hours, and b) emulsion formed at 4:1 (water:toluene) ratio, showing stable and small emulsion bubbles at the toluene/water interface..... | 157 |
| <b>Figure 6.2:</b> Effect of pH in emulsion formation.....   | 159 |
| <b>Scheme 6.1:</b> Two proposed mechanisms of the formation of stable graphene microspheres in aqueous ammonia.....  | 160 |

|   |     |
|---|-----|
| <b>Figure 6.3:</b> Digital photographs showing the effect of the use of sonication for stable emulsion synthesis.....   | 161 |
| <b>Figure 6.4:</b> (left) A light micrograph of the emulsion stabilized by graphene; b) a plot of the distribution of sizes of the emulsion shown on the left .....   | 162 |
| <b>Scheme 6.2:</b> Schematic showing the coupling of PNIPAM polymer onto the – COOH groups on the edge of graphene via EDC/NHS coupling reaction.   | 163 |
| <b>Figure 6.5:</b> Emulsion prepared using ultrasonication at pH 13 .....   | 164 |
| <b>Figure 6.6:</b> (Left) Regular optical image and (right) a typical fluorescence microscopic images of the emulsion microspheres. It clearly demonstrates a strong fluorescent signal from the microsphere cores, suggesting the encapsulation of the Oil Blue N dyed toluene ..... | 165 |
| <b>Figure 6.7:</b> a SEM image of the sample prepared by dropping and vacuum drying a volume of 10 uL of the emulsion on a Si substrate. ....   | 166 |
| <b>Figure 6.8:</b> A typical phase diagram .....  | 167 |
| <b>Figure 6.9:</b> Photograph of the home-built freeze-drying apparatus.....  | 168 |
| <b>Figure 6.10:</b> SEM images of the freeze-dried graphene-polymer sample,.....  | 169 |
| <b>Figure 6.11:</b> a series of light microscopic images of PNIPAM-only emulsion obtained at different temperatures.....  | 170 |
| <b>Figure 6.12:</b> (Top) Fluorescence images of a PNIPAM/graphene microsphere, and (bottom) their corresponding light microscopic images at different temperatures. ....   | 172 |

## Chapter 1: Introduction

### 1.1: RESEARCH BACKGROUND:

#### 1.1.1: Carbon and hybridization

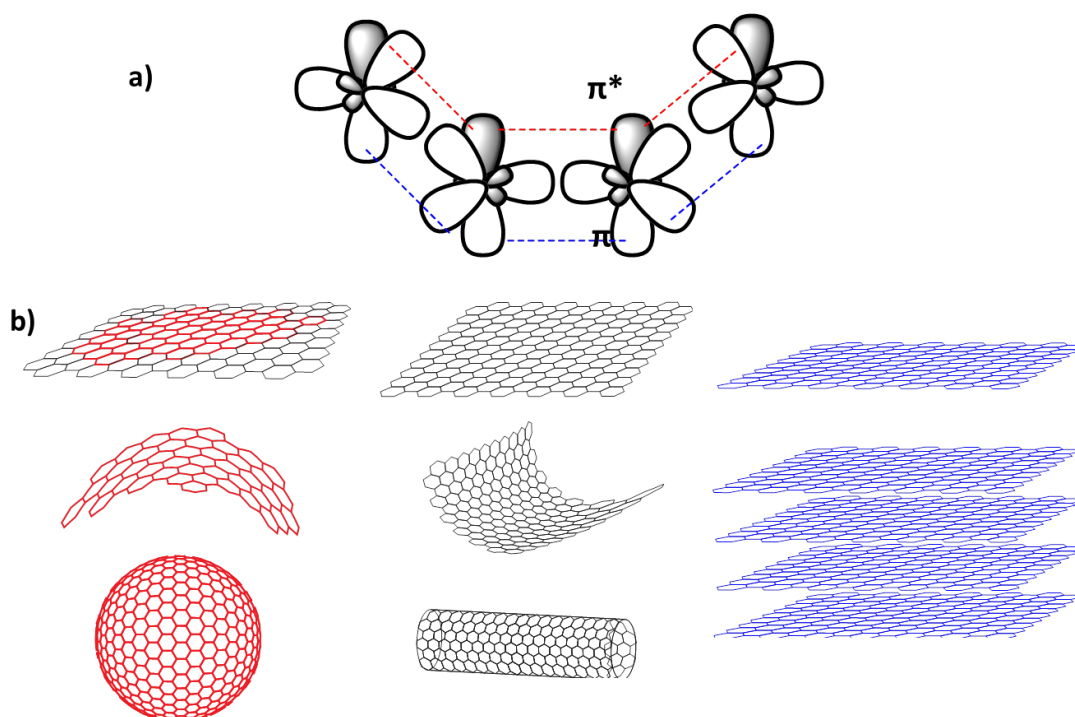
Carbon is the sixth element in the periodic table and it has six electrons that occupy  $1s^2$ ,  $2s^2$ , and  $2p^2$  atomic orbitals. Three forms of hybridization can occur: 1)  $sp$  (in  $C_2H_2$ ), 2)  $sp^2$  (in graphite), and 3)  $sp^3$  (in  $CH_4$ ). The capability to have multiple hybridizations makes carbon special in its group in the periodic table. Extremely stable nanomaterials which consist of only  $sp^2$  materials (see figure 1.1), such as fullerenes[1], carbon nanotubes[2] and graphene[3], have stimulated a wide range of research. In this thesis, the focus will be mainly on graphene and carbon nanotubes.

### 1.2: GRAPHENE

#### 1.2.1: Discovery of graphene

The very first graphene was synthesized by chemical vapor deposition on metal platinum substrate in 1968 by Morgan and co-workers[4]. Harmed by the lack of reproducibility and the impossibility to transfer the produced graphene onto different substrates, this synthetic process was eventually abandoned. In 1975, Bommel and co-workers[5] also reported a process of epitaxial sublimation of silicon from silicon carbide (0001) to synthesize graphene. However, no further characterization or investigation was performed. Even though graphite crystals are extremely stable and inert in different environments, it was believed both

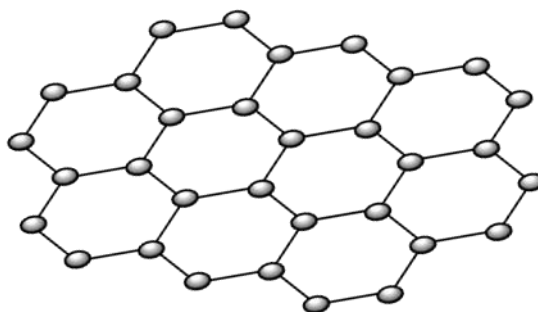
theoretically and experimentally that graphene would be thermodynamically unstable at finite temperatures when the crystal was just a few layers thick[6]. The melting temperature of thin films rapidly decreases as the thickness decreases. At just a few layers thick, they become unstable and either segregate into islands or decompose[7, 8]. 2-D materials like graphene were believed not to exist until 2004 when the theory was disproved by the discoveries of graphene by Novoselov et al.[3] This will be discussed in detail in following sections.



**Figure 1.1: sp<sup>2</sup> hybridization of in carbon materials and their main forms.** a) Three sp<sup>2</sup> hybridized orbitals (in red) are in-plane with 2p orbitals perpendicular to the plane;  $\pi$  and  $\pi^*$  are the bonding and anti-bonding orbitals, respectively. b) Three different carbon-based materials: fullerene (left), carbon nanotube (center), and graphite (right), and graphene is the basic building block.

### 1.2.2: Morphology of graphene

Graphene is a mono-layer planar sheet consisting of only  $sp^2$ -bonded carbon atoms that are tightly packed into a two-dimensional honeycomb crystal lattice[9]. A schematic showing the 1-D graphene lattice is shown in figure 1.2. The carbon bond length in graphene is about 0.142 nm. Due to this highly conjugated carbon network, graphene has shown excellent mechanical, electrical, thermal and optical properties. When graphene layers stack together on top of each other, bulk graphite is formed (see figure 1.1b right) with an inter-planar spacing of 0.335 nm. These layers are loosely bonded to each other via van der Waals, thus graphene can be extracted from bulk graphite crystal by mechanical or chemical exfoliation.



**Figure 1.2: A schematic showing the 1-D graphene hexagonal lattice.** In such lattice, carbon atoms (filled circles) are about 0.142 nm away from each other.

### 1.2.3: Properties of graphene

It is important to understand that only  $\pi$  electrons can contribute to electronic transport in such  $sp^2$ -hybridized system; hence the above energy dispersion described as the electronic band structure of graphene can be plotted in the Brillouin zone using equation 1.2 (as shown in figure 1.3). The upper half of the energy curve describes anti-bonding ( $\pi^*$ ) orbital, while the lower part describes the bonding ( $\pi$ ) orbital. One of the most striking features of graphene is that  $\pi$  and  $\pi^*$  bands are degenerate at the K points in the Brillouin zone, through which Fermi energy passes. Due to the symmetry requirements of two equivalent carbon atoms in the unit cell of the hexagonal lattice, P.R. Wallace identified that graphene possessed a zero gap at the K point (between the conduction and valence bands), making it a zero band gap semiconductor[10]. Nearly 40 years later, DiVincenzo and Mele reported their discovery of the linear dispersions of the electronic band structure near the K-point of graphene has zero mass of the charge carriers[11]. Using a well-established mathematical expression:

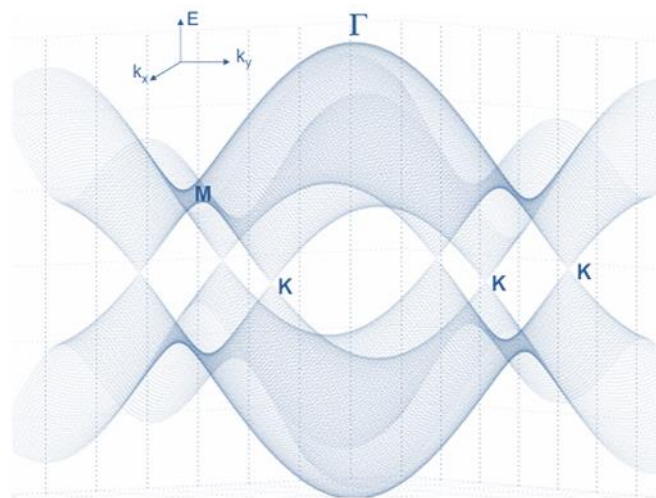
$$\omega(\vec{k}) = \sqrt{|f(\vec{k})|^2} = \sqrt{1 + 4 \cos \frac{\sqrt{3}k_x a}{2} \cos \frac{k_y a}{2} + 4 \cos^2 \frac{k_y a}{2}}$$

one can fit the theoretically calculated band structure. Figure 1.3 shows a typical calculated electronic band structure of graphene  $\pi$ -bands. It is clear that the upper anti-bonding  $\pi^*$ -band and the lower bonding  $\pi$ -band touch at the K-point and render graphene a semiconductor with zero band gap.



### 1.2.4: Synthesis techniques

It is surprising that we actually make graphene when we write with pencils, which is basically graphite, by cleaving it with the friction between the graphite and the paper. We indeed understand that fabricating graphene is not at all that difficult; however the challenging part is the isolation of these nanostructures in large scale in order to study their properties.

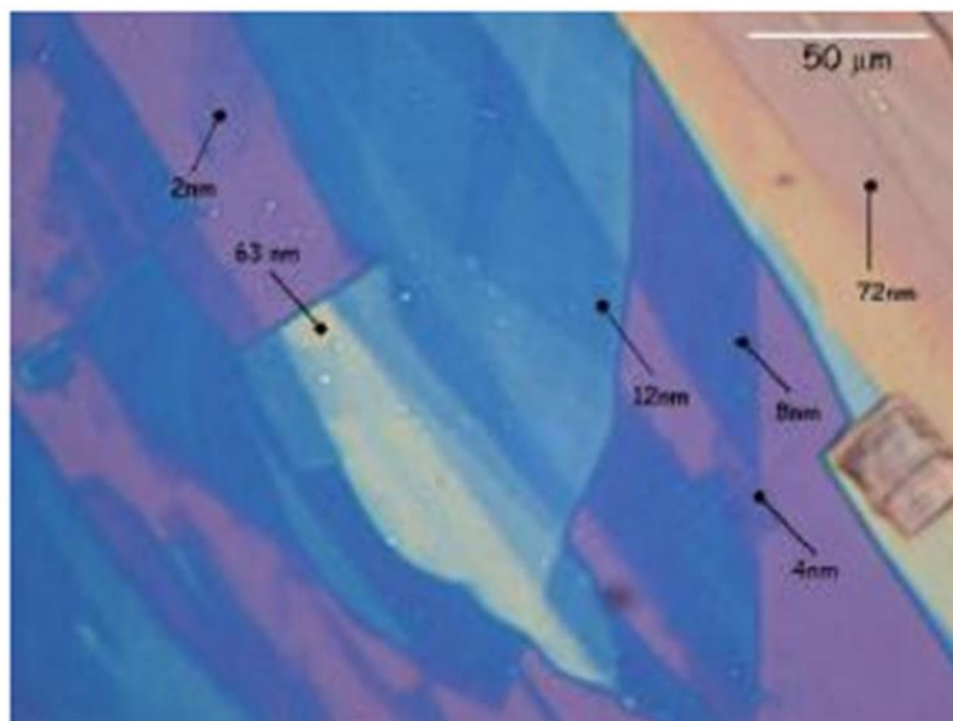


**Figure 1.3:** Energy dispersion of graphene.

#### 1.2.4.1: Mechanical exfoliation

There are several mechanical methods for graphene synthesis. The most important method, a more repeatable process for yielding pristine graphene was reported in 2004 by Novoselov et al.[3], through mechanical cleavage (Scotch tape method) of highly-orientated pyrolytic graphite (HOPG) and other atomic crystals[12]. This technique requires repeated sticking and peeling of the HOPG

with scotch tape until thin sheets of graphene are obtained. The last step involves gentle rubbing of the tape with thin graphene sheets on top of any desired substrates with some soft matters to prevent damaging the graphene flakes, and the tape is finally removed carefully. However, the graphene sheets were never physically observed until the discovery that monolayers of graphene gave a visible good optical contrast when they were deposited onto a 300 nm  $\text{SiO}_2/\text{Si}$  substrate (see figure 1.4)[13]. The isolation of single sheet combined with



**Figure 1.4: Microscope image of successful transfer of graphene from HOPG onto a 300 nm  $\text{SiO}_2/\text{Si}$  substrate.** A number of layers can be identified by the contrast in color of the image. A single layer of graphene should have a faint violet-blue color. The color shifts to blue as the thickness increases. From [13]. Reprinted with permission from AAAS.

the visibility of graphene have enabled significant amount of research about this wonderful material. Another mechanical exfoliation method is first to intercalate graphite with lithium ions. When water is added, it is quickly converted into hydrogen gas by the intercalated lithium ions, which expands and exfoliates the graphite particles into layers of graphene[14].

#### **1.2.4.2: Epitaxial growth and CVD of graphene**

Epitaxial growth is another notable method in fabricating graphene sheets, since the electronic band-structure of graphene was first studied in this material. The growth of graphene on hexagonal substrates is often referred as epitaxial growth. SiC epitaxial graphene has been one of the most extensively studied structures. A typical epitaxial growth of graphene requires SiC to be annealed to high temperatures ( $>1250\text{ }^{\circ}\text{C}$ ) in either ultra-high vacuum[5] or inert atmospheres[15]. The main mechanism of forming graphene at such high temperatures is the evaporation of silicon from SiC off the surface leaving behind a surface enriched with carbon, which gives rise to the growth of high quality graphene layers. The size and quality of the fabricated graphene have been reported to be easily controllable.

The first epitaxial growth of graphene was reported by de Heer et al at the Georgia Institute of Technology, [16, 17] in which the graphene was a product from the high temperature reduction of silicon carbide at around  $1000\text{ }^{\circ}\text{C}$  in

ultrahigh vacuum. A number of literatures have reported that the differences in the physical properties between epitaxially grown and mechanically exfoliated graphene are due to the influence of surface dependence on silicon carbide substrates and several other growth parameters.[16, 18]

Another substrate-based growth method for graphene is by chemical vapor deposition (CVD) onto transition metal films. Recent reports of successful growth of graphene on relatively inexpensive CVD substrates have encouraged the optimization of CVD conditions for large-area growths.[19-21] Graphene grown on polycrystalline Ni exhibits electron mobility of  $\sim 3650 \text{ cm}^2\text{V}^{-1}\text{S}^{-1}$  and quantum Hall effects. However, the growth of graphene on Ni has been limited to the size (graphene can grow up to a few to tens of microns regions) and by the lack of control over the number of layers at grain boundaries.[20] In contrast to Ni, uniform high quality of single-layered graphene has been repeatedly reported on polycrystalline copper substrates.[22] Imaging and various analyses confirmed 95% single-layered graphene coverage with a single Cu foil as the substrate. Currently the most economically available graphene by CVD is graphene on Cu.

In theory, both epitaxial and CVD growths of graphene have the potential of yielding a single-layered graphene sheet over the entire substrate. This may be the easiest method to incorporate the material into many current semiconductor applications. Despite the high quality of graphene obtained with these deposition methods, the cost of the base materials and the strong interaction between formed graphene and the supporting substrates have always

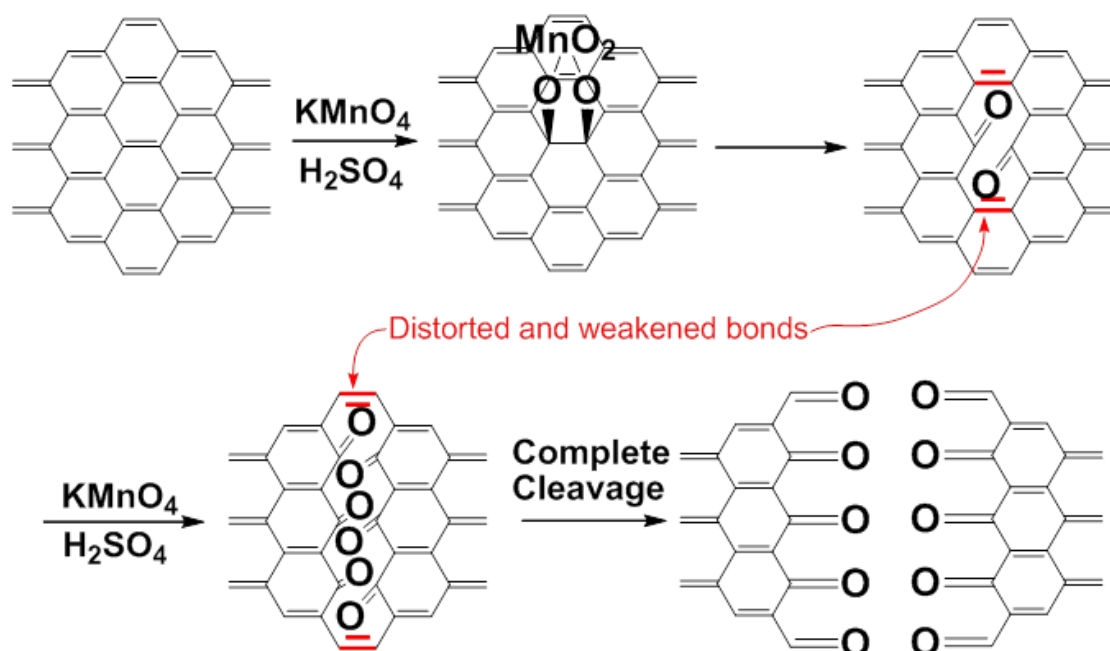
been the major drawbacks. Without the possibility of transferring the grown graphene on to other insulating substrates, such as plastic foils, glass or  $\text{SiO}_2/\text{Si}$ , it is difficult to incorporate it to many electronic applications.

#### **1.2.4.3: Liquid phase exfoliation**

Hernandez et al.[23] have recently reported that graphene can be exfoliated in a small number of solvents such as *N*-methylpyrrolidone (NMP). They made dispersions of graphene by sonication. After sonication, a grey solution was obtained which contains a homogeneous phase with a large number of macroscopic particles precipitated on the bottom of the containers. They observed that after a longer period of time, the suspensions that had the least amount of sedimentation remained the most stable suspensions. They proposed that the successful dispersions of graphite in the solvents are governed by the difference in the net gain in enthalpy within the systems, which depends on the surface energies of graphene and the solvents. The surface energy is defined as the energy required overcoming the van der Waals force between two layers of graphene. Similar experiments were conducted by Coleman and co-workers, in which they dispersed graphite in other solvents known to disperse carbon nanotubes, such as Benzyl Benzonate,  $\gamma$ -Butyrolactone and *N,N*-Dimethylacetamide. Each suspension was studied by the fraction of graphite/graphene remaining after centrifugation. The main drawback of this method in fabricating graphene sheet is that the size of the graphene sheets cannot be controlled.

#### 1.2.4.4: Unzipping carbon nanotubes to make graphene nanoribbons

Recently, long but narrow graphene-based nanoribbons have been made by selectively longitudinally unzipping carbon nanotubes by different approaches.[24-26] The easier and more applicable method is to treat multi-walled carbon nanotubes (MWNTs) with mixtures of concentrated sulfuric acid and 500 wt% of  $\text{KMnO}_4$ . [26] This unzipping method is based on the strong oxidation of alkene permanganate in acidic conditions, (see scheme 1.1). The first step is the formation of manganate ester, which oxidizes the alkenes in the acid medium. Juxtaposition of the oxide species distorts the  $\beta$ ,  $\gamma$ -alkenes making them more prone to further attack. Thus once an opening has been initiated the tubes just opens up or unzips. This could occur in a longitudinal cut or in a spiral manner depending upon the initial site of attack and the chirality of the nanotube.



**Scheme 1.1: A chemical mechanism of cleavage of the carbon  $sp^2$  network.**

A defect bearing a manganate ester is first created on the sidewall of the carbon  $sp^2$  network in a permanganate oxidative environment. This defect can further oxidize in the dehydrating oxidative medium to form a dione species. The juxtaposed ketones cause a strong steric hindrance that distorts the  $\beta,\gamma$ -alkenes (marked as red), making them severely more prone to the attacks by permanganate. After consecutive attacks, the  $sp^2$  network is eventually cleaved.

Another important method to produce graphene nanoribbon has been demonstrated by Jiao et al.[25] In this method, the carbon nanotube was first coated with a polymer, such as poly(methyl methacrylate) (PMMA), and was exposed to high-power plasma etchant which unzips them into nanoribbons. Both the quality and the widths are well-controlled in this method, which can be advantageous for fabrications of nanoribbon-based high-quality devices. It has several advantages over the method above. 1) The quality of graphene nanoribbons is pristine, due to the fact that no oxidation is required; 2) This

method requires no solvents, thus the products contain no residue like other liquid phase exfoliations; 3) the process is generally fast. However, from the experimental results, there were no large ribbons observed.

### **1.3: CARBON NANOTUBE:**

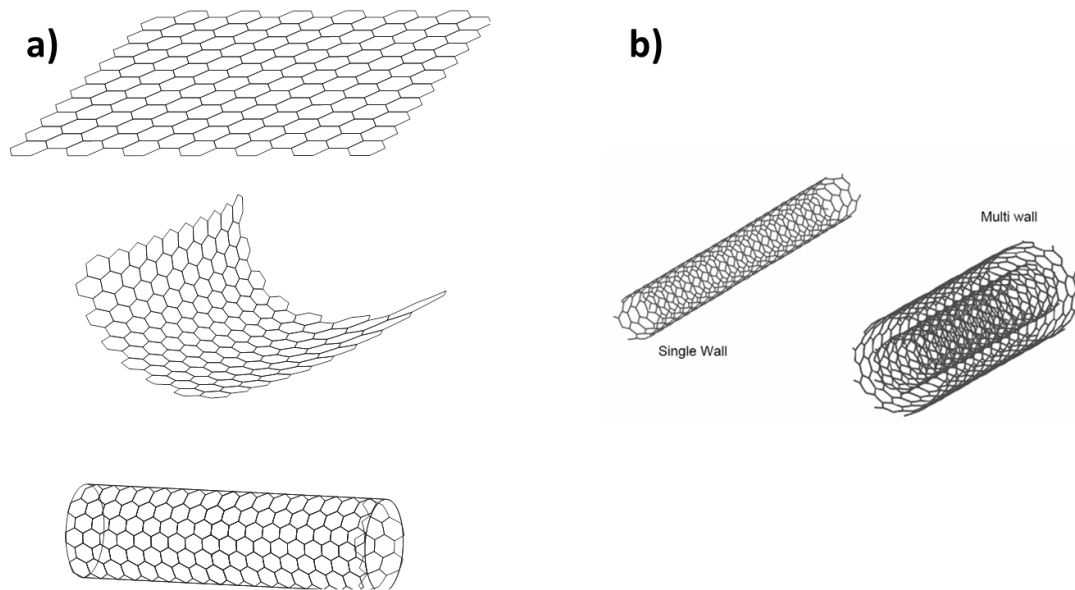
#### **1.3.1: Discovery of carbon nanotube:**

Carbon nanotubes were first discovered in a black soot by-product from a chemical vapor deposition (CVD) process[2, 27] by Sumio Iijima. While he was examining the carbon by-product materials under an electron microscope, he surprisingly observed some thin needle-like material, which tended to be curvy then straight. His later findings further proved that these tubes have graphitic structures. However, these tubes did not generate much interest then, due to the fact that they were structurally impaired, thus quality was not ideal. Carbon nanotubes have been increasingly attracting great interest due the huge improvements in the synthesis of tubes with higher quality. Tremendous research has been concentrated in the syntheses[28] and applications of high quality carbon nanotubes, such as electronic circuits, and thin films[29].

#### **1.3.2: Morphology of carbon nanotube**

Ideally, nanotubes are seamless cylinders composed of hexagons and capped with hemispherical half-fullerenes at both ends. A carbon nanotube can be technically viewed as a cylinder made up of a rolled up sheet of graphene as depicted in figure 1.5a. There are currently three main types of carbon nanotube



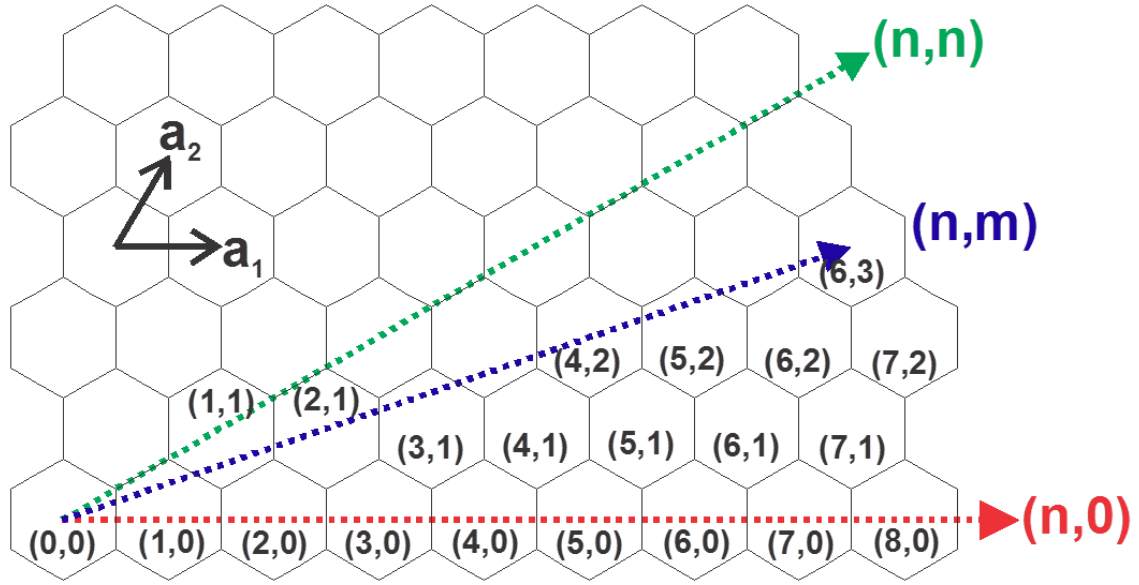


**Figure 1.5. Morphologies of carbon nanotubes.** a) A carbon nanotube can be technically viewed as a cylinder made up of a rolled up sheet of graphene. b) Schematic drawings of a single-walled carbon nanotube (SWNT) (left), and a multi-walled carbon nanotube (right).

that are being extensively investigated. 1) single-walled carbon nanotube (SWNT) are tubes with single shell (figure 1.5b left), 2) double-walled carbon nanotube (DWNT) are tubes with two shells, and 3) multi-walled carbon nanotube (MWNT) are tubes with more than three shells (figure 1.5b right). While the diameters of the tubes are about 1 nm for SWNT and up to 200 – 300 nm for MWNT, the length of nanotubes can be up to centimeters, giving them an astonishing length-to-width or an aspect ratio of up to  $10^7$ .

Another important characterization of carbon nanotubes is their chirality. Chirality of each nanotube is based on a chiral or wrapping vector ( $C_h = na_1 +$

$ma_2$ ) that connects equivalent atomic positions in to a graphene sheet denoted as an integer pair  $(n, m)$ , see figure 1.6. One must realized that not all ways of rolling up a graphene sheet would result in a unique carbon nanotube. The rolling



**Figure 1.6: An unrolled honeycomb lattice crystal structure of carbon nanotubes.** This figure shows the structural relation between a graphene sheet and different potential types of carbon nanotube which can be formed if it is rolled up. The vectors  $\mathbf{a}_1$  and  $\mathbf{a}_2$  are the basis pair that defines the chiral vector  $\mathbf{C}_h = n\mathbf{a}_1 + m\mathbf{a}_2$ , where  $(n, m)$  is an integer pair. Every value of  $\mathbf{C}_h$  gives rise to a unique carbon nanotube.

must follow the convention of  $n \geq m \geq 0$ . This convention identifies all unique possible nanotubes, including their diameter of  $D = \sqrt{3} a_{c-c} (n^2 + nm + m^2)^{1/2} / \pi$ , where  $a_{c-c}$  being the nearest-neighbor atomic distance, 1.421 Å for graphite. Another parameter that greatly affects the rolling of a graphene sheet into a carbon nanotube is the chiral angle, which is defined as  $\theta = \tan^{-1}[\sqrt{3}m/(2n + m)]$ , and is the angle between the hexagonal chain in the  $\mathbf{a}_1$  direction and the

chiral vector. Carbon nanotubes with an index of  $(n, 0)$  are termed “zigzag” nanotubes with a chiral angle  $\theta = 0^\circ$ . This kind of carbon nanotube has the hexagonal carbon rings arranged into a closed loop around the circumference. Another extreme type is the “armchair” nanotubes which have a chiral angle  $\theta = 30^\circ$  where the hexagonal rows are arranged in such a way that they are parallel to the tube axis. All other tubes are known as “chiral” tubes, having chiral angle of  $30^\circ > \theta > 0^\circ$ . Based on the chirality and the diameter, each individual carbon nanotube can be metallic, semi-metal, or semi-conducting[30], as will be discussed in the following section.

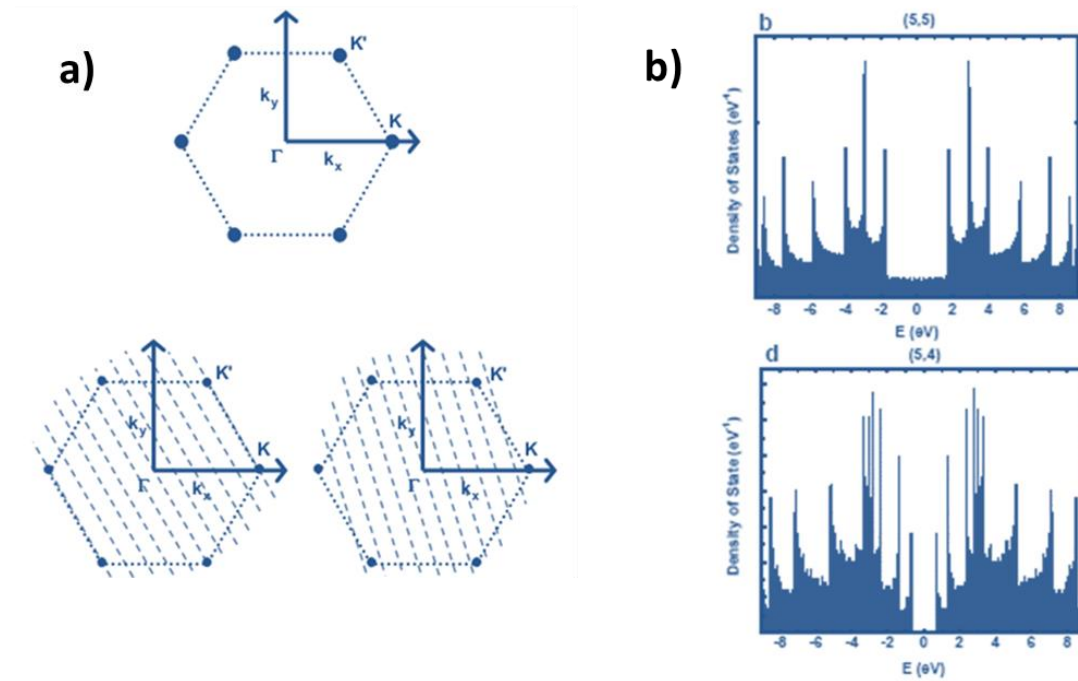
Another important morphology of natural appearance is carbon nanotube bundles, which is formed with nanotube tubes strongly attached to one another via van der Waals attraction force, similar to that of graphene layer interaction with each other to form graphite. These bundles or ropes consisted of many tubes preferentially aligned in a close-packed triangular lattice. When carbon nanotubes are adjoined together, the local symmetries are broken and interfered, leading to band repulsion and depletion of states near the Fermi level, which severely hinders the properties of carbon nanotubes. Thus, to incorporate carbon nanotubes, one must individually disperse carbon nanotubes into suspensions, which requires the elimination of this attraction force.

### **1.3.3: Electronic properties of carbon nanotubes:**

The phenomenal properties of carbon nanotubes originate from their special electronic structures that each individual tube can be metallic, semi-

metallic or semi-conducting, predominantly depending on its diameter and chirality[31]. As discussed in the very beginning of this chapter, each carbon atom has four electrons in the outer shell in a graphene sheet, and three of them are responsible for  $\sigma$  bonding with the last one dedicated for  $\pi$  bonding with other carbon atoms. In this bonding system, the  $\pi$  bond is higher in energy than the  $\sigma$  bonds, thus the Fermi level settles in this  $\pi$  band, which is the ultimate factor that governs the properties of the carbon nanotube. When the graphene sheet is rolled into a cylindrical structure to form carbon nanotubes, a periodic boundary is imposed along the direction of the chiral vector. This gives rise to quasi-1-D electronic states that are based on 2-D dispersion relations of graphene sheet[32]. With these electronic states azimuthally quantized if unhindered in the axial direction, the states of carbon nanotubes can be represented in reciprocal space by a series of parallel lines representing the azimuthal subbands that are drawn at the intersection of the 2-D graphene Brillouin zone (as discussed above). Figure 1.7a shows the two distinct cases for the electronic structures of carbon nanotubes. When the Fermi level is an allowed state of a carbon nanotube, its conduction and valence bands will overlap, creating a metallic nanotube. On the other hand, when the Fermi level is not an allowed state, there will be an energy gap between the conduction and valence bands of a carbon nanotube, creating a semiconducting tube. Thus, the chiral indices, as mentioned above, can be used to determine the type of carbon nanotubes. When  $n - m$  is an integer multiple of 3, the tube will have a metallic density of states (DOS),

while other tube will have semi-conducting DOS. Because of this reason, it is always estimated that one-third of carbon nanotubes are metallic tubes, while the rest are semi-conducting carbon nanotubes.



**Figure 1.7:** a) Brillouin zone of a graphene unit cell (top). Dashed lines are the allowed wavevectors (electronic states) of two different carbon nanotubes: a metallic (5, 5) (left) and a semi-conducting (5, 4) (right) and are superimposed onto the graphene Brillouin zone to illustrate that the  $K/K'$  points are allowed in the (5, 5) metallic nanotube, while the  $K/K'$  points are forbidden in the (5, 4) semi-conducting nanotube. b) Plots of the density of states (DOS) for a metallic armchair (5, 5) SWNT, and for a semi-conducting chiral (5, 4) SWNT.

It is well-known that the DOS of carbon nanotubes, as in other 1-D systems, are dominated by van Hove singularities. In metallic (M) tubes, the almost linear  $\pi$  band dispersion near the Fermi level creates a constant DOS in-between the pair of van Hove singularities closest to the Fermi level. However, in

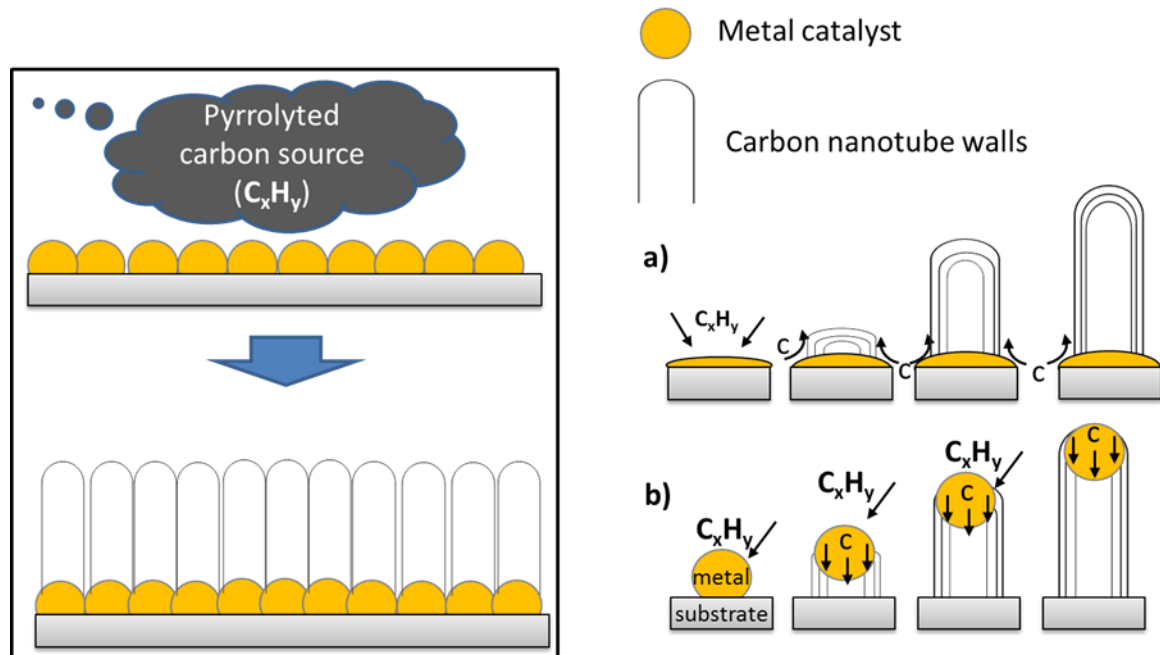
semi-conducting (S) carbon nanotubes, the energy gap is dependent on the chirality and it spans the region between the van Hove singularities for filled and empty states. An example of the DOS of a typical metallic tube (5, 5) and a semi-conducting nanotube (5, 4) is depicted in figure 1.7b.

Due to the distinct van Hove singularity properties, optical absorption spectroscopy has been extensively applied to carbon nanotubes for characterization of their electronic structures. In optical measurements, the scanning range usually covers ultraviolet, visible and near-infrared regions of the spectrum. The response from carbon nanotube suspension originates from the transition between the conduction and the valence bands, where only the transition pairs of singularities that are symmetrically placed with respect to the Fermi level are allowed. These allowed transitions are labeled as  $E_{ji}$  (where  $i = 1, 2, 3, \dots$ ). A typical absorption spectrum of bulk carbon nanotube consists of three main absorption peaks as  $E_{11}^S$ ,  $E_{22}^S$ ,  $E_{11}^M$ , which are associated with the lowest transition in semi-conducting tubes, the second transition of the same semi-conducting tubes, and the first transition of metallic carbon nanotubes, respectively.

#### **1.3.4: Synthesis techniques:**

To date, there are three main techniques to synthesize carbon nanotubes: 1) arc discharge[2, 33], 2) laser ablation[34], and 3) chemical vapor deposition[35]. All these methods require the generation of free carbon atoms and the precipitation of the dissolved carbon out from the catalyst particles[36],

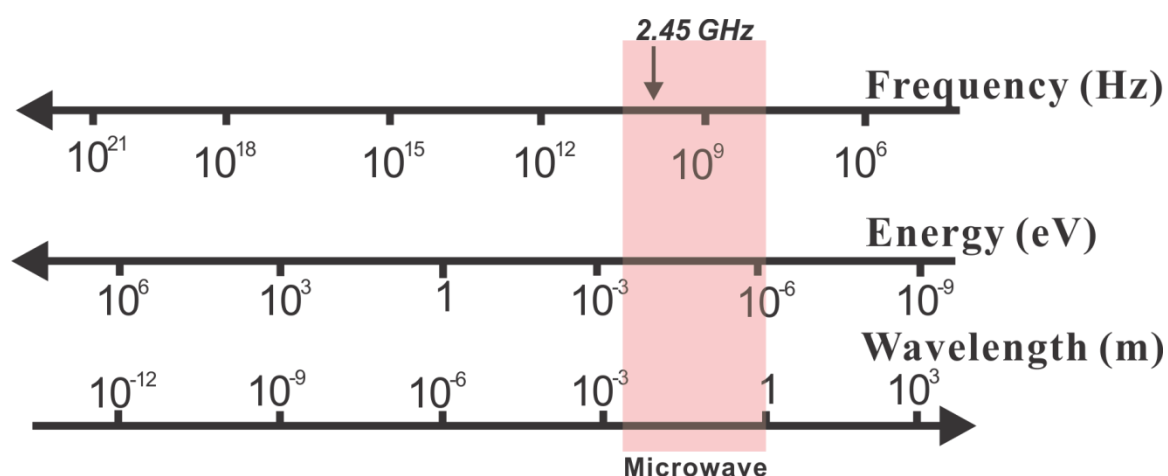
without these catalysts, no carbon nanotubes can be formed. In general, the growth of carbon nanotube stops when the catalysts become deactivated either by carbide formation or by poisoning from impurities or over-growth. The exact growth mechanism of carbon nanotubes is still unknown, but can be classified



**Figure 1.8: Visualizations of carbon nanotube growth mechanisms by CVD.** Typically, carbon nanotubes are grown by the precipitation of saturated carbon pyrrolyzed from carbon sources ( $C_xH_y$ ) at elevated temperatures. Depending on the interaction between the catalyst particles and the substrate, carbon nanotubes can grow in two mechanisms: top growth (a) and base growth (b).

Into two main categories: tip growth and base growth (see figure 1.8). They undergo similar steps; firstly metal catalysts have to be present which are generated under high temperatures, then decomposed carbon resource diffuses into the surface of the catalyst particles and concentrate. Finally, as the catalyst particles are becoming saturated, tube-like carbon-based materials precipitate out of the catalyst and grow out of the catalyst. Depending on the interaction

between the catalyst particles and the substrate, carbon nanotubes can grow via two mechanisms: tip growth and base growth. If the interaction between them is strong, the catalyst particles are anchored onto the substrate, the carbon nanotubes grow on top of the catalyst particles. If the interaction between the catalyst particles and the substrate is weak, the catalyst particles get “lifted up” and stay on top during the carbon nanotube growth, and this is termed “tip growth”.



**Figure 1.9: Microwave irradiation frequency range relative to electron energy and wavelengths on electromagnetic spectrum.** Red shadow shows the full range of microwave irradiation in the frequency of 0.3 to 3 GHz, which lies between infrared and radio frequencies.

#### 1.4: MICROWAVE CHEMISTRY:

Microwaves are electromagnetic waves which consist of an electric and a magnetic field component. The microwave region of the electromagnetic spectrum lies between infrared and radio frequencies in the range of 0.3 to 300 GHz, as shown in figure 1.9, which correspond to the range of wavelengths from

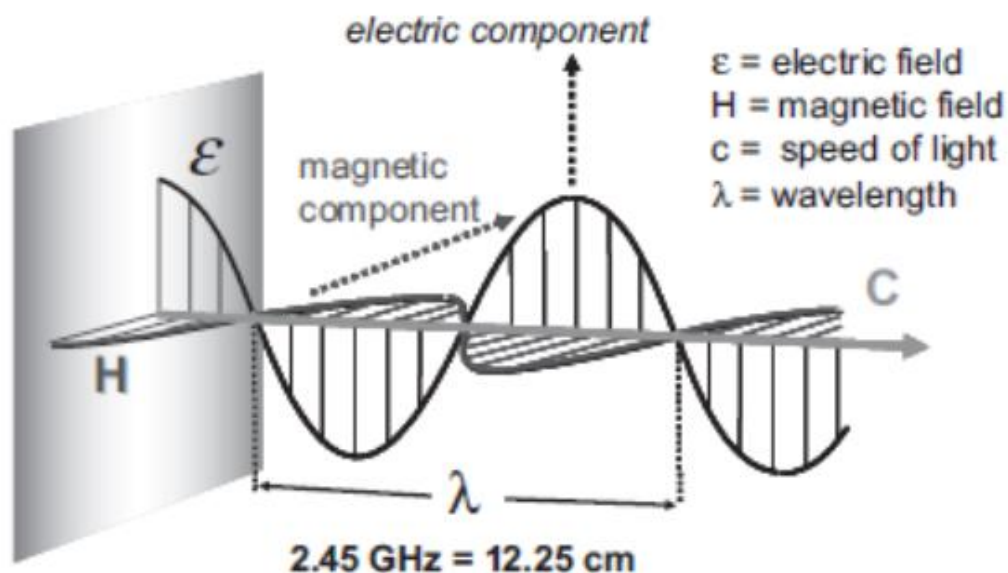


1 cm to 1m. However, for most of the purposes in microwave-assisted chemistry reactions, the electric component of the electromagnetic field is of importance for wave-material interactions. The heating effect induced by microwave irradiations is significantly different from that of conventional heating. The energy in microwave photons (0.037 kcal/mole) is very low relative to the typical energy required to initiate molecular bond cleavages (80-120 kcal/mole), thus microwave irradiation will not affect the structure of the compound being irradiated.

| Solvent (bp C)  | Dielectric Constant | Tan $\delta$ | Dielectric loss ( $\epsilon''$ ) |
|-----------------|---------------------|--------------|----------------------------------|
| Water           | 80.4                | 0.123        | 9.889                            |
| DMSO            | 45.0                | 0.825        | 37.125                           |
| Methanol        | 32.6                | 0.659        | 21.483                           |
| Ethanol         | 24.3                | 0.941        | 22.866                           |
| Ethylene Glycol | 37.0                | 1.350        | 49.950                           |
| 1-propanol      | 20.1                | 0.757        | 15.216                           |
| 2-propanol      | 18.3                | 0.799        | 14.622                           |
| Acetic Acid     | 6.2                 | 0.174        | 1.079                            |
| DMF             | 37.7                | 0.161        | 6.070                            |

**Table 1.1:** Boiling point, dielectric constant, tan  $\delta$ , and dielectric loss ( $\epsilon''$ ) for 9 common solvents (measured at room temperature and 2450 MHz)

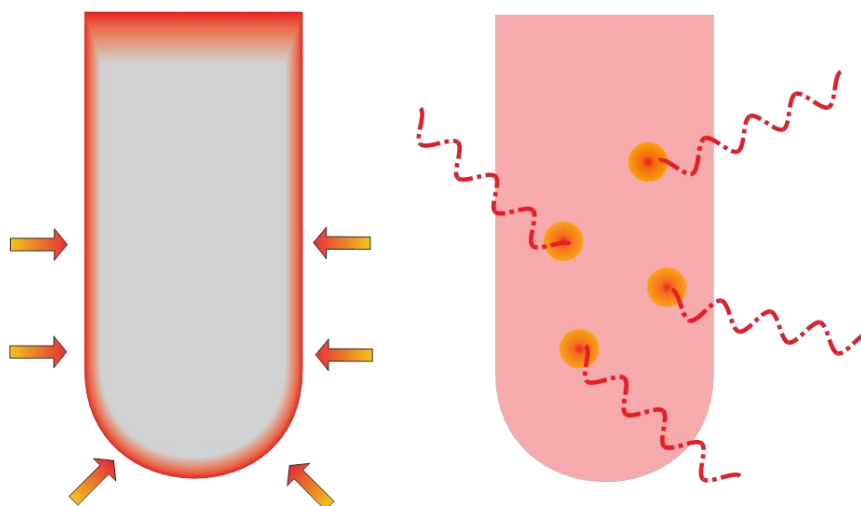
Microwave heating uses the ability of solids and liquids to transform electromagnetic portion of the energy into heat (figure 1.10). The microwave couples directly with the molecules in the reaction vessel; thus generates a rapid rise in temperature, which does not depend on the thermal conductivity of the vessel nor the solvents.



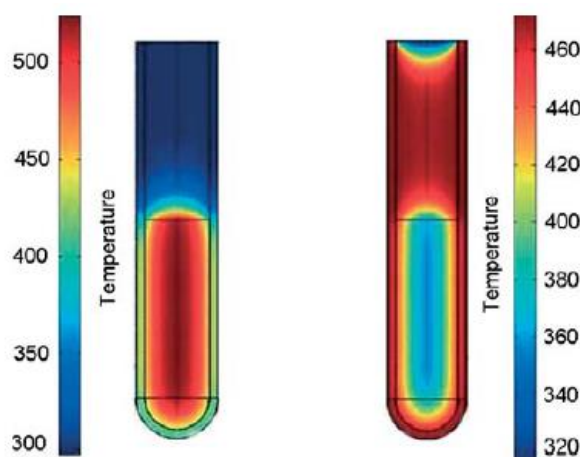
**Figure 1.10:** Schematic of microwave irradiation wave showing electric and magnetic fields. Reproduced from Practical Microwave Synthesis of Organic Chemists. Wiley-VCH, Weinheim, 2009.

Microwaves will react with either dipole rotation or ionic conduction to generate the heat. The magnitude of heating depends strongly on the dielectric properties of the molecules. Table shows the dielectric properties of 9 commonly used solvents and **Table 1.1:** Boiling point, dielectric constant,  $\tan \delta$ , and

dielectric loss ( $\epsilon''$ ) for 9 common solvents (measured at room temperature and 2450 MHz) substances. The heating effect induced by microwave is rapid and



**Figure 1.11:** Schematic of the difference of heating mechanisms between conventional heating (left) and microwave heating. With conventional heating (left), such as heating mantles and hot baths, temperature on the side surface of the vessel is greater than the internal temperature. With microwave heating (right), the microwave-absorbing reagents and solvents convert microwave irradiation into heat, and create localized superheating.



**Figure 1.12:** Temperature gradients in microwave versus oil-bath heating. Same substance after 1 minute of microwave irradiation (left) compared to treatment in an oil-bath (right). Microwave heating simultaneously raises the temperature of the entire volume, while the vessel wall is heated first in the oil-bath-heated with the internal temperature being not affected. Temperature scales in Kelvin. Reproduced from *Practical Microwave Synthesis for Organic Chemists*. Wiley-VCH, Weinheim, 2009.

volumetric; the entire material which is microwave active is heated simultaneously. In contrast, conventional heating, such as refluxing or hot oil bath heating, is relatively slow and inefficient, because the heating energy is driven into the substance, passing first through the walls of the vessel, and then to the solvent and finally to the reactants. This conventional heating method results in the temperature of the vessel being higher than the temperature of the reaction mixture. The immediate advantageous effects of microwave heating can be summarized in figure 1.11, and figure 1.12.

## **1.5: COLLOIDS AT THE LIQUID-LIQUID INTERFACE:**

### **1.5.1: Interfacial chemistry:**

All liquids tend to adopt shapes that minimize their surface areas, in order for its molecules to be surrounded by maximum amount of molecules from other bulk substances. The force that is responsible for minimizing the surface area is known as the surface tension and is governed by the following:

$$dw = \gamma dA$$

where  $w$  is the work needed to change the surface area,  $A$ , of a system, and  $\gamma$  is the surface tension of a system.

An interface between two bulk phases, such as liquid-vapor (water-air) or liquid-liquid (oil-water), can be imagined as separated by a dividing line[37]. In a system with two ideal bulk materials, this dividing line would have zero thickness. However, in reality, since there will always be some solubility of one substance to another, thus the thickness of the interface is always greater than zero.

### **1.5.2: Emulsions:**

The interfaces between two immiscible liquids (oil and water) are very common in daily lives and in industrial processes. One example is an emulsion which has been defined as a fluid (dispersed/internal phase) being fully dispersed or suspended throughout another fluid (continuous/external phase). The properties of the interface between water and oil are vital in determining the stability of an emulsion system. The formation of an interface between the bulk

dispersed phase and the bulk continuous phase increases the system free energy, therefore the emulsions are not thermodynamically stable, and tend to minimize the surface area by break-up or re-coalescence of emulsions. To gain stability, emulsifiers (e.g. surfactants, derived from “surface-active”) are added with some external mechanical forces, such as stirring, shaking or sonication to obtain stable emulsions.

There are three principal methods in preparing emulsions that are commonly employed and a work by Becher et al. has comprehensively covered this topic[38]. In short, these three methods include 1) physical emulsification by drop rupture, 2) emulsification by phase inversion, and 3) spontaneous emulsification. The first method depends more on the mechanical nature of the process (amount and form of energy input, while the latter two methods are based on the chemical process in that the final emulsion will be controlled by the chemical makeup of the system, such as the chemical nature of the additives, the ratios of the two phases, and the temperatures. In almost all practical emulsification processes, energy has to be input into the systems (see table 1.2), these processes provide external energies to break up the two phases into small droplets, at this point, small dispersed phase droplets are immersed in the continuous phase. As will be discussed below, the presence of emulsifiers will be vital to successful emulsion formation and stability.

| Method  | Energy Input <sup>i</sup> | Process <sup>ii</sup> | Drop Formation <sup>iii</sup> |
|---|---------------------------|-----------------------|-------------------------------|
| Shaking   | L                         | B                     | T                             |
| Stirring  | L                         | B, C                  | T, V                          |
| Colloid mill  | M-H                       | C                     | V                             |
| Ball and roller mill  | M                         | B, C                  | V                             |
| Homogenizer   | H                         | B, C                  | T, V, C                       |
| Ultrasonic  | M-H                       | B, C                  | C, T                          |
| <sup>i</sup> L = Low, M = Medium, H = High<br><sup>ii</sup> B = Batch, C = Continuous<br><sup>iii</sup> T = turbulence, V = viscous forces in laminar flow, C = cavitation. |                           |                       |                               |

**Table1.2:** A short list of typical mechanical methods in preparing emulsions.

Emulsifiers usually consist of a long apolar alkyl chain that is hydrophobic (favors the oil phase), and a charged head group that is hydrophilic (favors the water phase). Due to its amphiphilicity (favors both water and oil phases), the addition of these emulsifiers lowers the interfacial tension between the water and the oil phase, making the formation of emulsion thermodynamically more favorable.

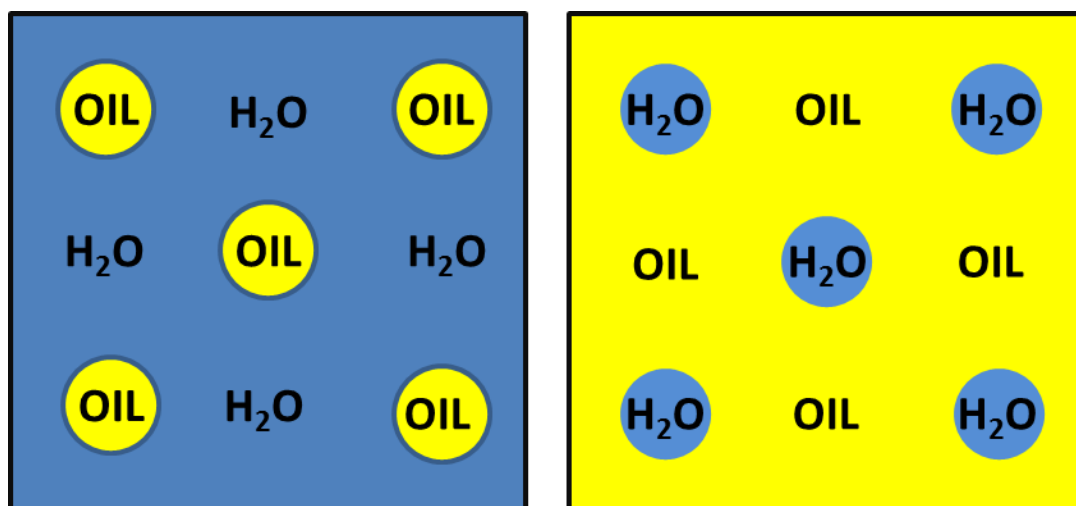
As discussed, emulsions are thermodynamically unstable, thus the free energy of formation ( $\Delta G_f$ ) of emulsions is greater than zero, causing the tendency for them to break. This instability is associated with the interfacial area of the droplets formed, as in  $A\gamma$ , where  $A$  is the surface area of the droplets and  $\gamma$  is the surface tension between the two phases. This energy term has higher influence than the entropy of formation ( $\Delta S_f$ ) associated with droplet formation, thus the total free energy of formation of emulsion droplets can be expressed by:

$$\Delta G_f = A\gamma - T\Delta S_f$$

Even though they are thermodynamically instable, emulsions are kinetically stable due to the adsorption of a layer of barrier at the new oil-water interface that will prevent or retard emulsion droplets from coming in direct contact with each other and collapse via flocculation and coalescence. This layer of barrier can be electrostatic, such as in ionic surfactants or steric, such as non-ionic surface active species or polymers. The formation of the barrier layer must be rapid relative to the rate of coalescence; otherwise a coarsening of the emulsion will result.

Emulsions can be classified into two basic types: oil-in-water (O/W) and water-in-oil (W/O) emulsions (see figure 1.13). When describing the type of emulsions, the first term is the discontinuous phase, while the last term is the continuous phase. However, some other simple emulsion systems may also contain droplets of the continuous phase dispersed within each of the dispersed





**Figure 1.13: Two major types of emulsion.** Oil-in-water (O/W) emulsion and water-in-oil (W/O) emulsion

phase droplets. Such systems are called double emulsions or multiple emulsions[39]. A more complicated system with solid dispersion, for example, magnetic colloids[40], within each droplet has also been successfully prepared. Whether an emulsion is O/W or W/O greatly depends on a number of parameters including oil/water ratio, temperature, *etc.* It was then realized that the nature of the emulsifiers is the dominant factor for stability and the emulsion type. According to Bancroft[41, 42], the phase in which the surfactant is favorably dissolved in tends to be the continuous phase. Water soluble surfactants tend to form O/W emulsions while oil-soluble surfactants result in W/O emulsions.

Emulsions have generated great impacts for our daily lives, because of their applications in the food, cosmetic and pharmaceutical industries. Some examples of emulsions include milk, lotions, paints, and drug delivery carriers.

Emulsions, if prepared properly, are stable for months or even years, however, Due to the thermodynamic instability, emulsion droplets tend to reduce their total free energy by increasing droplet diameters, so reducing their total interfacial area. The degradation of emulsions can be classified into different mechanisms and they are listed below and in figure 1.14.

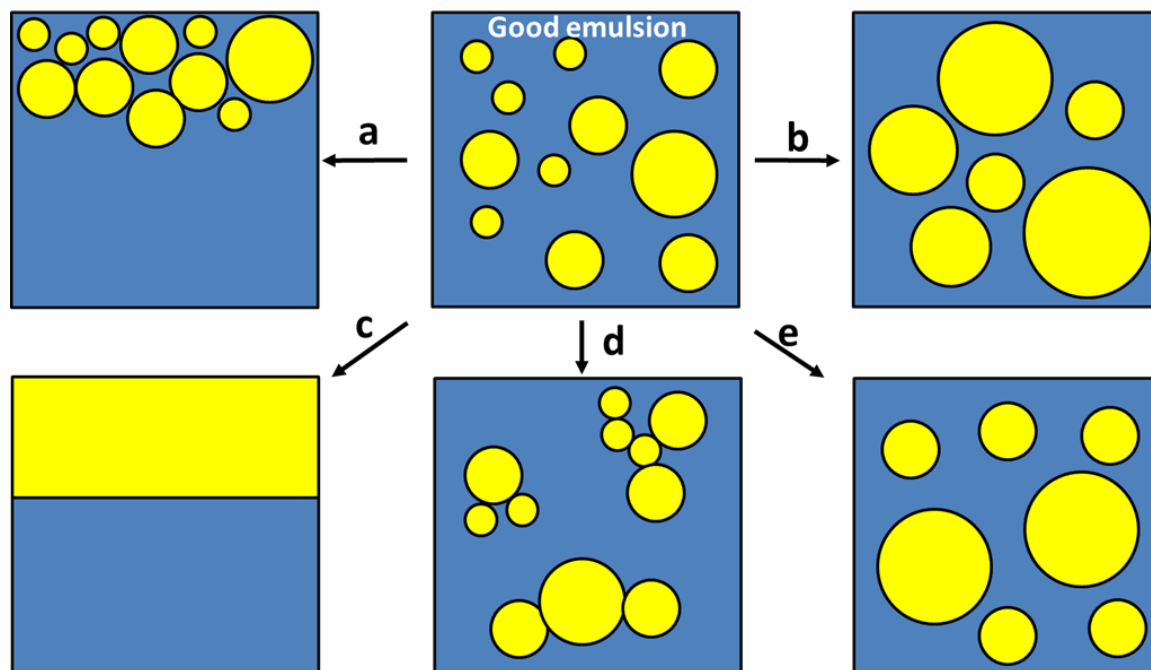
1. Creaming
2. Aggregation with creaming
3. Coarsening of emulsion droplets through Ostwald ripening
4. Droplet coalescence

### **1.5.3: Pickering Emulsion**

Self-assembly of colloid particles and the formation of stable emulsions at the liquid-liquid interface has been well-documented since 1907 by Pickering[43]. Pickering was the very first to describe a phenomenon in which an emulsion was stabilized by colloidal particles (in his case, colloidal silica particles). Since his discovery, Pickering emulsions have been used as templates for preparing advanced functional materials, such as Janus particles[44] and colloids capsules[45]

The formation of Pickering emulsion often involves irreversible adsorption of colloidal solid particles at the liquid/liquid interface to form a robust barrier that prevent breaking of the emulsion bubbles. The solid colloids that build the barriers must be able to be partially wetted by both liquids and exhibit a contact

angle at the three-phase contact line. To reach maximum stabilization, these colloids should be preferentially wetted by the continuous phase in the biphasic system. If the solid is excessively wetted by either phase, the stabilizing effect will not result.



**Figure 1.14:** Most important mechanisms of the degradations of emulsion from a good emulsion (top middle): a) creaming; b) Ostwald ripening; c) breaking; d) flocculation; e) coalescence.

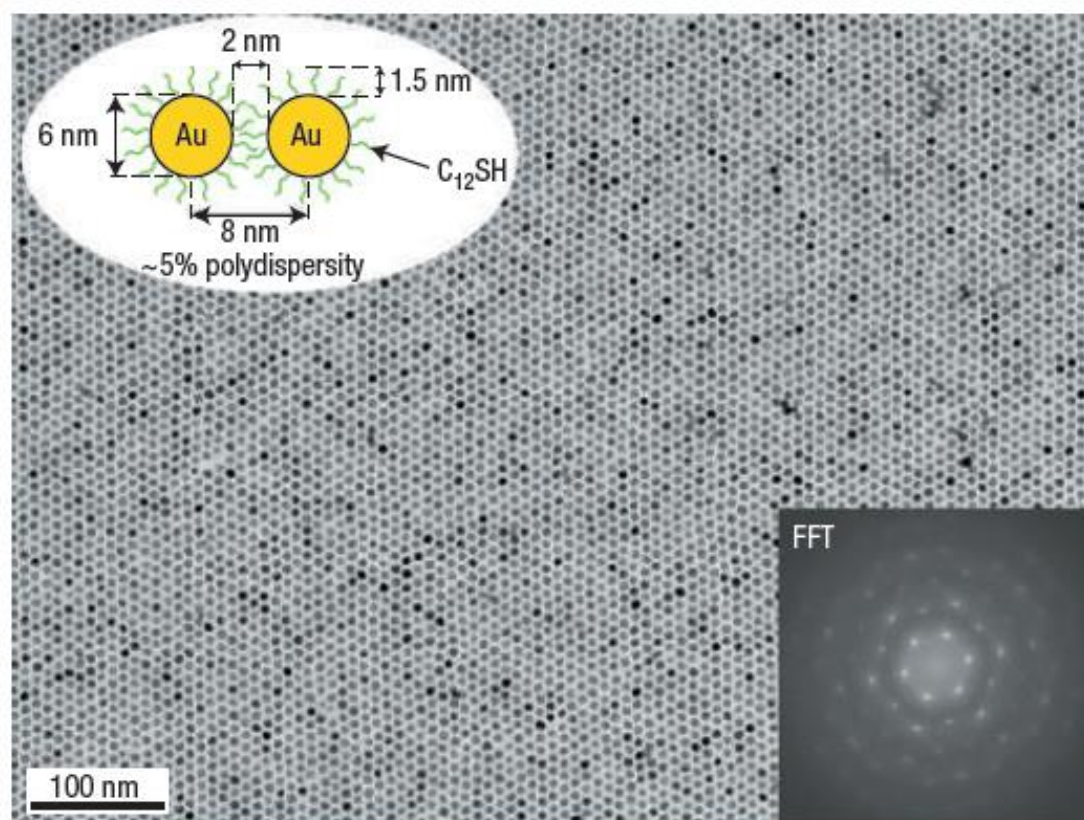
#### 1.5.4: Self-assembly of nanoparticle films:

Self-assembly of particles has attracted much attention for its fabrication of nanoscopic materials with special electronic and optical properties[46-48]. Different processes have been proposed to produce 2-D particle films (colloidal films) with fairly high homogeneity. The most common method is by controlling

the evaporation rate of the solvent[49]. Liquid-liquid interfaces are especially ideal templates for self-assembling nanoparticles into 2-D structures. This is because the nanoparticles, the building blocks can move at the interface and the interaction with the interface can be manipulated by different methods, thus highly-ordered structures can be formed with defects of the structures spontaneously eliminated. These interfaces are highly anticipated to also offer a method for chemical manipulation of nanoparticles.

The air-water interface has been a traditional medium to prepare molecular self-assemblies, such as Langmuir-Blodgett and Langmuir-Schaefer films and other ultrathin films for potential applications[50]. The liquid-liquid interface provides a non-traditional, inexpensive route to synthesize materials with high functionalities and unusual properties. Recently, thin films at the liquid-liquid interface have drawn more attention in the production of novel nanomaterials and ultra-thin films of metals and oxides.[51, 52] Lin and coworkers showed that the self-assembly or the interfacial entrapment of cadmium selenide (CdSe) nanoparticles at an oil-water interface can be controlled by the sizes of the particles, which provided an easy to chemically and selectively modify the desired sizes of particles adsorbed at the interface[53]. Transferred self-assembled films were studied by scanning force microscopy (SFM) and transmission electron microscopy (TEM). Both results showed that the self-assembled films were formed by a densely packed monolayer with high ordering (liquid like) at the interface. The monolayer films were also shown to be

mechanically stable, the integrity was retained even when they were removed from the liquid-liquid interface[54].



**Figure 1.15:** Gold nanoparticle monolayer. Micrograph of a monolayer formed by 6-nm gold nanocrystals. Reprinted by permission from Macmillan Publishers Ltd: [Nature Materials] (55), copyright (2006).

Self-assembled films at the liquid-liquid interface of Au, Ag, and  $Fe_2O_3$  nanoparticles were also recently reported by Duan et al[52]. They demonstrated that the fabrication of nano-alloy films were possible by manipulating the liquid interfaces. Bigioni and coworkers also demonstrated the fabrication of highly ordered gold nanoparticle monolayer at the interface[55] (see figure 1.15). These

films were demonstrated to have stunning properties, such as high stiffness, high robustness and remarkable flexibility[56]. Tran and coworker showed that by performing repeated transfers of monolayer interfacial films, the formation multilayer highly ordered nanoparticle films can also be easily fabricated for electronic applications[57, 58]. Film formation at the liquid-liquid interfaces have opened a new path for the fabrication of ultrathin, organic-inorganic composite membranes, which can be used for many sensor applications.

#### **1.6: OBJECTIVE OF THE DISSERTATION:**

Several basic physical concepts and introductions of carbon based allotropes will be introduced in **chapter 1**. In addition, microwave enhanced chemistry and some basics about interfacial chemistry will also be introduced in this chapter.

In **chapter 2**, a simple and scalable approach to fabricate large graphene sheets is reported. In this approach, a controlled reaction was employed using nitronium ions to selectively and slightly functionalize graphite powder to fabricate low-oxygen-containing graphene sheets. Unlike the common product of graphene oxide, graphene sheets made with our method were large in areas and high in qualities (low defect contents, highly conductive, low degree of oxidation. Their intact graphitic structures largely retained with minimal defects. After understanding the mechanism behind the fabrication of high-quality graphene sheets, in **chapter 3**, we demonstrate that the nitronium ion chemistry can also

be applied to carbon nanotubes. Carbon nanotubes produced with our method were also highly conductive, and only slightly oxidized.

Equipped with the products with excellent properties of graphene and carbon nanotube, **chapter 4** presents an interfacial approach to fabricating graphene-carbon nanotube hybrid thin films at the liquid-liquid interface, which was demonstrated to have superior performance compared to films fabricated with only individual components. By tweaking the properties of the liquid-liquid interface, the interfacial energies can be varied. In **chapter 5**, a method of separating high-quality graphene sheets from the bulk product of graphene suspensions is reported. We also demonstrate that using similar techniques, graphene sheets can be separated based on different sizes and degrees of oxidation.

In **chapter 6**, another application using the large-area graphene sheets conjugated with a temperature-sensitive polymer, poly(*N*-isopropylacrylamide), to form oil-in-water emulsion is reported. Oil-soluble fluorescent dyes are purposely encapsulated in the emulsion droplets, and it is shown that the controlled-release of the dye can be triggered by raising the temperature to about 37 °C, which is believed to have profound potential in both bio- and physiological applications.

All corresponding references are cited at the end of each chapter, and duplicates are cited afresh in each chapter for simplicity.

### 1.7: REFERENCES

1. Guo, T., C. Jin, and R.E. Smalley, *Doping bucky: formation and properties of boron-doped buckminsterfullerene*. The Journal of Physical Chemistry, 1991. **95**(13): p. 4948-4950.
2. Iijima, S., *Helical microtubules of graphitic carbon*. Nature, 1991. **354**(6348): p. 56-58.
3. Novoselov, K.S., et al., *Electric field effect in atomically thin carbon films*. Science, 2004. **306**(5696): p. 666-9.
4. Morgan, A.E. and G.A. Somorjai, *Low energy electron diffraction studies of gas adsorption on the platinum (100) single crystal surface*. Surface Science, 1968. **12**(3): p. 405-425.
5. Van Bommel, A.J., J.E. Crombeen, and A. Van Tooren, *LEED and Auger electron observations of the SiC(0001) surface*. Surface Science, 1975. **48**(2): p. 463-472.
6. Geim, A.K. and K.S. Novoselov, *The rise of graphene*. Nat Mater, 2007. **6**(3): p. 183-91.
7. Venables, J.A., G.D.T. Spiller, and M. Hanbucken, *Nucleation and growth of thin films*. Reports on Progress in Physics, 1984. **47**(4): p. 399.
8. Evans, J.W., P.A. Thiel, and M.C. Bartelt, *Morphological evolution during epitaxial thin film growth: Formation of 2D islands and 3D mounds*. Surface Science Reports, 2006. **61**(1-2): p. 1-128.
9. Novoselov, K.S., et al., *Two-dimensional gas of massless Dirac fermions in graphene*. Nature, 2005. **438**(7065): p. 197-200.
10. Wallace, P.R., *The Band Theory of Graphite*. Physical Review, 1947. **71**(9): p. 622-634.
11. DiVincenzo, D.P. and E.J. Mele, *Self-consistent effective-mass theory for intralayer screening in graphite intercalation compounds*. Physical Review B, 1984. **29**(4): p. 1685-1694.
12. Novoselov, K.S., et al., *Two-dimensional atomic crystals*. Proc Natl Acad Sci U S A, 2005. **102**(30): p. 10451-3.
13. Blake, P., et al., *Making graphene visible*. Applied Physics Letters, 2007. **91**(6): p. 063124-3.



14. Cano-Márquez, A.G., et al., *Ex-MWNTs: Graphene Sheets and Ribbons Produced by Lithium Intercalation and Exfoliation of Carbon Nanotubes*. Nano Lett, 2009. **9**(4): p. 1527-1533.
15. Hass, J., et al., *Highly ordered graphene for two dimensional electronics*. Applied Physics Letters, 2006. **89**(14): p. 143106-3.
16. de Heer, W.A., et al., *Epitaxial graphene*. Solid State Communications, 2007. **143**(1-2): p. 92-100.
17. Hass, J., W.A.d. Heer, and E.H. Conrad, *The growth and morphology of epitaxial multilayer graphene*. Journal of Physics: Condensed Matter, 2008. **20**(32): p. 323202.
18. Berger, C., et al., *Ultrathin Epitaxial Graphite: 2D Electron Gas Properties and a Route toward Graphene-based Nanoelectronics*. The Journal of Physical Chemistry B, 2004. **108**(52): p. 19912-19916.
19. Kim, K.S., et al., *Large-scale pattern growth of graphene films for stretchable transparent electrodes*. Nature, 2009. **457**(7230): p. 706-710.
20. Obraztsov, A.N., et al., *Chemical vapor deposition of thin graphite films of nanometer thickness*. Carbon, 2007. **45**(10): p. 2017-2021.
21. Li, X., et al., *Large-Area Synthesis of High-Quality and Uniform Graphene Films on Copper Foils*. Science, 2009. **324**(5932): p. 1312-1314.
22. Li, X., et al., *Large-area synthesis of high-quality and uniform graphene films on copper foils*. Science, 2009. **324**(5932): p. 1312-4.
23. Hernandez, Y., et al., *High-yield production of graphene by liquid-phase exfoliation of graphite*. Nat Nanotechnol, 2008. **3**(9): p. 563-8.
24. Cano-Marquez, A.G., et al., *Ex-MWNTs: graphene sheets and ribbons produced by lithium intercalation and exfoliation of carbon nanotubes*. Nano Lett, 2009. **9**(4): p. 1527-33.
25. Jiao, L., et al., *Narrow graphene nanoribbons from carbon nanotubes*. Nature, 2009. **458**(7240): p. 877-80.
26. Kosynkin, D.V., et al., *Longitudinal unzipping of carbon nanotubes to form graphene nanoribbons*. Nature, 2009. **458**(7240): p. 872-6.

27. Iijima, S. and T. Ichihashi, *Single-shell carbon nanotubes of 1-nm diameter*. Nature, 1993. **363**(6430): p. 603-605.
28. Dai, H., *Nanotube Growth and Characterization Carbon Nanotubes*, M. Dresselhaus, G. Dresselhaus, and P. Avouris, Editors. 2001, Springer Berlin / Heidelberg. p. 29-53.
29. Gruner, G., *Carbon nanotube films for transparent and plastic electronics*. Journal of Materials Chemistry, 2006. **16**(35): p. 3533-3539.
30. Li, Y., et al., *Growth of Single-Walled Carbon Nanotubes from Discrete Catalytic Nanoparticles of Various Sizes*. The Journal of Physical Chemistry B, 2001. **105**(46): p. 11424-11431.
31. Jorio, A., G. Dresselhaus, and M.S. Dresselhaus, *Carbon Nanotubes, Advanced Topics in the Synthesis, Structure, Properties and Applications*. Topics in Applied Physics, ed. C.E. Ascheron. Vol. 111. 2008, Berlin, Germany: Springer-Verlag. 720.
32. Dresselhaus, M.S., et al., *Exciton Photophysics of Carbon Nanotubes*. Annual Review of Physical Chemistry, 2007. **58**(1): p. 719-747.
33. Journet, C., et al., *Large-scale production of single-walled carbon nanotubes by the electric-arc technique*. Nature, 1997. **388**(6644): p. 756-758.
34. Guo, T., et al., *Catalytic growth of single-walled nanotubes by laser vaporization*. Chemical Physics Letters, 1995. **243**(1-2): p. 49-54.
35. Kong, J., A.M. Cassell, and H. Dai, *Chemical vapor deposition of methane for single-walled carbon nanotubes*. Chemical Physics Letters, 1998. **292**(4-6): p. 567-574.
36. Jorio, A., G. Dresselhaus, and M.S. Dresselhaus, *Carbon Nanotubes: Advanced Topics in the Synthesis, Structure, Properties and Applications*. Topics in Applied Physics. Vol. 111. 2008.
37. Hiemenz, P.C. and R. Rajagopalan, *Principles of Colloid and Surface Chemistry*. 3rd ed 1997, New York: Marcel Dekker Inc.
38. Becher, P., *Encyclopedia of Emulsion Technology*. Vol. 1-4. 1985, New York: Marcel Dekker.

39. Davis, S.S., J. Hadgraft, and K.J. Palin, *Medical and pharmaceutical applications of emulsions*, ed. P. Becher. Vol. 2. 1985, New York: Marcel Dekker New York.
40. Bibette, J., *Monodisperse ferrofluid emulsions*. Journal of Magnetism and Magnetic Materials, 1993. **122**(1–3): p. 37-41.
41. Bancroft, W.D., *The Theory of Emulsification*, V. The Journal of Physical Chemistry, 1912. **17**(6): p. 501-519.
42. Bancroft, W.D., *The Theory of Emulsification*, VI. The Journal of Physical Chemistry, 1914. **19**(4): p. 275-309.
43. Pickering, S.U., *CXCVI.-Emulsions*. Journal of the Chemical Society, Transactions, 1907. **91**: p. 2001-2021.
44. Tsuji, S. and H. Kawaguchi, *Colored Thin Films Prepared from Hydrogel Microspheres*. Langmuir, 2005. **21**(18): p. 8439-8442.
45. Dinsmore, A.D., et al., *Colloidosomes: Selectively Permeable Capsules Composed of Colloidal Particles*. Science, 2002. **298**(5595): p. 1006-1009.
46. Brus, L., *Quantum crystallites and nonlinear optics*. Applied Physics A: Materials Science & Processing, 1991. **53**(6): p. 465-474.
47. Alivisatos, A.P., *Semiconductor Clusters, Nanocrystals, and Quantum Dots*. Science, 1996. **271**(5251): p. 933-937.
48. Alivisatos, P., et al., *From Molecules to Materials: Current Trends and Future Directions*. Advanced Materials, 1998. **10**(16): p. 1297-1336.
49. Kralchevsky, P.A. and K. Nagayama, *Particles at Fluid Interfaces and Membranes*. Studies in Interface Science, ed. D. Möbius and R. Miller. Vol. 10. 2001, Amsterdam: Elsevier. 654.
50. Rajca, A., *An Introduction To Ultrathin Organic Films: From Langmuir-blodgett To Self-Assembly*, By Abraham Ulman, Academic Press, London 1991, Xxiii, 442Pp., \$65, ISBN 0-12-708230-1. Advanced Materials, 1992. **4**(4): p. 309-309.
51. Kalyanikutty, K.P., U.K. Gautam, and C.N. Rao, *Ultra-thin crystalline films of CdSe and CuSe formed at the organic-aqueous interface*. J Nanosci Nanotechnol, 2007. **7**(6): p. 1916-22.

52. Duan, H., et al., *Directing Self-Assembly of Nanoparticles at Water/Oil Interfaces*. Angewandte Chemie International Edition, 2004. **43**(42): p. 5639-5642.
53. Lin, Y., et al., *Nanoparticle Assembly and Transport at Liquid-Liquid Interfaces*. Science, 2003. **299**(5604): p. 226-229.
54. Lin, Y., et al., *Ultrathin cross-linked nanoparticle membranes*. J Am Chem Soc, 2003. **125**(42): p. 12690-1.
55. Bigioni, T.P., et al., *Kinetically driven self assembly of highly ordered nanoparticle monolayers*. Nat Mater, 2006. **5**(4): p. 265-270.
56. Mueggenburg, K.E., et al., *Elastic membranes of close-packed nanoparticle arrays*. Nat Mater, 2007. **6**(9): p. 656-660.
57. Tran, T.B., et al., *Sequential tunneling and inelastic cotunneling in nanoparticle arrays*. Physical Review B, 2008. **78**(7): p. 075437.
58. Tran, T.B., et al., *Multiple cotunneling in large quantum dot arrays*. Phys Rev Lett, 2005. **95**(7): p. 076806.

## **Chapter 2: Microwave and Nitronium Ion Enabled Rapid and Direct Production of Highly Conductive Low Oxygen Graphene**

### **2.1: INTRODUCTION**

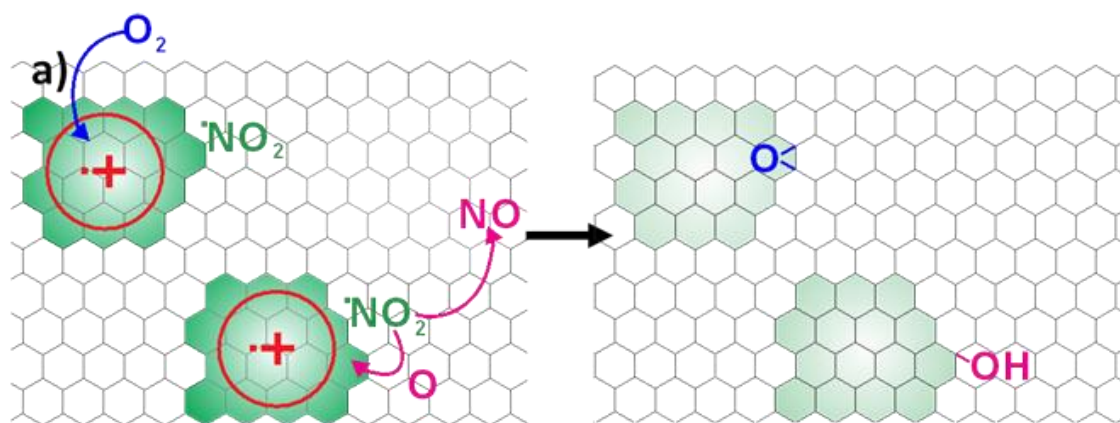
Due to its excellent electronic, thermal and mechanical properties, and its large surface area and low mass, graphene holds great potential for a range of applications. Fundamental studies and high-frequency electronics require pristine graphene.[1] However, “bulk” applications such as energy and hydrogen storage,[2, 3] flexible macroelectronics,[4, 5] and mechanically reinforced conductive coatings (including films for electromagnetic interference shielding in aerospace applications)[6-8], require large quantities of high-quality, solution-processible graphene manufactured at low cost.

Most efforts focused on enabling mass production of solution-processible graphene through time-consuming Hummer’s or modified Hummer’s methods.[9-18] In brief, one must oxidize graphite powder, exfoliate the oxidized product to form nonconductive graphene oxide (GO) suspensions, and finally reduce it to recover some fraction of its electrical conductivity via thermal and/or chemical methods. In addition, these processes can lead to excessive cutting of the graphene sheets into small pieces, and generate nanometer sized holes and vacancies in the basal plane.[19, 20] These holes and vacancies decrease the integrity of the material, thereby significantly altering their desired physical

properties, such as molecular impermeability, electrical and thermal conductivity, and mechanical strength.[21] Furthermore, to prevent aggregation of individual graphene sheets during the reduction step, surfactants and/or stabilizers are used, resulting in graphene with species attached to both sides. Residual surfactants/stabilizers can increase the resistance between the individual sheets in a thin film, thereby dramatically decreasing the overall electrical conductivity. In addition, even though new environmentally friendly reduction protocols are being developed,[16, 22] hydrazine, a hazardous material, is still widely used as the reducing agent to restore the conductivity of graphene. Finally, trace amounts of reducing agents and metal ions following Hummers' approaches can participate in unwanted reactions and be detrimental to applications such as organic solar cells.[6] Therefore, extensive cleaning and purification steps are required, making industrial scale production expensive.

This work aims to develop a simple and scalable approach, which can avoid the problems mentioned above, to quickly (30 seconds) and directly produce large ( $400\text{-}900\text{ }\mu\text{m}^2$ ), clean, and highly conductive solution-processible graphene sheets without the need of a reduction process. This new approach is inspired in part by the recent atomic level studies of the formation of vacancies and larger holes in graphene, the chemical cutting of graphene and carbon nanotubes (CNTs) into small pieces[20, 23-25] and by the recent discoveries by Tour et al.[26] who found that CNTs can be cut longitudinally into graphene oxide ribbons based on an alkene oxidation mechanism using  $\text{KMnO}_4$ . To avoid any

undesired graphene cutting, we exclude  $\text{KMnO}_4$  (used in Hummer's recipe), and make full use of oxidation by nitronium ions ( $\text{NO}_2^+$ ) that are produced by mixing concentrated  $\text{H}_2\text{SO}_4$  and  $\text{HNO}_3$ . [27, 28] Nitronium ions interact with a graphene surface to form multiple aromatic radical-ion pairs via a single electron transfer (SET) pathway. [29] At higher temperatures, multiple  $-\text{OH}$  and/or epoxy groups can be formed across the graphene surface following oxygen transfer processes to the aromatic radicals (Figure 2.1a). [27] Due to the electron donating capability



**Figure 2.1:** (a) Schematic drawing shows the proposed oxidation mechanism to directly produce highly conductive low oxygen containing amphiphilic graphene sheets. A nitronium ion forms a single electron transfer (SET) intermediate with a graphene layer, which is intercepted by a rapid oxygen transfer from molecular oxygen, affording an epoxy group; or from  $\text{NO}_2^+$  to form an OH group.

of the resulting  $-\text{OH}$  and epoxy groups, the subsequent oxidation results in more  $-\text{OH}$  and epoxy groups that are preferentially form far away from the already oxidized carbon atoms. [28] An important consequence is that if the reaction does not stop in a timely manner, subsequent oxidation will lead to the formation of

oxides, vacancies, larger holes,[25] and ultimately cutting of the graphene into small pieces, analogous to what was shown in previous CNT cutting studies.[23, 24] Therefore, the key to directly produce large conductive graphene sheets by  $\text{NO}_2^+$  is to quickly produce a low concentration of oxygen moieties that is required for the separation of individual graphene sheets, and then quench the reaction before holes and/or vacancies form. Microwave heating satisfies these requirements. Due to the high conductivity and polarizability of graphene (and graphite), the local temperature can be significantly increased (under microwave irradiation), which in turn leads to higher oxidation rates. Furthermore, the movement of the intercalation agent,  $\text{H}_2\text{SO}_4$ , and the oxidant,  $\text{NO}_2^+$ , are also dramatically increased upon microwave irradiation due to their ionic nature.[30] These concerted processes lead to the rapid dispersion of large graphene sheets containing a minimal amount of oxygen. Due to the essential role of microwave heating during the production, we refer to these graphene sheets as microwave-enabled low oxygen graphene (ME-LOGr). Compared to reduced graphene oxide (rGO) sheets prepared using Hummers' method, the ME-LOGr exhibit much larger sizes (400-900  $\mu\text{m}^2$ ), fewer defects, greater thermal stability, and comparable or higher conductivity than the solution-processible graphene reported in literatures. Our approach also results in graphene capable of being dispersed in either aqueous or organic solvents without the need for stabilizers.



## **2.2: RESULT AND DISCUSSIONS:**

### **2.2.1: Large area sized single-layered graphene sheets**

The key to fully exfoliate graphite powders for cost effective production of solution processible graphene sheets is to weaken the van der Waal interactions between individual graphene sheets within the graphite particles. The introduction of oxygen containing functional groups by oxidation is a common approach to achieve this goal. The oxidation reaction by Hummer's method introduces various oxygen containing groups in the basal planes of graphite as well as at the edges of each individual graphene sheets. The resulting graphitic oxide can be completely exfoliated in water by simple sonication or by stirring.[31] However, the oxidation process also leads to uncontrollable cutting, resulting in small GO pieces, and the formation of a large amount of individual vacancies and nanometer sized holes in the graphene plane.[19, 20] There are, in general, two main mechanisms that are responsible for cutting and creating defects on aromatic substances.

### **2.2.2: Cutting mechanisms:**

#### **2.2.2.1: Longitudinal cutting:**

The exact mechanism of cutting and creating holes and vacancies remains elusive. From density functional calculations, it was reported that the cutting is initiated by the formation of an epoxy group, which exerts strain on the basal plane of graphene. The strain facilitates the generation of another epoxy group at its nearest neighbor, and finally leads to linearly aligned epoxy groups

on the surface as oxidation progresses.[20] Another theoretical work suggested that the linearly aligned epoxy groups may also form through the migration of epoxide groups catalyzed by hydrogen transfer reactions.[32] These aligned epoxy groups co-operatively strain the graphene sheets, which accounts for the initiation of GO cutting.[20] In Hummer's method, both  $\text{HNO}_3$  and  $\text{KMnO}_4$  in concentrated  $\text{H}_2\text{SO}_4$  act as oxidants via different oxidation mechanisms ( $\text{NaNO}_3$  converts to  $\text{HNO}_3$  under acidic conditions). The  $\text{H}_2\text{SO}_4$  not only generates a strongly acidic environment for oxidation, but it also acts as an intercalation agent to allow the oxidant molecules access to the graphene surfaces within a graphite particle.

Additional insight into the mechanism of oxidative cutting graphene/GO sheets may also be derived from the extensive experimental studies of oxidative cutting (both shortening and longitudinal unzipping) of carbon nanotubes (CNTs) due to their chemical similarities. Both  $\text{KMnO}_4/\text{H}_2\text{SO}_4$  and  $\text{HNO}_3/\text{H}_2\text{SO}_4$  have been used for oxidative cutting of CNTs. While the oxidation by  $\text{KMnO}_4$  in anhydrous  $\text{H}_2\text{SO}_4$  induces predominately longitudinally unzipping of CNTs to produce graphene nanoribbons,[26] the oxidation processes in concentrated  $\text{HNO}_3/\text{H}_2\text{SO}_4$  acids preferentially leads to CNT shortening.[33] Both methods of oxidation introduce a large number of oxygen containing functional groups that facilitates the exfoliation of individual sheets in aqueous mediums. The mechanism for longitudinally unzipping CNTs was explained by having the oxidation initiated by permanganate ions attacking existing defects in CNTs, such

as alkenes, to form a manganate ester. With further oxidation, the esters can form dione structures, which could lead to the formation of vacancies and holes. At the same time, the formation of dione structures distorts the  $\beta,\alpha$ -alkenes making the neighboring sites more prone to attack. It is in this step-wise manner that the longitudinal unzipping of the tubes into ribbons occurs.

#### **2.2.2.2: Nitronium ion attack:**

On the other hand, the mixture of concentrated  $\text{HNO}_3/\text{H}_2\text{SO}_4$  acid without any  $\text{KMnO}_4$  can produce electrophilic species such as  $\text{NO}_2^+$ , which not only attack the existing defects on the graphene, but also react with the relatively inert defect free graphene basal planes, producing various oxygen containing groups, which is the first step of oxidative cutting. Through progressive oxidation, it can further etch these oxidized sites, leading to vacancies, holes and finally cutting of the CNTs into short pieces.[33]

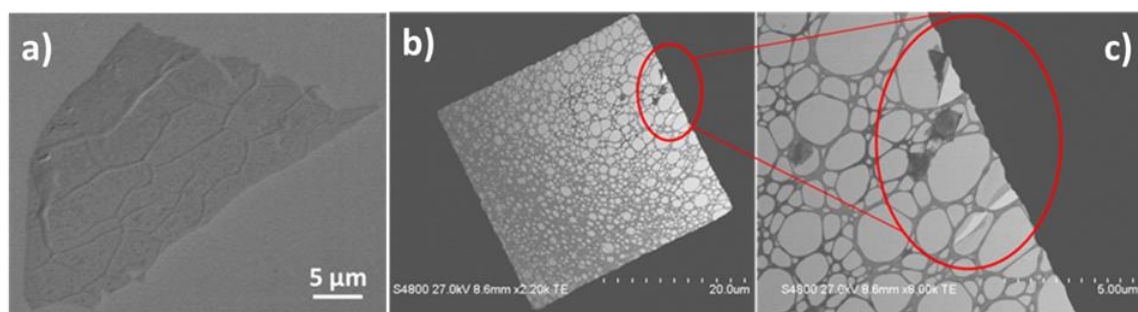
Nevertheless, an important common feature for these two oxidation systems is that the initial oxidation step, which produces various oxygen containing groups, is the rate determining step and further local oxidation (oxidation adjacent to an oxidized site) under the same reaction conditions is thermodynamically favored over oxidation on defect-free graphene regions.[34] Therefore, the optimal method would be to have a fast initial oxidation to quickly produce a sufficient density of oxygen containing groups to enable dispersion. The reaction should then be quenched so that individual vacancies do not have time to grow into larger holes (and eventual cutting) of the graphene. In the

opposite scenario, if oxygen containing groups are gradually produced, vacancies and holes would be created which grow into larger holes around the initially formed oxygen containing groups, as observed in some of the literatures.[23, 24, 35] It was reported that at higher temperatures,  $\text{HNO}_3$  and  $\text{H}_2\text{SO}_4$  intercalation can be dramatically sped up.[36] The oxidation of the graphene basal planes in a CNT by  $\text{KMnO}_4$  and  $\text{NO}_2^+$  is also enhanced.[23, 37, 38] So the ability to quickly increase and decrease the reaction temperatures will satisfy the requirement to produce large graphene sheets without cutting. For this reason, microwave heating instead of the traditional convection heating is used during the reaction.

On the other hand, the key difference between these two oxidative systems lies in the different initial oxidation step. Tour et al. noted that nitronium ions attack non-neighboring carbon atoms, whereas permanganate preferentially attacks neighboring carbon atoms.[26] However, the molecular level understanding of the oxidation mechanism by  $\text{NO}_2^+$  is still not clear.[39] The mechanism of aromatic nitration by nitronium ions has been well studied with small aromatic species.[27] The nitronium ions can interact with aromatic substrates to form nitronium-aromatic  $\pi$ -complexes via a polar two-electron electrophilic mechanism. In subsequent steps, the nitronium-aromatic complex undergoes hydrogen transfer from the complex to form nitrated aromatics. In a second scenario, the nitronium ions can also interact with the aromatic substrates via a single electron transfer (SET) pathway to form a radical-ion pair

(a donor/acceptor complex) affording an aromatic radical cation and an  $\text{NO}_2$  radical. The radical cation could be intercepted by rapid oxygen transfer from molecular oxygen, affording the respective epoxides. It is also possible that an oxygen transfers from  $\text{NO}_2^+$  to the aromatic ring resulting in the formation of phenol and NO. While more electron-rich aromatic molecules would favor the SET pathway, different substituent groups will affect the mechanism and substitution positions on the aromatic molecules.[28] Electron donating groups facilitate the SET mechanism, and further oxidation introduces substitution in the non-neighboring para-position. In contrast, electron accepting groups would make the electrophilic mechanism more favorable. With further oxidization, the neighboring carbon atoms are attacked and oxidized, or nitrated.

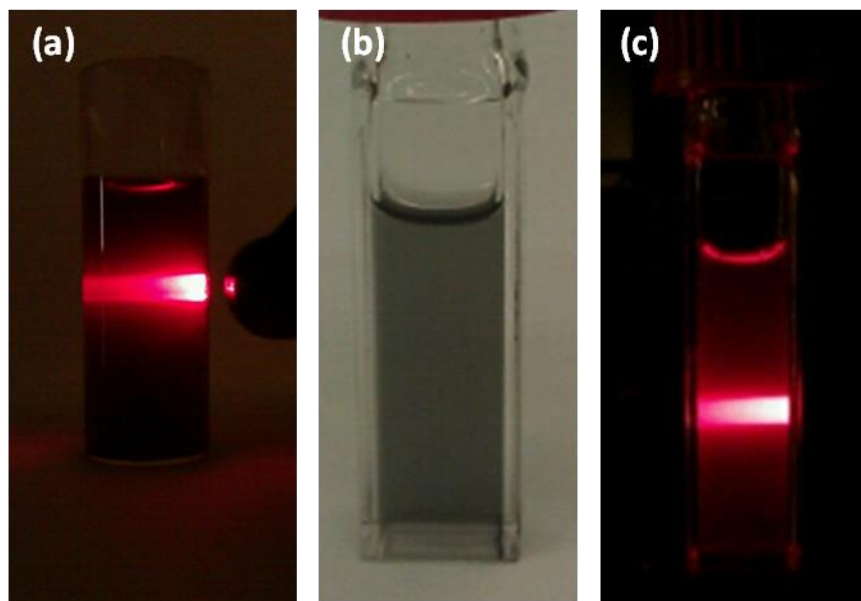
Based on these extensively studied aromatic oxidation mechanisms, combined with the known fact that nitronium ions interact with graphite via an electron transfer mechanism,[29, 40] we hypothesize that conducting graphene sheets can be directly produced by exploiting the mixture of concentrated  $\text{HNO}_3/\text{H}_2\text{SO}_4$  as the sole oxidant, and using microwave heating to enhance the initial oxidation step of forming multiple oxygen containing groups.



**Figure 2.2:** a) FE-SEM image of a large graphene sheet deposited onto a SiO<sub>2</sub>/Si substrate. b) STEM image of a graphene sheet deposited onto a holey carbon film on Cu from the same graphene dispersion. c) A magnified image of the circled area in figure 2.2b showing a side of a large graphene sheet.

In a typical experiment, graphite powder is mixed with concentrated sulfuric acid and nitric acid (1:1 volume ratio) and then subjected to 30 seconds of microwave irradiation (300 watts). The reaction results in a finely dispersed suspension that is significantly easier to purify and handle than the sticky paste obtained from Hummer's method.[41] Its topologic morphologies were intensively studied by atomic force microscopy (AFM), scanning electron microscopy (SEM) and scanning transmission electron microscopy (STEM). All these characterizations reveal the lateral size of the single graphene sheets is on average of 20-30 micrometers ( $400-900 \mu\text{m}^2$ ), which is similar the size of the starting graphite powder. Figure 2.2a shows one typical SEM image with one large sheet of  $20 \times 32$  microns in size. STEM image (figure 2.2b, c) also revealed a large sheet of graphene on the holey carbon grid showing one edge of the sheet, while other edges seem beyond the grid. We believe that the size of the sheet is similar to the size of the grid with a diagonal of  $\sim 30$  microns. The heights of the sheets were around 0.8 nm from AFM measurements, revealing that

single-layer graphene sheets were obtained. These results demonstrated large single-layer graphene sheets were directly produced and exfoliated upon microwave irradiation.



**Figure 2.3:** Digital photographs of stable ME-LOGr solution in water and in DMF. The clear Tyndall effect from both solutions indicated the colloidal characteristic of these solutions. Figure 2.3a, ME-LOGr aqueous solution, Figure 2.3b and c are ME-LOGr in DMF.

### 2.2.3: Colloidal nature of graphene suspensions:

Graphene powder can be obtained after microwave irradiation by vacuum filtration, which can be readily re-dispersed in polar solvents such as water (Figure 2.3a) or N,N-dimethylformamide (DMF) (Figure 2.3b, c) to form colloidal solutions with concentrations up to 3 mg/mL. In a nonpolar solvent, such as dichloroethene, suspensions possessing concentrations of 20 mg/L are achievable with the help of bath sonication or magnetic stirring. The high dispersibility in both polar and nonpolar solvents without requiring surfactants or

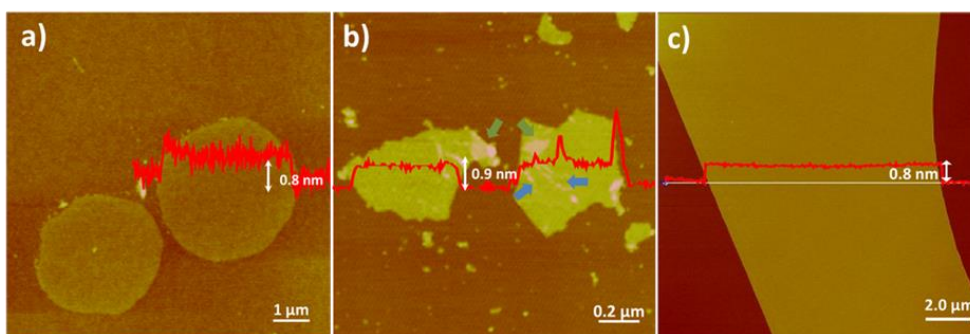
stabilizers indicates the amphiphilic nature of ME-LOGr, which is quite different from previously reported graphene sheets.[42] These solutions are stable and exhibit no precipitation for several months.



#### 2.2.4: Effect of physical agitation and the length of microwave exposure

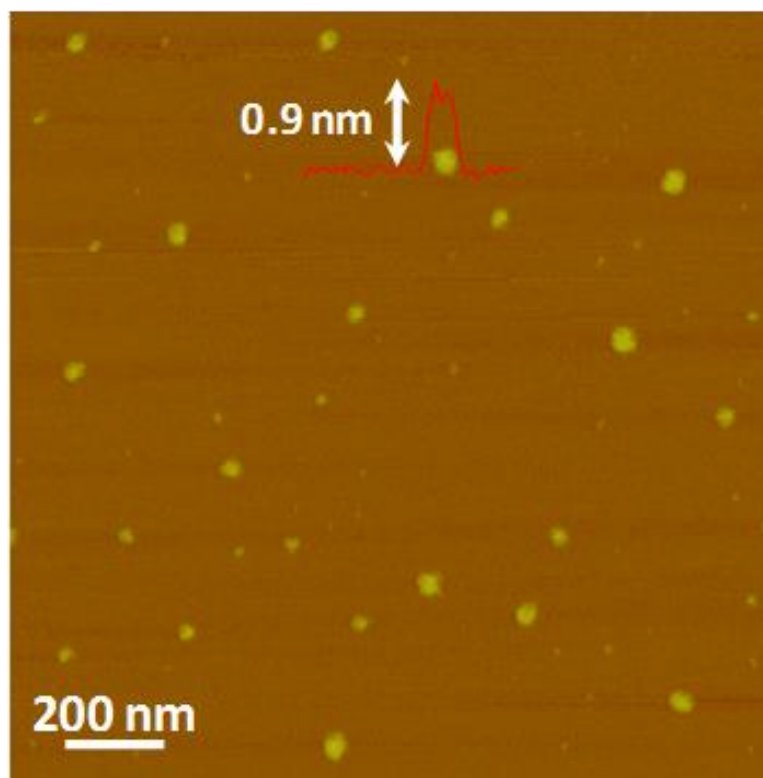
Figure 2.4a shows typical tapping-mode AFM images of the ME-LOGr sheets obtained after bath sonication and deposited on a freshly cleaved mica surface. The thickness of a single layer ME-LOGr on mica ranges from 0.7 to 0.9 nm with an average of  $0.8 \pm 0.2$  nm.

The sizes of the graphene sheets are several microns ( $2\sim 8\ \mu\text{m}$ ), still larger than GO sheets prepared by Hummer's method (typically, several hundred nanometers) (Figure 2.4b). When the ME-LOGr filtrate is exfoliated by magnetic stirring, graphene sheets of even larger sizes ( $10\sim 30$  micrometers in average) are obtained (Figure 2.4c). Note that all the ME-LOGr via direct dialysis is around  $20\sim 30$  micrometers in average, so the relatively smaller sheet size ( $2\sim 8\ \mu\text{m}$ ) obtained after bath sonication is due to sonication-induced cutting or etching.[23, 24] We did not observe holes in the sheets, which is different from graphene sheets dispersed in the presence of pyrene derivatives.[18]



**Figure 2.4:** Representative AFM images of ME-LOGr and GO. (a) ME-LOGr via bath sonication; (b) graphene oxide prepared by Hummer's method; (c) ME-LOGr prepared by magnetic stirring. The arrows in figure (b) indicate foldings and wrinkles. The height profiles are shown in red lines in each image.

To study how the microwave exposure time affects the size and electronic states of the ME-LOGr, we extended the exposure time to 60 seconds. Interestingly, the sizes of the graphene decrease down to the nanoscale. As shown in figure 2.5, individual pieces of graphene sheets that are ~50-100 nm with a height profile of 0.9 nm were typically observed, suggesting that the increasing the microwave irradiation time to 60 s caused a significant decrease in the size of the sheets, possibly due to over-oxidation induced cutting and etching (figure 2.5)[23]. This is in agreement with our hypothesis that the oxidation reaction will need to be quenched in a timely manner before over-oxidation, which governs the cutting of graphene sheets into smaller pieces, occurs. In the scenario of over-oxidation, if given enough time, defects created as small vacancies on the graphene plane could grow into larger holes around the initially formed oxygen containing groups, causing the observed extensively cutting into small graphene sheets.

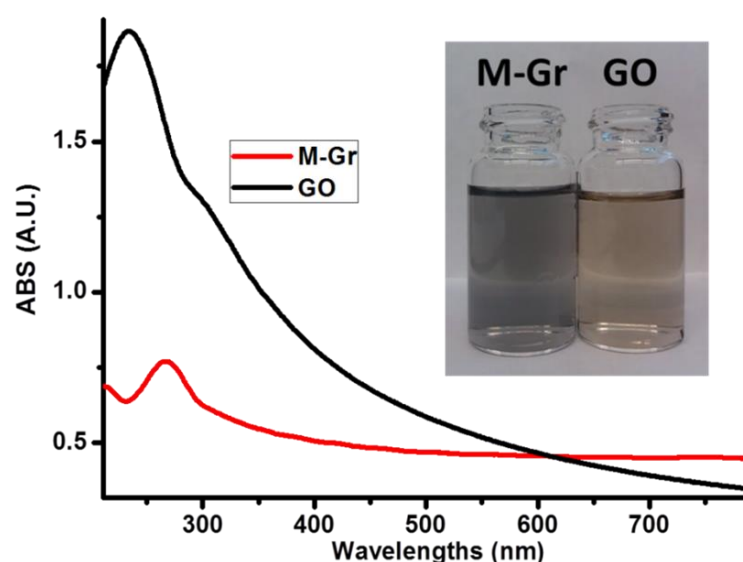


**Figure 2.5:** shows an AFM image of small graphene sheets obtained with 60 seconds of microwave irradiation.

#### **2.2.5: Optical properties and surface morphologies of ME-LOGr graphene sheets:**

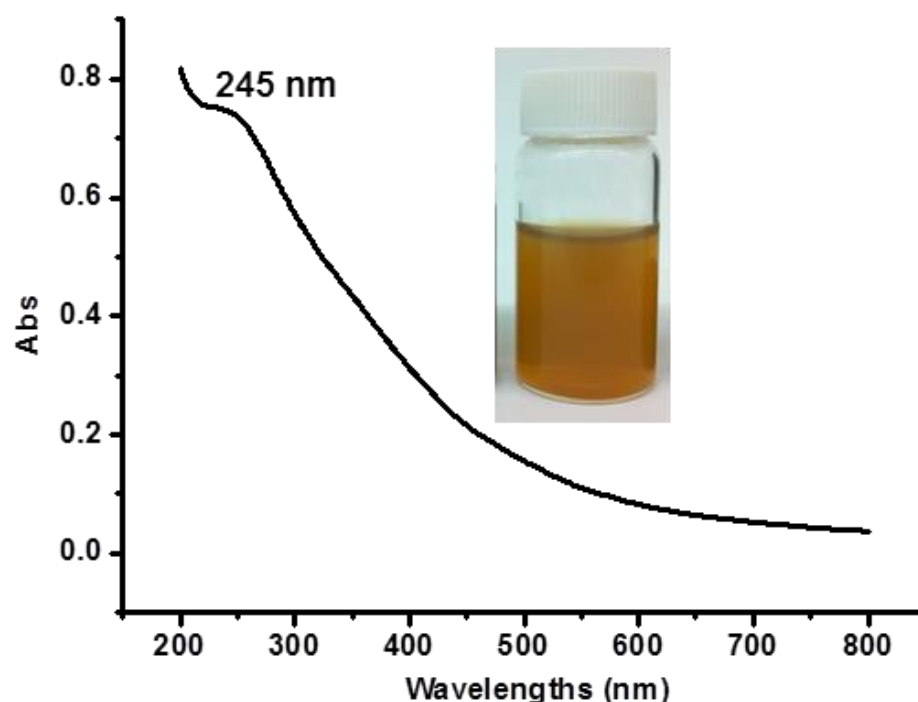
The color of ME-LOGr suspensions are grayish-black, which qualitatively suggests that we have directly obtained electrically conductive graphene sheets instead of the typically brown GO solutions (Figure 2.6., inset).[12, 13] A control experiment was performed by adding a small amount of  $\text{KMnO}_4$  to the  $\text{HNO}_3/\text{H}_2\text{SO}_4$  acid mixture. This yielded a bright yellow colored solution of fully oxidized GO shown in figure 2.7. The UV-Vis spectrum of the graphene solution obtained by adding a small amount of  $\text{KMnO}_4$  to the microwave irradiation

reaction showed an absorption peak at  $\sim 267$  nm dramatically shifts to a much lower wavelength (at 245 nm), indicating that with 30s of microwave irradiation,  $\text{KMnO}_4$  can heavily oxidize the graphitic material,[12] demonstrating the importance of excluding  $\text{KMnO}_4$  in our procedure. The bright yellow color also indicates a high-degree of oxidation, similar to that of GO prepared by Hummer's



**Figure 2.6:** UV-Vis spectra of ME-LOGr (red) and GO (black). Inset: a digital photo showing the different colorations of ME-LOGr and GO solution in water.

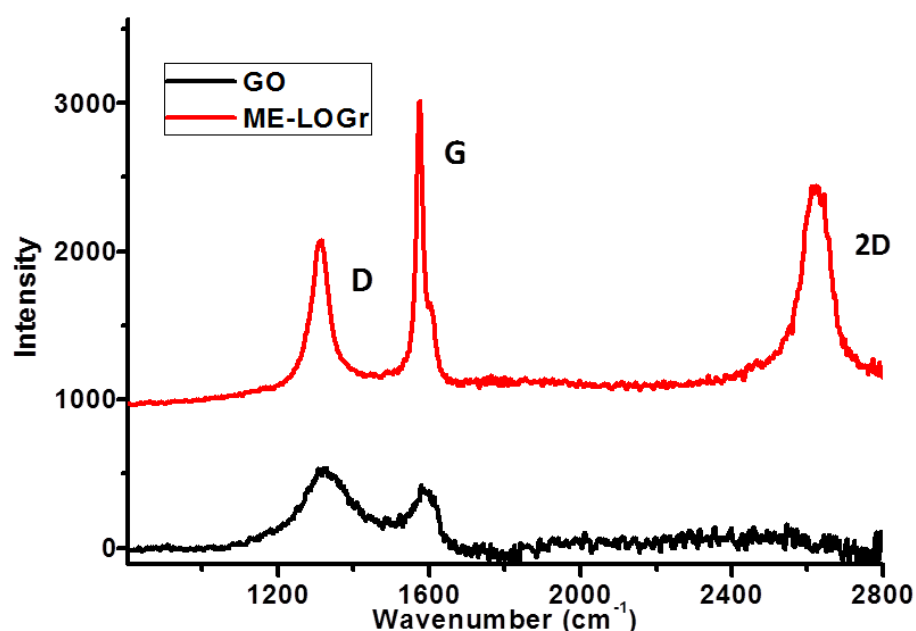
method. Additionally, unlike GO, the UV-Vis-Near IR spectrum of the ME-LOGr solution displayed an absorption maximum at 267 nm and relatively uniform absorption in the visible and NIR region (Figure 2.7), which suggests that the  $\pi$ -conjugation within the graphene sheets is largely retained.[12, 14, 43]



**Figure 2.7:** A UV-Vis spectrum and digital photograph of the graphene solution obtained by adding a small amount of  $\text{KMnO}_4$  in the mixture of  $\text{H}_2\text{SO}_4/\text{HNO}_3$ . The  $\lambda_{\text{max}}$  at 245 nm indicates that this material is heavy oxidized during the 30 seconds of microwave irradiation. The brownish yellow color indicates a high-degree of functionalization of the graphene surface.

Figure 2.8 shows the Raman spectra of ME-LOGr and GO films deposited on alumina membranes. The typical features of the G band, defect D band, and 2D band are shown in the Raman spectrum of ME-LOGr. The D to G band intensity ratio ( $I_D/I_G$ ) is 0.45 and 1.23 for ME-LOGr and GO, respectively. Using the empirical Tuinstra-Koenig relation,[44] we found that the size of the ordered crystallite graphitic domains was  $\approx 10$  nm in ME-LOGr, while the domain size in GO is approximately 3.5 nm. The reported  $I_D/I_G$  ratios for reduced GO (r-GO) are similar to or even higher than GO, which was explained by the fact that chemical

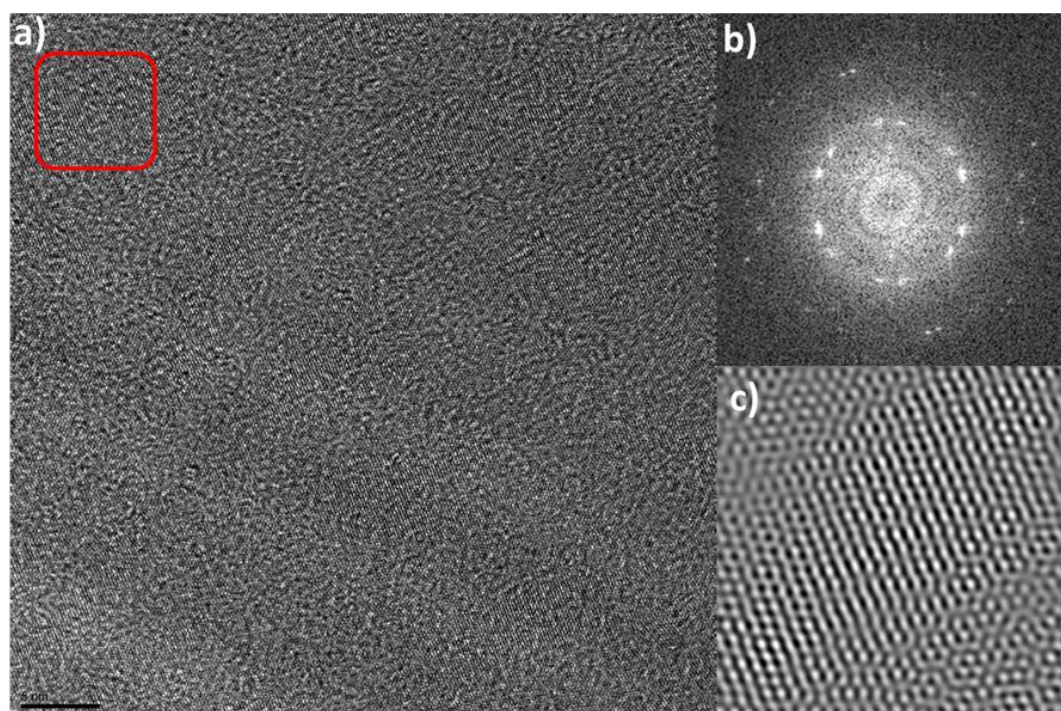
reduction preferentially generates a greater number of smaller crystalline domains rather than increasing the size of existing graphitic domains.[13, 16] Therefore, though the apparent electronic structure of the ME-LOGr sheets is similar to that of r-GO, as demonstrated by its color and UV-Vis spectrum, the ME-LOGr sheets have unique molecular structures that differ from both GO and r-GO.[13, 45]



**Figure 2.8:** Raman spectra of ME-LOGr (red) and GO (black). The small intensity ratio of D/G bands and the high intensity of 2D in ME-LOGr are in contrast to the larger D/G band ratio and the absence of 2D band in GO, indicating ME-LOGr has more ideal graphitic structures without adsorbents induced surface modification.

The 2D band in GO is absent, which is consistent with previous reports.[9, 13] Additionally, the literature states that reduction of GO results in only a small increase in the 2D band due to the defects in the graphitic structures.[16] A

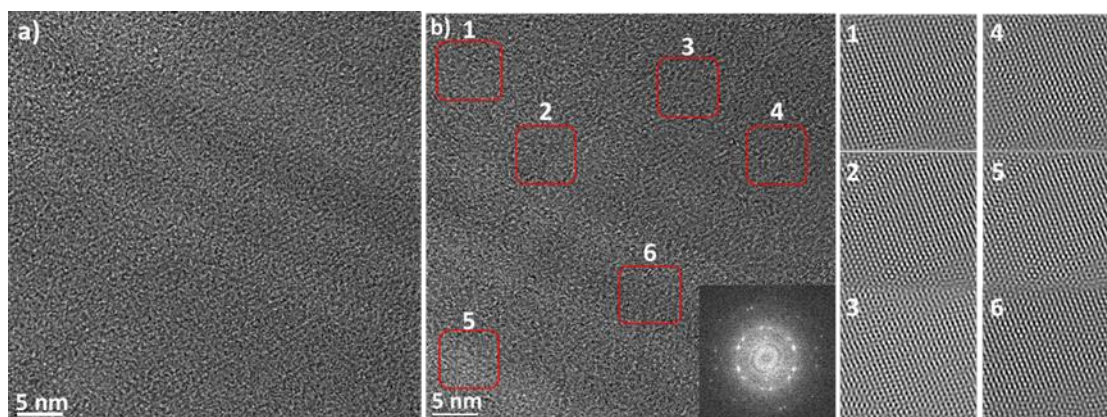
decrease of the 2D band is also associated with the modification of pristine graphene through chemisorption[46] and physisorption.[15, 47] However, for ME-LOGr the intensity of the 2D band is similar to that of the G band, demonstrating a more ideal structure without adsorbent-induced surface modification.[16]



**Figure 2.9:** A representative HRTEM image of ME-LOGr, which is consisted of many different crystalline-like domains with average lateral size of 6-10 nm, there is no nanometer sized holes was observed, which is in highly contrast to GO and rGO. The size of crystalline domains is also much larger than those observed in GO and rGO. b) Fast Fourier transform (FFT) pattern of the selected region, indicated in a). c) The reconstructed image of the same spot as b) after filtering with the frequency domain to include contributions from both sets of hexagons of the FFT pattern. The scale bar in (a) is 5 nm.



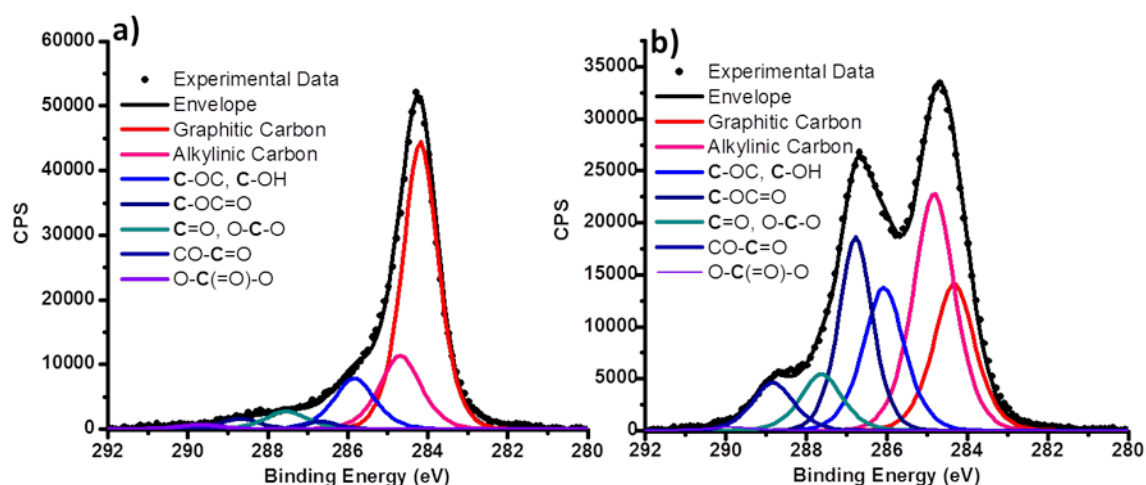
To further understand the structure of the ME-LOGr on an atomic level, we used a low voltage aberration-corrected high resolution transmission electron microscopy (HRTEM) to carefully examine the structure of the ME-LOGr sheets and compare them to what was observed for GO and r-GO.[19, 48] Both GO and r-GO contain nearly perfect graphene domains ranging from 1-3 nm, separated by amorphous-like regions and nanometer sized holes. Additionally, r-GO appears to be more sensitive to the electron beam than GO during TEM imaging. Similar to GO and r-GO, ME-LOGr also exhibits multiple crystalline-like domains connected by amorphous regions. However, the ME-LOGr structure remained stable during imaging and no nanometer sized holes were observed (Figure 2.9) in agreement with the AFM data. In addition to the TEM image, multiple positions



**Figure 2.10:** a) and b) show HRTEM images of a ME-LOGr sheet at two different positions. 1-6 are a series of reconstructed high-resolution images at different positions, as indicated by red boxes in figure S6b. The reconstructed images were obtained by filtering with the frequency domain to include contributions from both sets of hexagons of their respected FFT patterns.



of the ME-LOGr were examined (figure 2.10b); All positions exhibited multiple crystalline-like domains connected by amorphous regions. The crystalline domain sizes are on average 6-10 nm across. Fast Fourier transform (FFT) for all the selected areas shows two sets of six-spots (slightly blurred) with a hexagonal pattern. Blurring diffraction spots were also observed for GO and have been attributed to bond strain occurring at the interface of oxidized and non-oxidized regions in GO. A similar scenario may exist in ME-LOGr. The two sets of hexagonal patterns indicate that two graphene sheets were stacked together. For greater clarity, the selected areas in Figure 2.10b were reconstructed after frequency domain filtering to include contributions from both sets of hexagons from their respective FFT patterns. Unlike the AB Bernal stacking in graphite and mechanically exfoliated few-layer graphene, the reconstructed images show very pronounced, but different Moire patterns, demonstrating that ME-LOGr layers are likely stacked in a turbostratic manner. This stacking structure is characteristic of



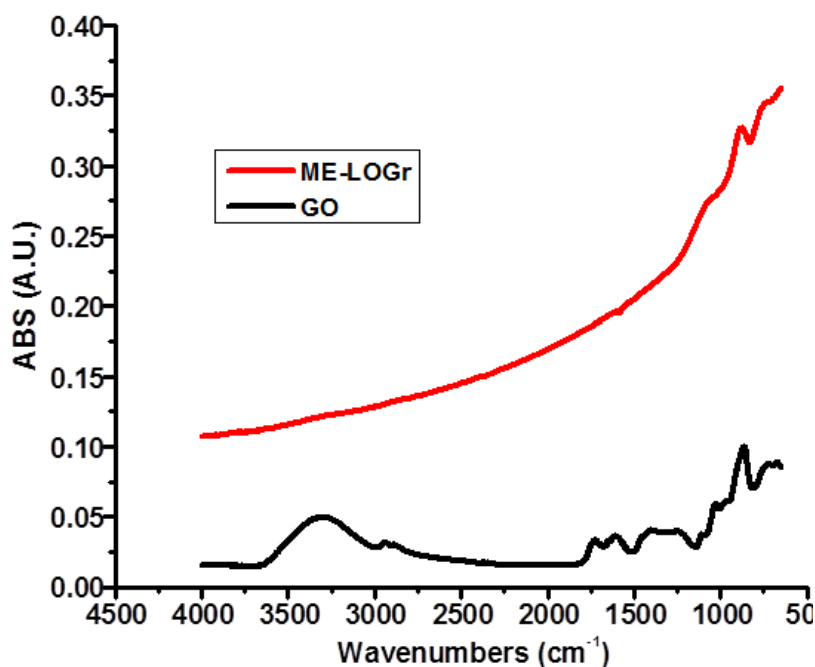
**Figure 2.11:** Carbon 1s core XPS spectra for thin films of (a) ME-LOGr and (b) GO. The content of oxygen-free carbon of ME-LOGr was 79% which was comparable with the reported value of fully reduced GO, while GO (b) contains only 49% of oxygen-free carbon. This is a direct evidence of much less oxidation in the ME-LOGr.

weakly interacting sheets, which has been used to corroborate full oxidation and exfoliation of GO and reduced GO layers.[48, 49] Therefore, the appearance of different Moire patterns may also suggest that a complete exfoliation of graphite was achieved with the microwave irradiation.

The chemical functionalities of the ME-LOGr sheets were studied using X-Ray photoelectron spectroscopy (XPS) and Fourier transform infrared spectroscopy (FTIR). The C 1s core level XPS spectra of ME-LOGr and GO show a main peak of oxygen-free carbon and a shoulder of oxygen-containing carbon (Fig. 2.11), (see methods for details about the data fitting). Further analysis of the XPS spectra helped shed light on the specific bonding present in

each material. The oxygen free carbon is mainly derived from the C 1s peak of aromatic rings (284.2 eV), and that of the aliphatic rings and/or linear alkylinic carbon chains (284.7 eV). The C content from aromatic rings in ME-LOGr is apparently much greater than that in GO. The other peaks are assigned as follows: **C**-OC and **C**-OH (285.8 eV), **C**-OC=O (287.5 eV), **C**=O and **O**-**C**-O (288.7 eV), **O**-**C**(=O)-O (289.7 eV). The oxygen-free carbon of ME-LOGr makes up 79% of the spectrum, comparable to the spectrum of reduced GO.<sup>42</sup> Whereas, the spectrum of GO (Figure 2.11b) contains an oxygen-free carbon signal that is 49% of the total carbon signal, which is much lower than that in ME-LOGr.

Measurements by Rutherford backscattering spectrometry (RBS) show that ME-LOGr exhibits almost an order of magnitude lower oxygen content than that observed in GO films (C:O ratios of 25:1 and 3:1, respectively), consistent with the XPS study. Neither of these two techniques detected nitrogen or sulfur signals in the films, suggesting that no nitration or sulfonation occurred.[50] ATR-FTIR spectra were measured from thin films deposited from ME-LOGr and GO solutions (Figure 2.12). The FTIR spectrum of ME-LOGr shows a main peak at



**Figure 2.12:** ATF-FTIR spectra of ME-LOGr (red) and GO (black) showing that small amount of epoxy and hydroxyl groups in ME-LOGr, while GO is heavily decorated with a variety of oxygen-containing groups.

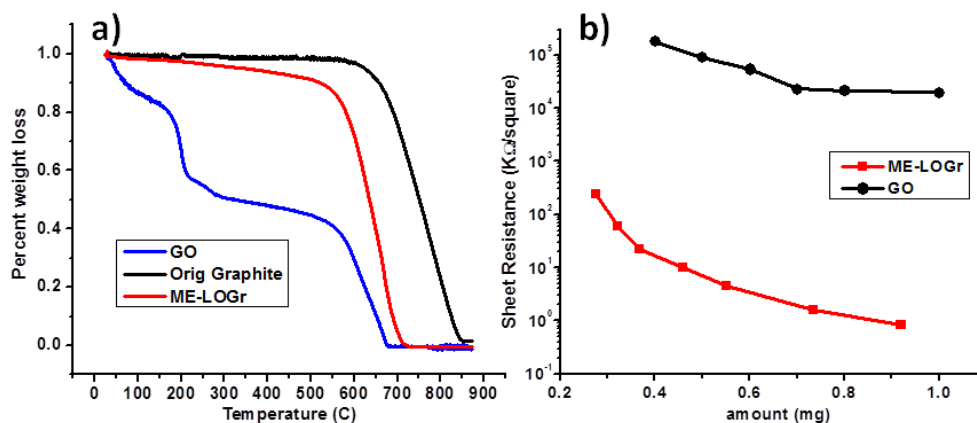
about  $853\text{ cm}^{-1}$ , which is assigned to epoxy or hydroxyl groups, in agreement with the XPS data. The spectrum is otherwise virtually featureless, which is similar to the ones that were reported for intact graphene sheets. However, the spectrum of GO is quite different, showing features characteristic of GO: (i) a strong and broad absorption in the range of  $3000\text{--}3700\text{ cm}^{-1}$  for O-H stretching vibrations mode from free hydroxyl (-OH) groups, and (ii) possible COOH and  $\text{H}_2\text{O}$  vibration mode at  $1210\text{ cm}^{-1}$ , (iii) and the asymmetric bending mode from epoxide (C-O-C) groups at  $853\text{ cm}^{-1}$ , and (iv) stretching vibrations at  $1703\text{ cm}^{-1}$  attributed to carbonyl and carboxylic groups. The XPS contribution from the

oxidized carbon species in ME-LOGr is in agreement with FTIR data that identifies the majority of the functional groups as alcohol and epoxide (Figure 2.12, red). ME-LOGr contains a very small amount of carbonyl containing groups, in contrast to GO. This further illustrates the different oxidation mechanisms of  $\text{NO}_2^+$  and  $\text{KMnO}_4$ .

#### **2.2.6: Thermally stable graphene sheets**

The thermal stability of as-prepared ME-LOGr sheets was compared to GO and the parent graphite powder using thermal gravimetric analysis (TGA) (Figure 2.13a). Below 100 °C the major mass loss has been assigned to desorption of water molecules, even though a complete desorption of water may need higher temperatures.[25] The high concentration of water in GO has been reported to be the result of the high density of oxygen-containing functionalities (including hydroxyl).[51] The minor mass loss of ME-LOGr in this temperature range indicates that the material only exhibits a weak interaction with water behaving similar to the parent graphite powder. At higher temperatures, GO continues losing mass, presumably due to pyrolysis of the labile oxygen-containing functional groups.[25, 52, 53] The sharp mass loss that occurred around 200-300°C has been assigned to pyrolysis of hydroxyl, epoxide, and carboxyl groups.[54, 55] The low weight loss in these temperature ranges further suggests the low concentration of hydroxyl, epoxide and carboxyl groups in the ME-LOGr sheets, which is consistent with the XPS results. The sharp mass loss above 500 °C has been ascribed to the combustion of carbon in the graphene

backbone.[56] It is interesting to note that even though the rate of mass loss of GO and ME-LOGr was similar between 300 ~ 500 °C, the complete combustion for ME-LOGr happens at a higher temperature than GO. This result indicates that the ME-LOGr may have better thermal stability than thermally reduced GO sheets.



**Figure 2.13:** (a) TGA curves of % weight loss plotted against temperature, showing that ME-LOGr (red) is thermally much more stable than GO (blue), and highly comparable with its parent graphite (black). (b) Percolation study of ME-LOGr and GO using a 4-point probe setup. After percolation threshold, the sheet resistivity of ME-LOGr (red) shows 5 orders of magnitude lower than the heavily oxidized GO films.

Recently, the evolution of carbon bonds in GO thin films has been carefully studied by monitoring XPS and infrared differential spectra as a function of annealing temperatures.[25, 52, 53] Thermal annealing of GO has been shown to result in the removal of the entrapped water molecules and the epoxide and

hydroxyl groups by formation of  $\text{H}_2\text{O}$ ,  $\text{H}_2$ ,  $\text{O}_2$ ,  $\text{CO}$  and  $\text{CO}_2$ , thus creating defects in the form of etched holes within the graphene basal plane.[57] Zettl, et al. reported on the existence of a large number of holes and vacancies in r-GO obtained by a combination of chemical and thermal reduction. They found the presence of these defects dramatically decreases the stability of r-GO to the electron beam during TEM imaging.[19] The higher thermal stability of the ME-LOGr is consistent with the TEM observation that the structure of ME-LOGr is stable during imaging and contains no holes and fewer defects.

#### **2.2.7: Conductive nature of graphene sheets:**

We prepared graphene films of different thicknesses from the ME-LOGr suspensions by vacuum filtration through an anodic filter membrane.[9] The electrical properties of the graphene sheets without any chemical and thermal reduction processes were studied by measuring the sheet resistance of the corresponding graphene films with a four-probe approach. Similar to other methods that utilize graphene sheets dispersed in solutions, the ME-LOGr films show percolation-type electronic behavior. The sheet resistance of the ME-LOGr film decreases with increasing film thickness, as shown in Figure 2.13b. After reaching the percolation threshold, the sheet resistance of the ME-LOGr film is 1.0 k $\Omega$ /square.

To estimate the DC conductivity of the film, a filtered ME-LOGr film was divided to two parts. One part was transferred onto a quartz substrate for

conductivity measurement and the other half was transferred onto a beryllium substrate to precisely measure the thickness of the film (see detail in supplementary materials). The sheet resistance was measured to be 0.76 k $\Omega$ /square and the thickness of the film is for 200 nm. This corresponds to a DC conductivity of 6600 S m<sup>-1</sup>. It is worthy to mention that this conductivity was achieved on the as-prepared film which has been neither chemically nor thermally reduced. This conductivity is much higher than graphene directly exfoliated in the presence of surfactants/stabilizers even though they were known to have a low density of defects. For instance, the graphene sheets dispersed in the sodium dodecylbenzene sulfonate (SDBS) has a DC conductivity of 35 S m<sup>-1</sup>.<sup>[15]</sup> Recently, we reported that the DC conductivity of the graphene sheets dispersed in the presence of pyrene derivatives before thermal annealing was around 1900 S m<sup>-1</sup>.<sup>[18]</sup> The conductivity of the as-produced ME-LOGr is much more comparable to surfactant-free reduced GO sheets obtained by hydrazine reduction under basic conditions (DC conductivity of 7200 S m<sup>-1</sup>).<sup>[12]</sup>

We believe that the high conductivity is due to the high conductivity as well as the relative cleanliness (non-functionalization) of the individual ME-LOGr sheets, which enables low inter-sheet contact resistance. It is known that directly exfoliating graphite in certain organic solvents, such as N-methyl-pyrrolidone (NMP), can produce graphene sheets with not only a low density of defects, but also clean surfaces without any surfactants or stabilizers. However, these solvents are expensive, require special care, tend to have high boiling points,



and are difficult to completely remove. Residual solvent also results in poor electronic contacts between graphene sheets and therefore lowers the overall conductivity of the resulting multisheet graphene films. It was reported that the as-produced film has a conductivity of  $5 \text{ S m}^{-1}$ . [14] After thermal annealing at  $300^\circ\text{C}$  for 2 hours, a conductivity of  $5000 \text{ S m}^{-1}$  was achieved. With annealing in a reductive environment ( $\text{Ar}/\text{H}_2$ ) at  $250^\circ\text{C}$  for 2 hours, a slightly higher conductivity of  $6500 \text{ S m}^{-1}$  was achieved. [14] Upon annealing a ME-LOGr film at  $300^\circ\text{C}$  in Ar for 2 hours to remove some of the oxygen containing groups, the conductivity was increased to  $19,200 \text{ S m}^{-1}$ , significantly higher than those films prepared via graphene dispersed by NMP and hydrazine reduced GO in basic conditions.

We emphasize that microwave methodologies are easy to scale and do not suffer from thermal gradient effects, providing a potentially industrially important improvement over convective methods. [30] Microwave irradiation was also exploited for other graphene research projects. For example, it has been applied to fabricate exfoliated graphite (EG) from a wide range of graphite intercalation compounds (GIC), [58] simultaneous exfoliation and reduction of GO, [59] and simultaneous intercalation and exfoliation of graphite powder. [60] However, this is the first report that large, clean, and highly conductive graphene of an intrinsically amphiphilic nature can be directly and rapidly produced with high yield. By eliminating extensive cuttings and formations of nanosized holes, which decrease the graphene integrity, and thus significantly alter the electrical

and thermal conductivity, mechanical strength, and molecular permeability are much improved compared to heavily modified GO.[21]

### **2.3: CONCLUSION**

An unprecedented, fast and scalable approach has been developed to directly produce large, highly-conductive graphene sheets. This method has the following advantages for mass production: (1) short production periods (30s); (2) much larger sheet size (400-900  $\mu\text{m}^2$ ), (3) fewer destructive defects such as nanometer sized holes; (4) high-concentration dispersions both in aqueous and organic solvents (without requiring polymeric or surfactant stabilizers); (5) fewer starting materials and low-cost (compared to commonly used Hummers' and modified Hummers'); and (6) reduced waste from purification steps. This process can enable a broad range of real-world applications to be realized using solution processing.

### **2.4: MATERIALS AND METHODS:**

#### **2.4.1: Materials**

Synthetic graphite powder ( $\sim 20 \mu\text{m}$ ) used in all experiments was purchased from Sigma Aldrich and used as received. ACS grade concentrated sulfuric acid (98%  $\text{H}_2\text{SO}_4$ ) and concentrated nitric acid (70%  $\text{HNO}_3$ ) were purchased from Pharmco-AAPER and used as received. All solutions were prepared using deionized water (18.2 M $\Omega$ ) (Nanopure water, Barnstead), which is also used to rinse and clean the samples.

#### **2.4.2: Using microwave heating to directly produce slightly oxidized graphene sheets (ME-LOGr).**

In a typical experiment, 20 mg of synthetic graphite powder is added to a mixture of sulfuric acid and nitric acid (ratio of 1:1 with a total volume of 10 mL) in a round bottom flask. The mixture is then swirled and mixed, and then placed into a CEM Discover microwave reactor chamber. The flask is connected to a reflux condenser that passes through the roof of the microwave oven via a port and is subjected to 30s of 300 watt microwave irradiation. A colloidal ME-LOGr solution was directly obtained by removing the excess acid with 4M NaOH in the formed suspension via extensive dialysis through a membrane with a molecular weight cutoff of 30,000. To speed up the cleaning procedure, the formed suspension is then filtered through an Anodisc alumina filter membrane with 0.2  $\mu\text{m}$  pore size, and is washed with 600 mL of deionized water. The filtrand is then re-dispersed into water with a 30 minute bath sonication. The obtained grey dispersion was then centrifuged at 4000 r.p.m. for 20 minutes to remove the small amount of unexfoliated graphite using a Beckman J2-21 centrifuge. The supernatant was then carefully decanted and all visible agglomerates were avoided, forming the stock ME-LOGr solution. This solution is stable for months without significant precipitation. The yield of graphene sheets was estimated to be 50% by weight. The resulting solution was directly used to prepare graphene films with a vacuum filtration method for conductivity measurements.

A control experiment was performed by adding a small amount (0.65 g) of  $\text{KMnO}_4$  into the  $\text{HNO}_3/\text{H}_2\text{SO}_4$  mixture prior to the microwave irradiation. The

solution was then neutralized using 4M NaOH, and extensive dialysis was performed to completely remove the resulting salt and ions.

#### **2.4.3: Synthesis of GO**

Graphene oxide was synthesized using the modified Hummer's method from the same graphite powder mentioned above. In a typical preparation, 0.5 g of graphite, 0.5 g of NaNO<sub>3</sub> and 23 mL of H<sub>2</sub>SO<sub>4</sub> were stirred and mixed until homogenized in an ice bath. Then 3 g of KMnO<sub>4</sub> was gradually added into the reaction over 1 hour while continuing stirring. The reaction temperature was maintained at about 35 °C in a water bath. After 1 hour, 40 mL of water was then added to the thick brownish paste. The solution was stirred for another 30 minutes after the temperature was stabilized at 95 °C. 100 mL more of DI water was then added to the solution, followed by 3 mL of 35% H<sub>2</sub>O<sub>2</sub> while the temperature of the solution was still maintained at around 95 °C. Upon the addition of H<sub>2</sub>O<sub>2</sub>, the color of the solution turned from dark brown to yellow. Finally, this warm and yellowish solution was filtered with a 0.2 µm polycarbonate filter and was extensively washed with 1L of DI water to remove all traces of acid and metal ions. Because of the paste-like characteristic of the final products, we took one-fifth of it at a time for filtration and cleaning, which usually takes from 6 hours to overnight, to remove away all the ions and acids. The following day this filter cake was then re-dissolved into DI-water with mild sonication, forming GO stock solutions.

#### **2.4.4: Characterizations**

##### **2.4.4.1: Atomic force microscopy (AFM)**

The morphology of the ME-LOGr and GO samples were studied using a Nanoscope IIIa multimode SPM (Digital Instrument) with a J scanner operated in “Tapping Mode”. AFM samples were prepared by slowly dip-coating freshly cleaved mica into the graphene solution, and by slowly removing the mica from the solution at a rate of 1mm/min. The mica surface was rinsed with 20  $\mu$ L of DI water and dried in a fume hood for 20-30 mins. During imaging, a 125  $\mu$ m long rectangular silicon cantilever/tip assembly (Model: MPP-12100, Veeco) was used with a resonance frequency between 127-170 kHz, a spring constant of approximately 5 N/m, and a tip radius of less than 10 nm. The applied frequency was set on the lower side of the resonance frequency and the scan rate was  $\sim$ 1.0 Hz. Height differences were obtained from section analysis of the topographic images.

##### **2.4.4.2: Raman spectroscopy**

Raman spectroscopy has been used extensively to characterize graphene materials because it is a direct and non-destructive method that gives very useful information about the quality of the graphene. Raman spectra from films deposited on alumina membranes using Buchner filtration were collected in a Kaiser Optical Systems Raman Microprobe with a 785 nm solid state diode laser. Spectra were acquired using a 30 s exposure time.

#### **2.4.4.3: TEM**

We characterized the ME-LOGr sheets using a Zeiss 200 kV Cs Corrected Libra 200 FEG energy-filtering transmission electron microscope (EF-TEM) at an accelerating voltage of 80 kV. The TEM samples were prepared by drying a droplet of the graphene suspension on a lacey carbon grid.

#### **2.4.4.4: X-ray photoelectron spectroscopy (XPS) and Rutherford backscattering spectroscopy (RBS)**

XPS characterization was performed after depositing a ME-LOGr or a GO suspension onto a gold film (a 100 nm gold layer was sputter-coated on silicon with a 10 nm Ti adhesion layer). The thickness of the ME-LOGr or GO film on the gold substrates was roughly 30-50 nm. XPS spectra were acquired using a Thermo Scientific K-Alpha system with a monochromated Al K $\alpha$  x-ray source ( $h\nu$  = 1486.7 eV) and a hemispherical analyzer. Energy calibration was performed in-situ with an ion-sputtered Au foil (Sigma Aldrich, 99.999% pure) with the Au 4f 7/2 peak centered at a binding energy of 83.9 eV with a FWHM of 0.9 eV. Prior to sputtering, adventitious carbon (aliphatic) on the same foil possessed a binding energy of 284.7 eV and a FWHM of 1.2 eV, in agreement with literature values.[61] To compensate for charging in the GO sample, a rigid energy shift was applied to samples so that the underlying Au substrate matched the values of the Au foil; no such correction was required with the ME-LOGr film.

The peak-fitting routine employed in this project (Casa XPS) was found to reproducibly provide good data fits for various forms of carbon (GO, ME-LOGr, CNTs). A Shirley background removal was applied prior to fitting. Individual peak

shapes were fit with a symmetric Gaussian-Laurentz hybrid function. The FWHM of deconvoluted peaks are a combination of intrinsic photoelectron core-hole lifetimes and instrumental broadening. The combined broadening effects are found to limit the FWHM to  $\sim 0.9$  eV for C1s and Au 4f  $7/2$  levels. We allowed the FWHM to float within the range of 0.9-1.2 eV in our fitting algorithm. Relative binding energies for the different carbon species were obtained from the work of Briggs and Beamson and are related to the absolute energy value for adventitious carbon as noted above. The graphitic carbon peak was assigned a fixed energy of 284.2 per the literature value of HOPG.[62] Finally, a least squares fit was performed to determine the height and area (and width, within the range noted above) for each peak.

Rutherford back scattering (RBS) was performed using a 2 MeV  $\text{He}^{2+}$  ion beam produced in a tandem accelerator with an ion current of 2–3 nA. Spectra were collected in the back scattering geometry and simulations were performed using the SIMNRA program. Samples consisted of thick (several tens of  $\mu\text{m}$ ) films of GO and ME-LOGr deposited onto HOPG and thin ( $\sim 200$  nm) films of ME-LOGr onto beryllium foil (99.5% pure, Sigma Aldrich) .

#### **2.4.4.5: Thermogravimetric Analysis (TGA)**

TGA was performed with a nitrogen flow (20ml/min) using a Perkin Elmer Thermogravimetric Analyzer Pyris 1 TGA on sample sizes of about 2-3 mg, and the mass was recorded as a function of temperature. The samples in the TGA furnace were heated from room temperature to 1000 °C at a rate of 5 °C/min.

**2.4.4.6: Optical and electrical properties of dispersed graphene sheets.**

UV-vis-NIR absorption spectroscopy was used to characterize the electronic states of the exfoliated graphene sheets. All spectra were obtained using a Cary 500 Ultraviolet-visible-near-infrared spectrophotometer in double-beam mode. Graphene films of different thicknesses were prepared by Buchner vacuum filtration of the corresponding suspensions onto Anodisc 47 inorganic membranes with 200 nm pores (Whatman Ltd.). After filtration, the thin films were dried in air for 15-20 min before conductivity measurements. The sheet resistance of the films was determined by a manual four point resistivity probe (Lucas Laboratories, model 302).

**2.4.4.7: SEM and STEM**

SEM samples were prepared by spin-coating a stirred, exfoliated graphene solution onto SiO<sub>2</sub>/Si substrates. The substrates were first cleaned with a UV/Ozone treatment for 10 minutes, followed by 5 minutes in piranha solution, and finally treated with 2% APTES solution in toluene. The modified substrates were then fully covered by the graphene solution for 10s, followed by spinning at 3000 rpm for 2 minutes. SEM images were collected using a Hitachi S-4800 field emission scanning electron microscope (FE-SEM, Hitachi Co. Ltd. S-4800) under small accelerating voltage (1-2 KV) and a high probe current (15-20  $\mu$ A) to obtain images with high contrast. Samples for STEM imaging were prepared by adding a small drop of the same graphene solution onto a holey carbon on Cu grid (Ted Pella, Inc.) and air dried. STEM images were collected with the same FE-SEM,



with an acceleration voltage of 25 - 30 kV, working at a distance of 8.6 mm, and a probe current of 8  $\mu$ A.

## 2.5: REFERENCES:

1. Wu, Y.Q., Lin, Y.M., Bol, A.A., Jenkins, K.A., Xia, F.N., Farmer, D.B., Zhu, Y., and Avouris, P., *High-frequency, scaled graphene transistors on diamond-like carbon*. Nature, 2011. **472**(7341): p. 74-78.
2. Zhu, Y., Murali, S., Stoller, M.D., Ganesh, K.J., Cai, W., Ferreira, P.J., Pirkle, A., Wallace, R.M., Cychosz, K.A., Thommes, M., Su, D., Stach, E.A., and Ruoff, R.S., *Carbon-Based Supercapacitors Produced by Activation of Graphene*. Science, 2011. **332**: p. 1537-1541.
3. Jin, Z., Lu, W., O'Neill, K.J., Parilla, P.A., Simpson, L.J., Kittrell, C., and Tour, J.M., *Nano-Engineered Spacing in Graphene Sheets for Hydrogen Storage*. Chemistry of Materials, 2011. **23**(4): p. 923-925.
4. Eda, G. and Chhowalla, M., *Chemically Derived Graphene Oxide: Towards Large-Area Thin-Film Electronics and Optoelectronics*. Advanced Materials, 2010. **22**(22): p. 2392-2415.
5. Wobkenberg, P.H., Eda, G., Leem, D.S., de Mello, J.C., Bradley, D.D.C., Chhowalla, M., and Anthopoulos, T.D., *Reduced Graphene Oxide Electrodes for Large Area Organic Electronics*. Advanced Materials, 2011. **23**(13): p. 1558-1562.
6. Dubin, S., Gilje, S., Wang, K., Tung, V.C., Cha, K., Hall, A.S., Farrar, J., Varshneya, R., Yang, Y., and Kaner, R.B., *A One-Step, Solvothermal Reduction Method for Producing Reduced Graphene Oxide Dispersions in Organic Solvents*. ACS Nano, 2010. **4**(7): p. 3845-3852.
7. Stankovich, S., Dikin, D.A., Dommett, G.H.B., Kohlhaas, K.M., Zimney, E.J., Stach, E.A., Piner, R.D., Nguyen, S.T., and Ruoff, R.S., *Graphene-based composite materials*. Nature, 2006. **442**(7100): p. 282-286.
8. Ramanathan, T., Abdala, A.A., Stankovich, S., Dikin, D.A., Herrera-Alonso, M., Piner, R.D., Adamson, D.H., Schniepp, H.C., Chen, X., Ruoff, R.S., Nguyen, S.T., Aksay, I.A., Prud'homme, R.K., and Brinson, L.C., *Functionalized graphene sheets for polymer nanocomposites*. Nature Nanotechnology, 2008. **3**(6): p. 327-331.
9. Eda, G., Fanchini, G., and Chhowalla, M., *Large-Area Ultrathin Films of Reduced Graphene Oxide as a Transparent and Flexible Electronic Materials*. Nature Nanotech., 2008. **3**: p. 270-274.
10. Behabtu, N., Lomeda, J.R., Green, M.J., Higginbotham, A.L., Sinitskii, A., Kosynkin, D.V., Tsentelovich, D., Parra-Vasquez, A.N.G., Schmidt, J.,

- Kesselman, E., Cohen, Y., Talmon, Y., Tour, J.M., and Pasquali, M., *Spontaneous high-concentration dispersions and liquid crystals of graphene*. Nature Nanotechnology, 2010. **5**(6): p. 406-411.
11. Li, X.L., Zhang, G.Y., Bai, X.D., Sun, X.M., Wang, X.R., Wang, E., and Dai, H.J., *Highly conducting graphene sheets and Langmuir-Blodgett films*. Nature Nanotechnology, 2008. **3**(9): p. 538-542.
  12. Li, D., Muller, M.B., Gilje, S., Kaner, R.B., and Wallace, G.G., *Processable aqueous dispersions of graphene nanosheets*. Nature Nanotechnology, 2008. **3**(2): p. 101-105.
  13. Tung, V.T., Allen, M.J., Yang, Y., and Kaner, R.B., *High-throughput Solution Processing of Large-scale Graphene*. Nature Nanotech., 2009. **4**: p. 25-29.
  14. Hernandez, Y., Nicolosi, V., Lotya, M., Blighe, F.M., Sun, Z.Y., De, S., McGovern, I.T., Holland, B., Byrne, M., Gun'Ko, Y.K., Boland, J.J., Niraj, P., Duesberg, G., Krishnamurthy, S., Goodhue, S., Hutchison, J., Scardaci, V., Ferrari, A.C., and Coleman, J.N., *High-yield Production of Graphene by Liquid-Phase Exfoliation of Graphite*. Nature Nanotech., 2008. **3**: p. 563 - 568.
  15. Lotya, M., Hernandez, Y., King, P.J., Smith, R.J., Nicolosi, V., Karlsson, L.S., Blighe, F.M., De, S., Wang, Z., McGovern, I.T., Duesberg, G.S., and Coleman, J.N., *Liquid Phase Production of Graphene by Exfoliation of Graphite in Surfactant/Water Solutions*. J. Am. Chem. Soc., 2009. **131**: p. 3611-3620
  16. Moon, I.K., Lee, J., Ruoff, R.S., and Lee, H., *Reduced graphene oxide by chemical graphitization*. Nature Communications, 2010. **1**: p. 73.
  17. Wang, J.Z., Manga, K.K.M., Bao, Q.L., and Loh, K.P., *High-Yield Synthesis of Few -Layer Graphene Flakes through Electrochemical Expansion of Graphite in Propylene Carbonate Electrolyte*. J. Am. Chem. Soc., 2011. **133**: p. 8888-8891.
  18. Zhang, M., Parajuli, R.R., Mastrogiovanni, D., Dai, B., Lo, P., Cheung, W., Brukh, R., Chiu, P.L., Zhou, T., Liu, Z.F., Garfunkel, E., and He, H.X., *Production of Graphene Sheets by Direct Dispersion with Aromatic Healing Agents*. Small, 2010. **6**(10): p. 1100-1107.

19. Erickson, K., Erni, R., Lee, Z., Alem, N., Cannett, W., and A., Z., *Determination of the Local Chemical Structure of Graphene Oxide and Reduced Graphene Oxide*. Advanced Materials, 2010. **22**: p. 4467-4472.
20. Li, J.-L., Kudin, K.N., McAllister, M.J., Prud'homme, R.K., Aksay, I.A., and Car, R., *Oxygen-Driven Unzipping of Graphitic Materials* Phys. Rev. Lett., 2006. **96**: p. 176101.
21. Geim, A.K., *Graphene: Status and Prospects*. Science, 2009. **324**: p. 1530-1534.
22. Zhu, C.Z., Guo, S.J., Fang, Y.X., and Dong, S.J., *Reducing Sugar: New Functional Molecules for the Green Synthesis of Graphene Nanosheets*. ACS Nano, 2010. **4**(4): p. 2429-2437.
23. Ziegler, K.J., Gu, Z.N., Peng, H.Q., Flor, E.L., Hauge, R.H., and Smalley, R.E., *Controlled Oxidative Cutting of Single-Walled Carbon Nanotubes*. J. Am. Chem. Soc., 2005. **127**: p. 1541.
24. Liu, J., Rinzler, A.G., Dai, H.J., Hafner, J.H., Bradley, R.K., Boul, P.J., Lu, A., Iverson, T., Shelimov, K., Huffman, C.B., Rodriguez-Macias, F., Shon, Y.S., Lee, T.R., Colbert, D.T., and Smalley, R.E., *Fullerene pipes*. Science, 1998. **280**(5367): p. 1253-1256.
25. Bagri, A., Mattevi, C., Acik, M., Chabal, Y.J., Chhowalla, M., and Shenoy, V.B., *Structural evolution during the reduction of chemically derived graphene oxide*. Nature Chemistry, 2010. **2**(7): p. 581-587.
26. Kosynkin, D.V., Higginbotham, A.L., Sinitskii, A., Lomeda, J.R., Dimiev, A., Price, B.K., and Tour, J.M., *Longitudinal unzipping of carbon nanotubes to form graphene nanoribbons*. Nature, 2009. **458**(7240): p. 872-6.
27. Esteves, P.M., Carneiro, J.W.D., Cardoso, S.P., Barbosa, A.G.H., Laali, K.K., Rasul, G., Prakash, G.K.S., and Olah, G.A., *Unified mechanistic concept of electrophilic aromatic nitration: Convergence of computational results and experimental data*. Journal of the American Chemical Society, 2003. **125**(16): p. 4836-4849.
28. de Queiroz, J.F., Carneiro, J.W.D., Sabino, A.A., Sparrapan, R., Eberlin, M.N., and Esteves, P.M., *Electrophilic aromatic nitration: Understanding its mechanism and substituent effects*. Journal of Organic Chemistry, 2006. **71**(16): p. 6192-6203.

29. Loughin, S., Grayeski, R., and Fischer, J.E., *Charge Transfer in Graphite Nitrate and the Ionic Salt Model*. J. Chem. Phys. , 1978. **69**: p. 3740-3745.
30. (Skip) Kingston, H.M. and Haswell, S.J., eds. *Microwave-Enhanced Chemistry: Fundamentals, Sample Preparation, and Applications*. 1997, American chemical society: Washington DC.
31. Jung, I., Dikin, D.A., Piner, R.D., and Ruoff, R.S., *Tunable Electrical Conductivity of Individual Graphene Oxide Sheets Reduced at "Low" Temperatures*. Nano Letters, 2008. **8**(12): p. 4283-4287.
32. Paci, J.T., Belytschko, T., and Schatz, G.C., *Computational Studies of the Structure, Behavior upon Heating, and Mechanical Properties of Graphite Oxide*. J. Phys. Chem. C, 2007. **111**: p. 18099-18111.
33. Liu, J., Rinzler, A.G., Dai, H.J., Hafner, J.H., Bradley, P.K., Boul, P.J., Lu, A., Iverson, T., Shelimov, K., Huffman, C.B., Rodriguez-Macias, F., Shon, Y., Lee, T.R., Colbert, D.T., and Smalley, R.E., *Fullerene Pipes*. Science, 1998. **280**: p. 1253-1256.
34. Ziegler, K.J., Gu, Z.N., Peng, H.Q., Flor, E.L., Hauge, R.H., and Smalley, R.E., *Controlled Oxidative Cutting of Single-Walled Carbon Nanotubes*. J. Am. Chem. Soc., 2005. **127**: p. 1541-1547.
35. An, K.H., Park, J.S., Yang, C.M., Jeong, S.Y., Lim, S.C., Kang, C., Son, J.H., Jeong, M.S., and Lee, Y.H., *A diameter-selective attack of metallic carbon nanotubes by nitronium ions*. Journal of the American Chemical Society, 2005. **127**(14): p. 5196-5203.
36. McKay, S.F., *Expansion of Annealed Pyrolytic Graphite* J. Appl. Phys. , 1964. **35**: p. 1992-1993.
37. Higginbotham, A.L., Kosynkin, D.V., Sinitskii, A., Sun, Z.Z., and Tour, J.M., *Lower-Defect Graphene Oxide Nanoribbons from Multiwalled Carbon Nanotubes*. ACS Nano, 2010. **4**(4): p. 2059-2069.
38. Marcano, D.C., Kosynkin, D.V., Berlin, J.M., Sinitskii, A., Sun, Z.Z., Slesarev, A., Alemany, L.B., Lu, W., and Tour, J.M., *Improved Synthesis of Graphene Oxide*. ACS Nano, 2010. **4**(8): p. 4806-4814.
39. Zhang, J., Zou, H.L., Qing, Q., Yang, Y.L., Li, Q.W., Liu, Z.F., Guo, X.Y., and Du, Z.L., *Effect of chemical oxidation on the structure of single-walled carbon nanotubes*. Journal of Physical Chemistry B, 2003. **107**(16): p. 3712-3718.

40. Forsman, W.C. and Mertwoy, H.E., *Intercalation of Graphite by Nitronium Ion Attack*. Synthetic Metals, 1980. **2**: p. 171-176.
41. Hummers, W.S. and Offeman, R.E., *Preparation of Graphitic Oxide*. J. Am. Chem. Soc., 1958. **80**: p. 1339.
42. Qi, X.Y., Pu, K.Y., Li, H., Zhou, X.Z., Wu, S.X., Fan, Q.L., Liu, B., Boey, F., Huang, W., and Zhang, H., *Amphiphilic Graphene Composites*. Angewandte Chemie-International Edition, 2010. **49**(49): p. 9426-9429.
43. Becerril, H.A., Mao, J., Liu, Z.F., Stoltenberg, R.M., Bao, Z., and Chen, Y.S., *Evaluation of Solution-Processed Reduced Graphene Oxide Films as Transparent Conductors*. ACS Nano, 2008. **2**: p. 463–470.
44. Tuinstra, F. and Koenig, J.L., *Raman spectrum of graphite*. J. Chem. Phys., 1970. **53**: p. 1126–1130.
45. Wang, H.L., Robinson, J.T., Li, X.L., and Dai, H.J., *Solvothermal Reduction of Chemically Exfoliated Graphene Sheets*. J. Am. Chem. Soc., 2009. **131**: p. 9910–9911.
46. Niyogi, S., Bekyarova, E., Itkis, M.E., Zhang, H., Shepperd, K., Hicks, J., Sprinkle, M., Berger, C., Lau, C.N., Deheer, W.A., Conrad, E.H., and Haddon, R.C., *Spectroscopy of Covalently Functionalized Graphene*. Nano Letters, 2010. **10**(10): p. 4061-4066.
47. Farmer, D.B., Golizadeh-Mojarad, R., Perebeinos, V., Lin, Y.M., Tulevski, G.S., Tsang, J.C., and Avouris, P., *Chemical Doping and Electron-Hole Conduction Asymmetry in Graphene Devices*. Nano Letters, 2009. **9**(1): p. 388-392.
48. Go´mez-Navarro, C., Meyer, J.C., Sundaram, R.S., Chuvilin, A., Kurasch, S., Burghard, M., Kern, K., and Kaiser, U., *Atomic Structure of Reduced Graphene Oxide*. Nano Letters, 2010. **10**: p. 1144–1148.
49. Warner, J.H., Rummeli, M.H., Gemming, T., Buchner, B., and Briggs, G.A.D., *Direct Imaging of Rotational Stacking Faults in Few Layer Graphene*. Nano Letters, 2009. **9**: p. 102-106.
50. Wang, Y.B., Iqbal, Z., and Mitra, S., *Rapidly functionalized, water-dispersed carbon nanotubes at high concentration*. Journal of the American Chemical Society, 2006. **128**(1): p. 95-99.

51. Acik, M., Mattevi, C., Gong, C., Lee, G., Cho, K., Chhowalla, M., and Chabal, Y.J., *The Role of Intercalated Water in Multilayered Graphene Oxide*. ACS Nano, 2010. **4**(10): p. 5861-5868.
52. Acik, M., Lee, G., Mattevi, C., Chhowalla, M., Cho, K., and Chabal, Y.J., *Unusual infrared-absorption mechanism in thermally reduced graphene oxide*. Nature Materials, 2010. **9**(10): p. 840-845.
53. Mattevi, C., Eda, G., Agnoli, S., Miller, S., Mkhoyan, K.A., Celik, O., Mastrogiovanni, D., Granozzi, G., Garfunkel, E., and Chhowalla, M., *Evolution of Electrical, Chemical, and Structural Properties of Transparent and Conducting Chemically Derived Graphene Thin Films* Adv. Funct. Mater. , 2009. **19**: p. 2577-2583.
54. Kittaka, S., Fukuhara, N., and Sumida, H., *THERMAL-DESORPTION OF N-ALCOHOLS INTERCALATED IN VANADIUM PENTAOXIDE HYDRATE*. Journal of the Chemical Society-Faraday Transactions, 1993. **89**(20): p. 3827-3832.
55. Boehm, H.P., *Surface oxides on carbon and their analysis: a critical assessment*. Carbon, 2002. **40**(2): p. 145-149.
56. Jeong, H.K., Jin, M.H., So, K.P., Lim, S.C., and Lee, Y.H., *Tailoring the characteristics of graphite oxides by different oxidation times*. Journal of Physics D-Applied Physics, 2009. **42**(6).
57. Jung, I., Field, D.A., Clark, N.J., Zhu, Y.W., Yang, D.X., Piner, R.D., Stankovich, S., Dikin, D.A., Geisler, H., Ventrice, C.A., and Ruoff, R.S., *Reduction Kinetics of Graphene Oxide Determined by Electrical Transport Measurements and Temperature Programmed Desorption*. Journal of Physical Chemistry C, 2009. **113**(43): p. 18480-18486.
58. Luo, Z.T., Lu, Y., Somers, L.A., and Johnson, A.T.C., *High Yield Preparation of Macroscopic Graphene Oxide Membranes*. J. Am. Chem. Soc., 2009. **131**: p. 898–899.
59. Zhu, Y.W., Murali, S., Stoller, M.D., Velamakanni, A., Piner, R.D., and Ruoff, R.S., *Microwave assisted exfoliation and reduction of graphite oxide for ultracapacitors*. Carbon, 2010. **48**(7): p. 2118-2122.
60. Sridhar, V., Jeon, J.H., and Oh, I.K., *Synthesis of graphene nano-sheets using eco-friendly chemicals and microwave radiation*. Carbon, 2010. **48**(10): p. 2953-2957.

61. Barr, T.L. and Seal, S., *Nature of the use of adventitious carbon as a binding energy standard*. J Vac Sci Technol A, 1995. **13**: p. 1239.
62. Morar, J.F., Himpsel, F.J., Hollinger, G., Jordan, J.L., Huges, G., and McFeely, F.R., Phys. Rev. B 1986. **33**.



## **Chapter 3: Extension of microwave and nitronium ion chemistry to directly disperse highly conductive carbon nanotubes**

### **3.1: INTRODUCTION**

Carbon nanotubes have always been an highly attractive material and the focus of considerable research since their discovery in 1991 by Iijima[1] due to their excellent mechanical, electromagnetic and chemical performance. Their applications cover a wide range such as nanoelectronics, hydrogen storage, nanobiosensors, tissue engineering, etc. and have been well-documented.[2-4] Recently, the increased demand in liquid crystal displays, solar cells, and touch panels requires high performance, transparent, and conductive films. However these thin films are mainly prepared by using semiconductor oxides, such as indium tin oxide (ITO) and fluorine-doped tin oxide (FTO) because of their good conductivity and transparency. However, these materials suffer from inflexibility and limited availability of the rare metal. Carbon nanotubes are expected to solve these problems because of their reported excellent conductivity, flexibility and easy synthesis.[5] To satisfy the rapidly increasing demand for the material, high concentrations of carbon nanotube dispersions are largely desired. Great effort has been devoted over the past few years to prepare stable dispersions of carbon nanotubes with the aid of DNA,[6] small aromatic molecules,[7-11] water solution polymers[12, 13], and surfactants[14-16]. In aqueous media, surfactants,

such as sodium dodecyl sulphate[17] and the superior sodium dodecylbenzene sulphonate (SDBS)[18] have always been the most commonly used dispersant for carbon nanotubes, due to its low cost and its efficiency in dispersing carbon nanotube.

It is generally believed that the surfactants could be completely removed after thin films are formed, because of their high solubility in aqueous media.[5, 19] However, recent reports have shown that the surfactants indeed remained in the carbon nanotube samples even after extensive washing,[20, 21] which dramatically decreased the quality of the films, because the surfactants increased the contact resistance between nanotubes by covering their intrinsic properties. Thus, surfactants are undesirable for high-performance applications. *N*-Methyl-2-pyrrolidone (NMP) dispersions of carbon nanotube gives dispersion of carbon nanotube without any modification on surface, thus high quality of carbon nanotubes were obtained. This method, however suffers from the toxicity of the solvent and low conductivity of the films. Just like surfactants, complete removal this solvent from CNT films is difficult due to its high boiling point. All these factors would hinder its application in industry.

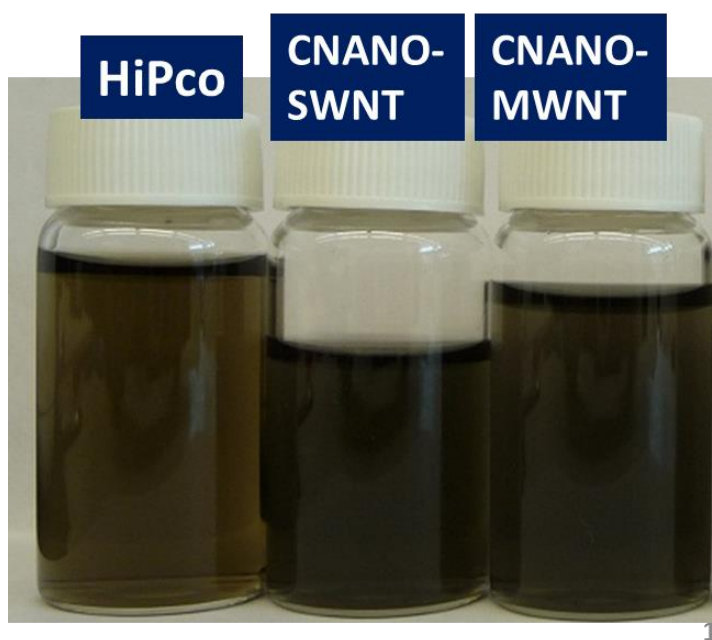
Microwave irradiation has been reported to be an excellent tool in dispersing high concentrations of carbon nanotube.[22] Wang et al. reported that individually suspended carbon nanotubes can be obtained by microwave irradiation. However, the resulting carbon nanotubes were highly oxidized, and were insulating. In this chapter, we extend the knowledge obtained from graphene

fabrication and directly apply the methods to carbon nanotube and directly and easily produce highly conductive carbon nanotubes. We also show that this method strongly depends on the quality of the starting materials.

### 3.2: RESULTS AND DISCUSSION:

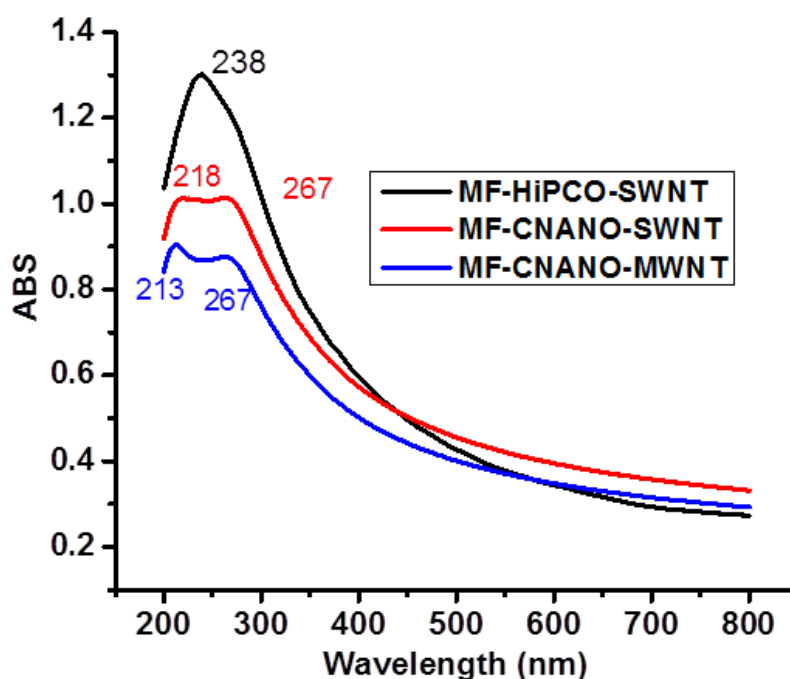
#### 3.2.1: Optical characterizations (Coloration and UV-Vis)

First of all, it had to be verified whether exfoliations using our method based on nitronium ions and microwave irradiation are effective when applied to



**Figure 3.1:** Photographs of microwave-enabled dispersions of different types of carbon nanotubes. a) HiPco single-walled carbon nanotubes, b) CNANO-single-walled carbon nanotubes, and c) CNANO multi-walled carbon nanotubes.

carbon nanotubes. Three carbon nanotube samples were tested, i.e. single-walled carbon nanotube (SWNT) produced by high-pressure carbon monoxide disproportionation (HiPco-SWNT), SWNT provided by Cnano, Inc. (CNANO-SWNT) and Multi-walled carbon nanotube (MWNT) provided by Cnano, Inc. (CNANO-MWNT). The very first observation was made visually. The darkness and the coloration of dispersions can reveal much regarding concentration, oxidation states, and surface chemistry of carbon based



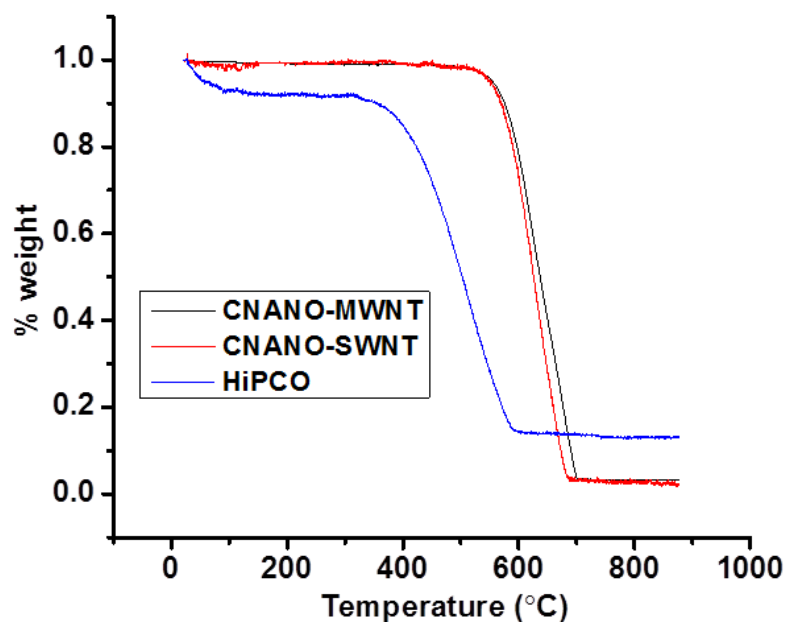
**Figure 3.2:** UV-Vis spectra of aqueous dispersions of different types of HiPco single-walled carbon nanotubes (black), CNANO-single-walled carbon nanotubes (red), and CNANO multi-walled carbon nanotubes (blue).

materials. Figure 3.1 is a photograph showing the resulting suspensions (diluted 10-fold in water) after microwave reactions with HiPco (left), CNANO-SWNT (middle) and CNANO-MWNT (right). These dispersions were stable against sedimentation for months, indicating that carbon nanotubes were exfoliated and dispersed in the aqueous medium. The apparent colors of both CNANO-SWNT and CNANO-MWNT are grey, while the final product of the HiPco-SWNT after the microwave irradiation had an orange-brown color. Despite the fact that the three types of unreacted carbon nanotubes used appear to be black, the different colors of the dispersion products in water following microwave reactions indicated that the carbon nanotubes exist in different oxidation states. It is well-known that the coloration of CNT dispersions monitors the electronic structure of the dispersed carbon nanotubes, very similar to dispersed graphene described in the previous chapter. So it is obvious that the HiPco-SWNT is more oxidized than both CNANO-SWNT and CNANO-MWNT. When conjugated carbon based materials lose conjugation due to oxidation, they undergo hypsochromic blue shifts. We then used UV-vis spectroscopy to examine their electronic structures. Figure 3.2 shows the absorption spectra for these carbon nanotube dispersions in water. For all three types of CNTs, the absorbance gradually decrease from UV to near-IR regions, similarly to the absorption spectrum reported by Jiang et al., due to scattering, especially in the lower wavelength range[23]. Distinct differences can be immediately observed. The HiPco-SWNT shows a single absorption peak at 238 nm, while the two CNANO carbon nanotubes show two

peaks at 218 nm and 267 nm, and 213 nm and 267 nm for MF-CNANO-SWNT and MF-CNANO-MWNT, respectively.

### **3.2.2: Thermal stabilities and purities**

Thermogravimetric analysis (TGA) can be extremely useful for analysis and of the quality of the dispersed carbon nanotubes, as well as the thermal stability and the composition of the bulk samples[24]. In a typical TGA weight loss curve, the important parameters are 1) the initiation temperature, 2) the pyrolysis temperature, and 3) the final mass of the residual substances. The initiation temperature is the temperature at which the material starts to decompose. The pyrolysis (in the inert atmosphere) or oxidation (in the oxidative atmosphere) temperatures are the point where the rate of weight loss is at maximum, which in



**Figure 3.3:** TGA mass loss of three different carbon nanotubes: HiPco-SWNT (blue), CNANO-MWNT (black) and CNANO-SWNT (red). When the pyrolysis was completed, HiPco-SWNT had about 18% of catalyst residual mass of remaining,

general is defined as the thermal stability of the material. Finally, the residual mass in the TGA data is usually attributed to the amount of metal catalyst used during the fabrication of the carbon nanotubes, which also includes the oxidized product of the same catalyst.[25-27] It should be noted that in previous experiments, we noticed that the quality of TGA data is dependent on the heating rate. Higher heating rates, such as 10 °C/min, are known to cause undesired carbon nanotube combustion, leading to different shapes of TGA traces and higher error.[28] Thus, all TGA experiments were performed at a heating rate of 5

°C/min. We then used TGA to examine the thermal stability and the purity of the different bulk samples. The TGA data in figure 3.3 indicates that the HiPco-SWNT (blue) had a weight loss right after heat was applied. At around 100 °C, the material had lost about 10 % of its original weight, which corresponds to the loss of water molecules and oxygen-containing groups on the surface of the carbon nanotubes. Then, the HiPco-SWNT was thermally stable from 100 °C up to about 400 °C. At this point, it experienced a dramatic weight loss in the range of 400 °C to 600 °C, indicating its pyrolysis temperature, which can be associated with the pyrolysis of carbon materials. The final weight became constant right above 600 °C with residual mass being about 18 % of its original weight. The 18% of the residual material that thermal stable up to 900 °C was attributed to the amount of oxidized catalyst (in the forms of metal oxides) in the sample, which were used for the synthesis of the carbon nanotubes in the HiPco process, namely the Fe catalyst. On the other hand, both the CNANO-SWNT and CNANO-MWNT were extremely stable up to 600 °C. These two samples exhibited only one exothermal event at 600 °C in which they both underwent a complete carbon pyrolysis, leaving about 2-3 % of the incombustible catalyst materials behind.

The overall thermal stability of HiPco-SWNT is much lower than those of CNANO-SWNT and CNANO-MWNT. There could be some parameters that might have contributed to the differences in the pyrolysis temperatures, however one should realize that higher pyrolysis temperature is always a result of a purer

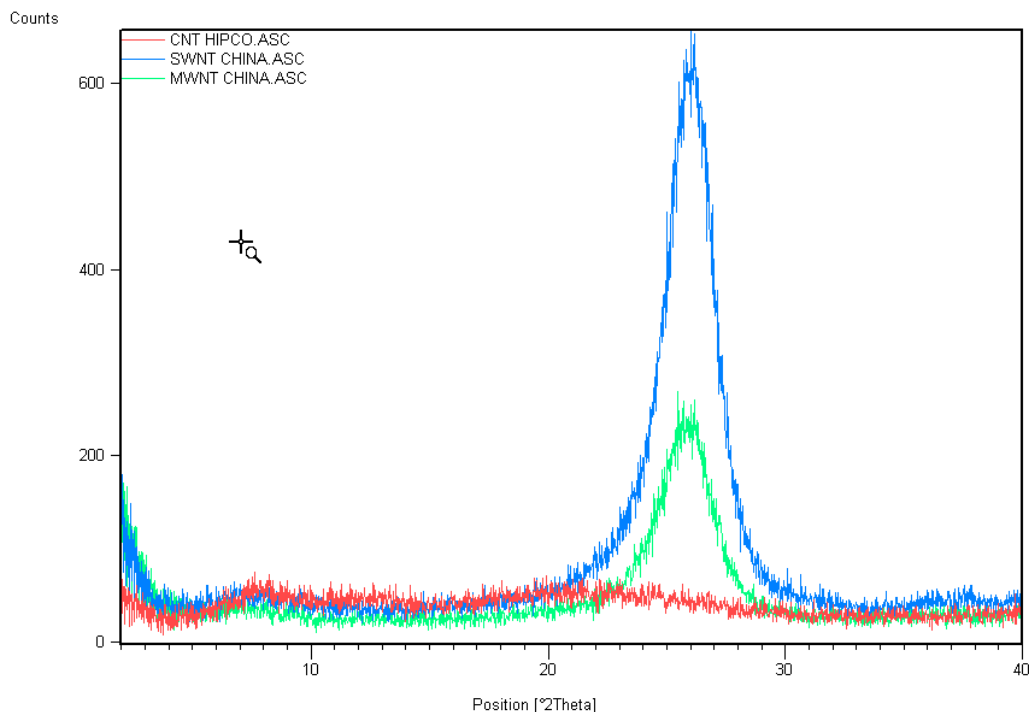


and less defective sample. Highly crystalline carbon nanotubes have been reported to have a higher resistance to oxidation[26]. Defects and derivatization moiety in carbon nanotube always lower the thermal stability. The effect of sizes of carbon nanotubes also plays an important role in the thermal stability[29]. Kim et al. demonstrated that MWNTs with small diameters tended to decompose and oxidize at lower temperature than those larger ones. The lengths of the carbon nanotubes also influence the oxidation temperature. It has been documented that as the lengths of carbon nanotubes decrease, the oxidation reaction occurs at lower temperatures[30]. Some reports have revealed correlations between the carbon nanotubes and the catalyst particles present in the carbon nanotube sample, especially Fe catalyst. As the amount of iron catalyst increased, the oxidation temperature was found to decrease[31]. This could be due to the catalytic effect from the iron catalyst. With an increase amount of catalysts, the reactivity of the CNT also increases, thus resulting in an decreased oxidation temperature[31].

### **3.2.3: XRD for structural information**

The X-ray spectroscopy has been useful as a tool for structural characterization of carbon nanotubes. It can provide important information about the differences we observed in the final carbon nanotube products. The XRD patterns of CNANO-SWNT, CNANO-MWNTs and HiPco-SWNT are shown in

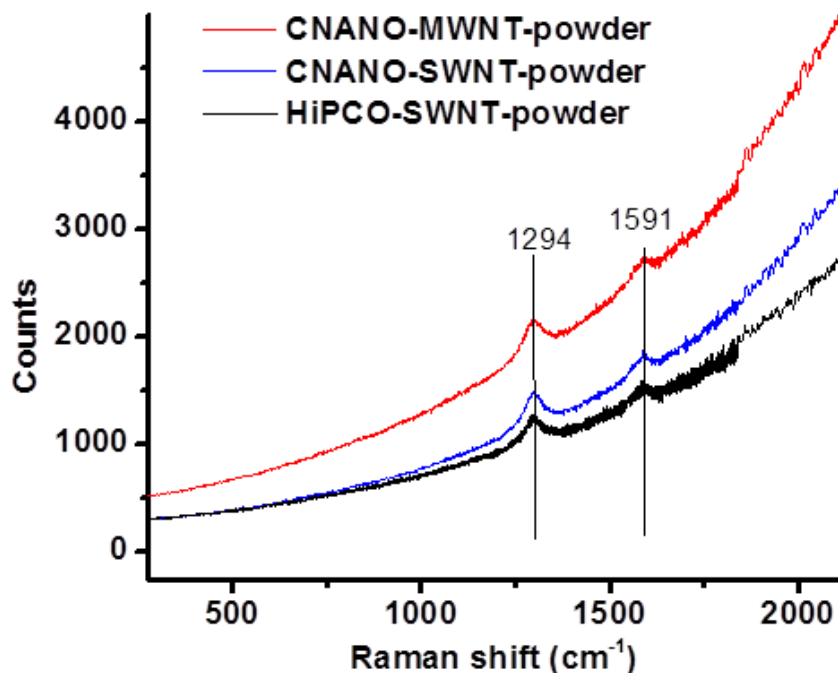
Figure 3.4. The diffraction peaks at  $26.5^\circ$  observed in the diffraction of both CNANO-MWNT and CNANO-SWNT can be attributed to the interlayer spacing



**Figure 3.4:** X-ray spectra of HiPco (red), CNANO-SWNT (blue) and CNANO-MWNT (green).

(0.34 nm) hexagonal graphite structures (002) of the carbon atoms in the nanotubes, in good agreement with literature[32]. For HiPco-SWNT, a rather wide and shallow (002) peak is observed in its XRD pattern, implying that HiPco-SWNT is a rather amorphous carbon material with small regions of crystallinity and MWNTs are in graphite form. The higher crystallinities in both CNANO-SWNT and CNANO-MWNT might provide the reasons behind the lowered

oxidation states compared to HiPco-SWNT, since they are relatively unreactive, and thus less likely to be oxidized by the nitronium ions.

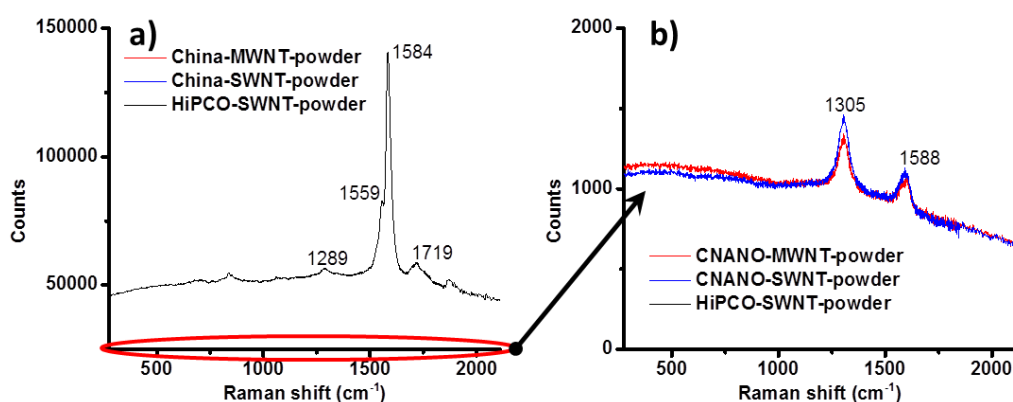


**Figure 3.5:** Raman spectra of non-treated CNANO-MWNT (red), CNANO-SWNT (blue) and HiPco-SWNT (black), in powder form.

### 3.2.4: Raman spectroscopy

Raman spectroscopy provides information about the crystal structure and the presence of disorder or defects in carbon nanotube samples. Raman spectroscopy was performed on each of the starting material types and each corresponding dispersion products. Stacked spectra for the starting materials are

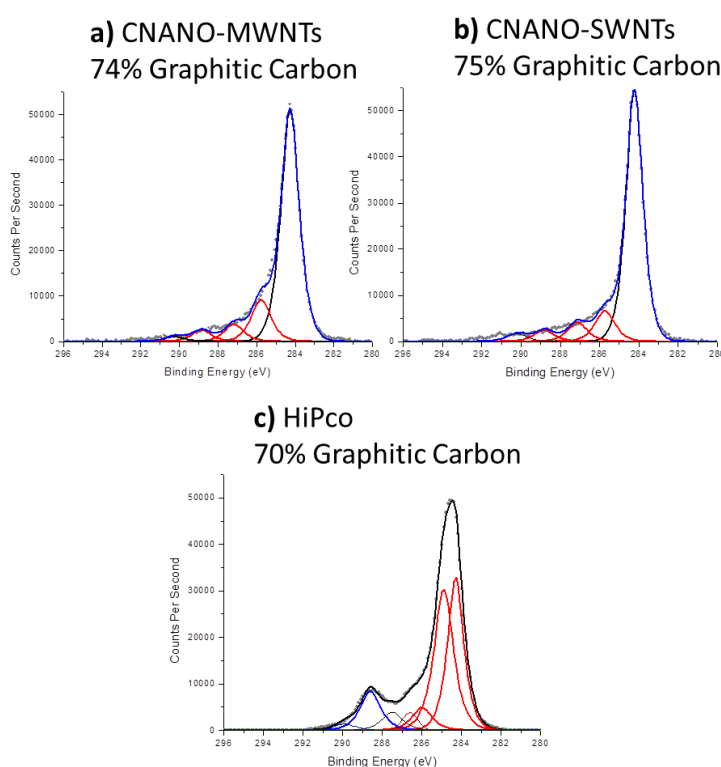
shown in Figure 3.5. Interestingly, both the D bands, which originated from the disordered structures and defects carbon[33] and the G bands, which correspond to the tangential vibrations of the graphitic carbon on the outermost wall, of the different resource of carbon nanotubes appear at  $1291\text{ cm}^{-1}$  and  $1591\text{ cm}^{-1}$ , respectively. After the microwave reactions, the dispersed CNTs were structurally different. Figure 3.6a shows stacked spectra of the final dispersed



**Figure 3.6:** As collected Raman spectra of microwave treated CNANO-MWNT (red), CNANO-SWNT (blue) and HiPco-SWNT (black). All spectra were collected on dried products obtained after the microwave reactions. b) Spectra of CNANO-MWNT (red) and CNANO-SWNT (blue) were zoomed in 70 times, indicating that the signals from these samples were much lower than HiPco-SWNT.

products collected on an alumina filter membrane. The product of HiPco-SWNT showed a distinct spectrum which had much stronger signal counts than both CNANO-SWNT and CNANO-MWNT. The spectra for the other two CNTs needed to be multiplied by 70 times to be visible, see figure 3.6b. The HiPco-

SWNT showed a typical Raman spectrum of SWNTs. The most prominent Raman active modes of SWNTs, include the RMB band ( $189 - 312 \text{ cm}^{-1}$ ), the sharp D-band ( $1289 \text{ cm}^{-1}$ ), sharp G-band ( $1584 \text{ cm}^{-1}$ ) and the sharp G'-band ( $2554 \text{ cm}^{-1}$ ). However, both CNANO-SWNT and CNANO-MWNT showed similar Raman spectra with only a broader D band at  $1305 \text{ cm}^{-1}$  and G bands at  $1588 \text{ cm}^{-1}$ . It is not clear yet at this stage why extremely low intensities were observed in their Ramam spectra, further work is needed.



**Figure 3.7:** Carbon 1s core XPS spectra for thin films of microwave treated dispersions of (a) CNANO-MWNT b) CNANO-SWNT and c) HiPco-SWNT. The content of oxygen-free carbon of CNANO-MWNT and CNANO-SWNT were comparable at 74% and 75%, respectively; while the content in HiPco-SWNT decreased to 70%.

### **3.2.5: XPS for surface functionalization**

X-ray photoelectron spectroscopy was used to study the oxidation stages of the dispersed CNTs after microwave irradiations. The surface of the samples was bombarded with X-ray photons, causing an ejection of core electrons from the samples. The XPS analysis of the produced spectra gives the binding energies in electron volts (eV). Using the magnitude of the binding energies differences between atomic elements and the nature of bonding in molecules, we can identify the element with different chemical bonds. Figure 3.7 shows XPS survey spectra of the final products. Both CNANO-SWNT (figure 3.7a) and CNANO-MWNT (figure 3.7b) showed similar amounts, 75% and 74%, of graphitic carbon, respectively. HiPco-SWNT showed a slight decrease (only 70%) in the amount of graphitic carbon (figure 3.7c). These results indicate that HiPco-SWNT is more prone to oxidation, compared to both CNANO-SWNT and CNANO-MWNT. This is in agreement with the TGA data discussed above. HiPco-SWNT contained more iron catalyst particles than the other two CNTs, and the catalyst particles have been shown to have catalytic effect on nanotube oxidation[34]. Xu et al. have demonstrated that by deactivating the iron particles in SWNT samples, the oxidation reactions were intensely quenched.

### **3.3: CONCLUSION:**

Our study shows that the nitronium ion microwave oxidation chemistry can be extended to be used other carbon-based materials, such as carbon nanotubes to directly obtain highly conductive CNT without requirement of postreduction process. A combined analysis of UV-Vis, TGA, XRD, Raman, and XPS measurements on the dispersion of different sources of carbon nanotube using nitronium ions and microwave chemistry is presented. We used three different types of carbon nanotube to demonstrate that this method can be used to synthesize different quality of materials by simply choosing different starting materials. We also demonstrated that this method can result in stable carbon nanotube dispersion with high concentrations in aqueous media without any surfactant. This method opens a new pathway for synthesis of high-quality carbon nanotube materials for many astonishing applications.

### **3.4: MATERIALS AND METHODS:**

#### **3.4.1: Materials:**

CNTs were obtained from different sources. HiPco SWNTs were obtained from Carbon Nanotechnologies (Austin, TX), while CNANO-SWNTs and CNANO-MWNTs were kindly supplied by CNano Technology Limited (Santa Clara, California, USA and Beijing, China). Graphite powder was purchased from Sigma-Aldrich. Sulfuric acid (98%) and nitric acid (70%) were purchased from Pharmco and were used as-received. All solutions were prepared using deionized water (18.2 M $\Omega$ ) (Nanopure water, Barnstead).

### **3.4.2: Methods:**

#### **3.4.2.1: Synthesis of carbon nanotube**

Three types of CNTs (HiPco SWNT, CNANO-MWNT, and CNANO-SWNT) were functionalized and suspended in DI-water similar to the procedures as described in Chapter 2. In short, 10 mg (unless mentioned otherwise) of CNT was mixed into a mixture of sulfuric acid and nitric acid at 1:1 ratio. This final mixture was then placed into a CEM Discover microwave reactor and irradiated for 30 seconds at a fixed power of 300 Watts. After microwave irradiation, the products were filtered and extensively washed with DI-water. Finally, the collected purified product was re-suspended into water using bath sonication for 30 minutes.

#### **3.4.2.2: Characterizations:**

UV: UV-vis-NIR absorption spectroscopy was used to characterize the electronic states of the carbon nanotube dispersion. All spectra were obtained using a Cary 500 Ultraviolet-visible-near-infrared spectrophotometer. All solutions used in UV-Vis experiments were diluted 10 times from the stock solution.

TGA: We obtained TGA traces of the three carbon nanotubes using ~5 mg each on a Perkin Elmer Thermogravimetric Analyzer Pyris 1 TGA under a



nitrogen flow (20 ml/min) with a heating rate of 5 °C/min. The samples in the TGA furnace were heated from room temperature to 1000 °C.

Raman: Raman spectra from films deposited on alumina membranes using Buchner filtration were collected in a Kaiser Optical Systems Raman Microprobe with a 785 nm solid state diode laser. Spectra were acquired using a 30 s exposure time. Multiple positions were examined to confirm reproducibility.

The x-ray powder patterns were collected using a Rigaku D/max 2200 diffractometer with Cu K $\alpha$  radiation generated at 44 kV and 40 mA. The instrument was configured in the Bragg-Brentano geometry and equipped with an auto-sampler, a diffracted beam monochromator, theta-compensating slits and a scintillation counter. The samples were packed on a silicon low background holder and the samples were rotated at 40 rpm. The data were collected over an angular range of 2 to 40° 2 $\theta$  with a step size of 0.02° 2 $\theta$  and a scan rate of 0.5 °C/min

### 3.5: REFERENCES:

1. Iijima, S., *Helical microtubules of graphitic carbon*. Nature, 1991. **354**(6348): p. 56-58.
2. Paradise, M. and Goswami, T., *Carbon nanotubes – Production and industrial applications*. Materials Design, 2007. **28**(5): p. 1477-1489.
3. Avouris, P. and Chen, J., *Nanotube electronics and optoelectronics*. Materials Today, 2006. **9**(10): p. 46-54.
4. Harrison, B.S. and Atala, A., *Carbon nanotube applications for tissue engineering*. Biomaterials, 2007. **28**(2): p. 344-353.
5. Wu, Z., Chen, Z., Du, X., Logan, J.M., Sippel, J., Nikolou, M., Kamaras, K., Reynolds, J.R., Tanner, D.B., Hebard, A.F., and Rinzler, A.G., *Transparent, conductive carbon nanotube films*. Science, 2004. **305**(5688): p. 1273-6.
6. Zheng, M., Jagota, A., Semke, E.D., Diner, B.A., McLean, R.S., Lustig, S.R., Richardson, R.E., and Tassi, N.G., *DNA-assisted dispersion and separation of carbon nanotubes*. Nat Mater, 2003. **2**(5): p. 338-42.
7. Chen, R.J., Zhang, Y., Wang, D., and Dai, H., *Noncovalent sidewall functionalization of single-walled carbon nanotubes for protein immobilization*. J Am Chem Soc, 2001. **123**(16): p. 3838-9.
8. Xin, H. and Woolley, A.T., *DNA-templated nanotube localization*. J Am Chem Soc, 2003. **125**(29): p. 8710-1.
9. Liu, L., Wang, T., Li, J., Guo, Z.-X., Dai, L., Zhang, D., and Zhu, D., *Self-assembly of gold nanoparticles to carbon nanotubes using a thiol-terminated pyrene as interlinker*. Chemical Physics Letters, 2003. **367**(5-6): p. 747-752.
10. Fernando, K.A., Lin, Y., Wang, W., Kumar, S., Zhou, B., Xie, S.Y., Cureton, L.T., and Sun, Y.P., *Diminished band-gap transitions of single-walled carbon nanotubes in complexation with aromatic molecules*. J Am Chem Soc, 2004. **126**(33): p. 10234-5.
11. Zhang, J., Lee, J.K., Wu, Y., and Murray, R.W., *Photoluminescence and Electronic Interaction of Anthracene Derivatives Adsorbed on Sidewalls of Single-Walled Carbon Nanotubes*. Nano Lett, 2003. **3**(3): p. 403-407.

12. O'Connell, M.J., Boul, P., Ericson, L.M., Huffman, C., Wang, Y., Haroz, E., Kuper, C., Tour, J., Ausman, K.D., and Smalley, R.E., *Reversible water-solubilization of single-walled carbon nanotubes by polymer wrapping*. Chemical Physics Letters, 2001. **342**(3–4): p. 265-271.
13. Moore, V.C., Strano, M.S., Haroz, E.H., Hauge, R.H., Smalley, R.E., Schmidt, J., and Talmon, Y., *Individually Suspended Single-Walled Carbon Nanotubes in Various Surfactants*. Nano Lett, 2003. **3**(10): p. 1379-1382.
14. O'Connell, M.J., Bachilo, S.M., Huffman, C.B., Moore, V.C., Strano, M.S., Haroz, E.H., Rialon, K.L., Boul, P.J., Noon, W.H., Kittrell, C., Ma, J., Hauge, R.H., Weisman, R.B., and Smalley, R.E., *Band gap fluorescence from individual single-walled carbon nanotubes*. Science, 2002. **297**(5581): p. 593-6.
15. Islam, M.F., Rojas, E., Bergey, D.M., Johnson, A.T., and Yodh, A.G., *High Weight Fraction Surfactant Solubilization of Single-Wall Carbon Nanotubes in Water*. Nano Lett, 2003. **3**(2): p. 269-273.
16. Wang, J., Sun, J., Gao, L., Wang, Y., Zhang, J., Kajiura, H., Li, Y., and Noda, K., *Removal of the Residual Surfactants in Transparent and Conductive Single-Walled Carbon Nanotube Films*. The Journal of Physical Chemistry C, 2009. **113**(41): p. 17685-17690.
17. Nish, A. and Nicholas, R.J., *Temperature induced restoration of fluorescence from oxidised single-walled carbon nanotubes in aqueous sodium dodecylsulfate solution*. Phys Chem Chem Phys, 2006. **8**(30): p. 3547-51.
18. Matarredona, O., Rhoads, H., Li, Z., Harwell, J.H., Balzano, L., and Resasco, D.E., *Dispersion of Single-Walled Carbon Nanotubes in Aqueous Solutions of the Anionic Surfactant NaDDBS*. The Journal of Physical Chemistry B, 2003. **107**(48): p. 13357-13367.
19. Zhou, Y., Hu, L., and Gruner, G., *A method of printing carbon nanotube thin films*. Applied Physics Letters, 2006. **88**(12): p. 123109-3.
20. Geng, H.Z., Kim, K.K., So, K.P., Lee, Y.S., Chang, Y., and Lee, Y.H., *Effect of acid treatment on carbon nanotube-based flexible transparent conducting films*. J Am Chem Soc, 2007. **129**(25): p. 7758-9.
21. Wang, J., Sun, J., Gao, L., Liu, Y., Wang, Y., Zhang, J., Kajiura, H., Li, Y., and Noda, K., *Improving the conductivity of single-walled carbon*

- nanotubes films by heat treatment*. Journal of Alloys and Compounds, 2009. **485**(1–2): p. 456-461.
22. Wang, Y., Iqbal, Z., and Mitra, S., *Rapidly Functionalized, Water-Dispersed Carbon Nanotubes at High Concentration*. J Am Chem Soc, 2005. **128**(1): p. 95-99.
  23. Jiang, L., Gao, L., and Sun, J., *Production of aqueous colloidal dispersions of carbon nanotubes*. J Colloid Interface Sci, 2003. **260**(1): p. 89-94.
  24. Mansfield, E., Kar, A., and Hooker, S.A., *Applications of TGA in quality control of SWCNTs*. Anal Bioanal Chem, 2010. **396**(3): p. 1071-7.
  25. Scheibe, B., Borowiak-Palen, E., and Kalenczuk, R.J., *Oxidation and reduction of multiwalled carbon nanotubes — preparation and characterization*. Materials Characterization, 2010. **61**(2): p. 185-191.
  26. Pang, L.S.K., Saxby, J.D., and Chatfield, S.P., *Thermogravimetric analysis of carbon nanotubes and nanoparticles*. The Journal of Physical Chemistry, 1993. **97**(27): p. 6941-6942.
  27. Lima, A., Musumeci, A., Liu, H.-W., Waclawik, E., and Silva, G., *Purity evaluation and influence of carbon nanotube on carbon nanotube/graphite thermal stability*. Journal of Thermal Analysis and Calorimetry, 2009. **97**(1): p. 257-263.
  28. Ajayan, P.M., Terrones, M., de la Guardia, A., Huc, V., Grobert, N., Wei, B.Q., Lezec, H., Ramanath, G., and Ebbesen, T.W., *Nanotubes in a Flash--Ignition and Reconstruction*. Science, 2002. **296**(5568): p. 705.
  29. Kim, D.Y., Yang, C.-M., Park, Y.S., Kim, K.K., Jeong, S.Y., Han, J.H., and Lee, Y.H., *Characterization of thin multi-walled carbon nanotubes synthesized by catalytic chemical vapor deposition*. Chemical Physics Letters, 2005. **413**(1–3): p. 135-141.
  30. Kim, D.-Y., Yun, Y.S., Kwon, S.-M., and Jin, H.-J., *Preparation of Aspect Ratio-Controlled Carbon Nanotubes*. Molecular Crystals and Liquid Crystals, 2009. **510**(1): p. 79/[1213]-86/[1220].
  31. McKee, G.S.B., Deck, C.P., and Vecchio, K.S., *Dimensional control of multi-walled carbon nanotubes in floating-catalyst CVD synthesis*. Carbon, 2009. **47**(8): p. 2085-2094.

32. Endo, M., Takeuchi, K., Hiraoka, T., Furuta, T., Kasai, T., Sun, X., Kiang, C.H., and Dresselhaus, M.S., *Stacking nature of graphene layers in carbon nanotubes and nanofibres*. Journal of Physics and Chemistry of Solids, 1997. **58**(11): p. 1707-1712.
33. Saito, R., Jorio, A., Souza Filho, A.G., Dresselhaus, G., Dresselhaus, M.S., and Pimenta, M.A., *Probing Phonon Dispersion Relations of Graphite by Double Resonance Raman Scattering*. Physical Review Letters, 2001. **88**(2): p. 027401.
34. Xu, Y.Q., Peng, H., Hauge, R.H., and Smalley, R.E., *Controlled multistep purification of single-walled carbon nanotubes*. Nano Lett, 2005. **5**(1): p. 163-8.

## **Chapter 4: Self-assembled thin films of graphene and graphene/CNT composites for electronics applications**

### **4.1. INTRODUCTION:**

Most optoelectronic devices, such as touch screens, organic light emitting diodes, and flat panel displays require transparent conducting electrode materials. Indium tin oxide (ITO) is the most commonly used transparent conducting thin films, but it suffers from many of the following disadvantages: 1) the cost of the materials has been drastically increasing, 2) it is incompatible with plastic substrates because of its high processing temperatures, and 3) it cannot be used in applications of flexible devices, because of its brittle nature. Thus, cheap and flexible transparent conducting thin films are being pursued intensively. As mentioned in earlier chapters, due to its wonderful properties, such as remarkable stiffness, high surface area, high thermal and electrical conductivity and high optical transmittance, it has been proposed and experimentally demonstrated that graphene is an excellent candidate to make highly conductive and transparent thin films to replace ITO in wide range optoelectronic applications. To reach this goal, productions of high-quality graphene or graphene-based composite films are required[1-3]. High-quality graphene films can be synthesized by chemical vapor deposition (CVD)[4-8] on different substrates, which have low sheet resistance of  $\sim 500$  ohm/sq at 85% optical

transmittance[8]. Another method for making graphene films is based on exfoliated graphene sheets, which are largely fabricated from reduction of graphene oxide (GO)[9]. The thin film preparation methods using GO-based suspensions include spray-coating[10, 11], spin-coating[12, 13], drop-casting, vacuum filtration[14, 15], and Langmuir-Blodgett (LB) assembly[16, 17]. Thin films prepared by these methods often suffer from multilayer aggregation and crumbling due to the uncontrolled de-wetting and evaporation of solvents and the strong capillary effect[18]. Development of a better and easier way for thin film fabrication is highly desired.

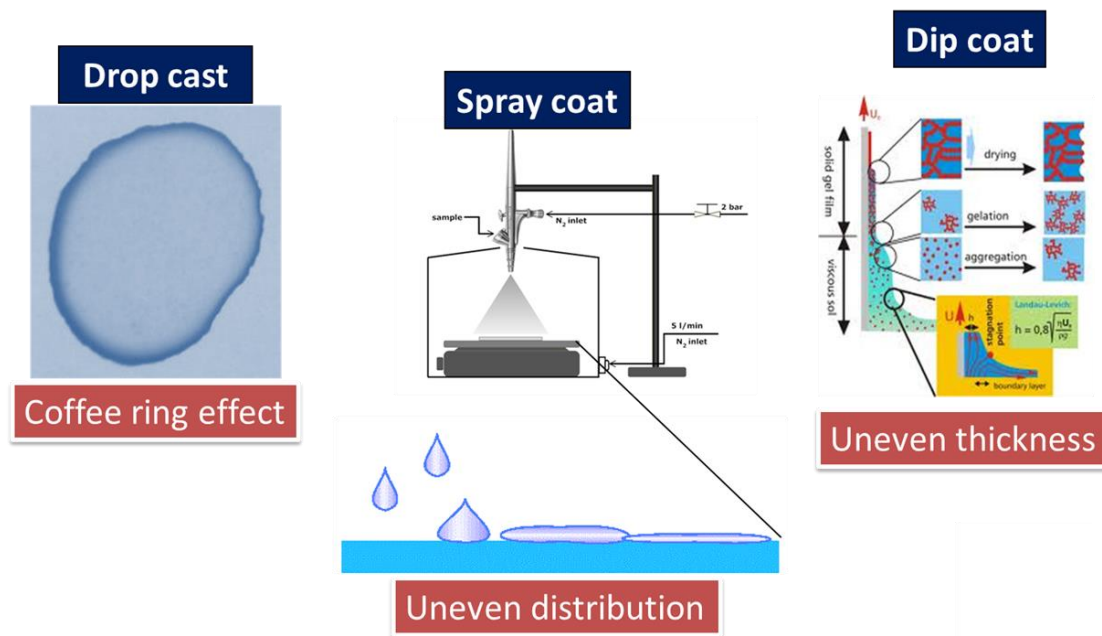
Here, we report an investigation of energetically favorable formation of self-assembled close-packed graphene thin films at the liquid-liquid interface and the potential to use this method to fabricate transparent yet highly conductive graphene thin film for the replacement of ITO.

## **4.2. RESULT AND DISCUSSION:**

### **4.2.1. Current issues with film preparations**

There are numerous solution-based processing methods for making thin films. The common ones include drop-casting, spray coating, and dip coating. However, they suffer from different limitations and are summarized in figure 4.1. The phenomenon of coffee ring is often suffered in drop casting method. This drying pattern is formed during the evaporation process of solvents in which the differential evaporation rates across the drops of solvents induce a capillary flow, causing solvent from the interior to continuously feed the evaporating solvent on

the edge of the drop. This can carry all the dissolved material to the edge, causing the coffee ring effect[18].

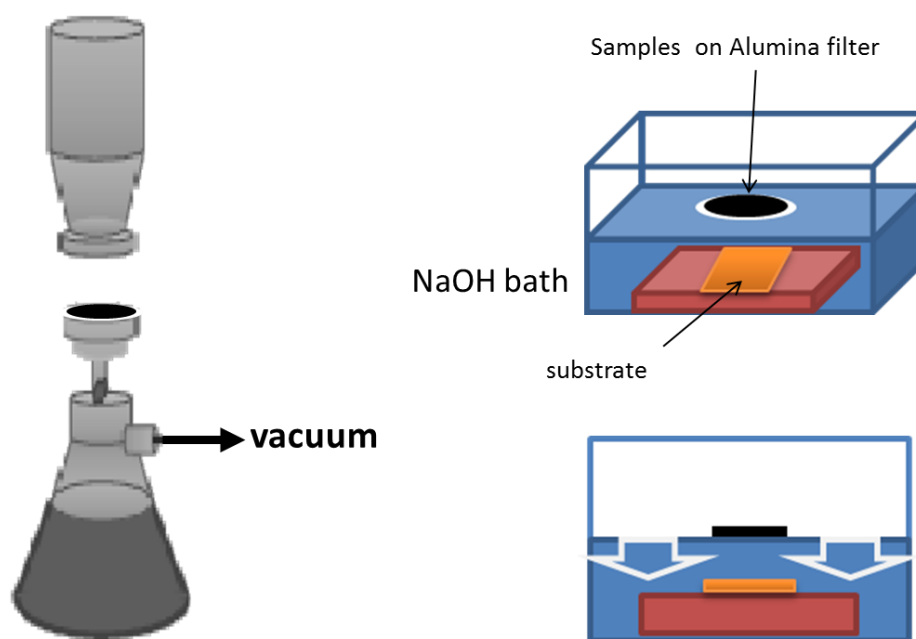


**Figure 4.1:** Three common film deposition methods used to fabricate thin films and their major drawbacks.

Another promising method to make thin films is the vacuum filtration method, which has been used to fabricate highly conductive carbon nanotube thin films[19]. To produce uniform films, dilute suspensions are poured over uniformly porous filtration membranes. This method is more favorable because it is self-regulatory. As the solvent goes through the pores, the suspended carbon nanotubes are trapped on the surface of the filter, forming an interconnecting network. The homogeneity of the films prepared by this method comes from the



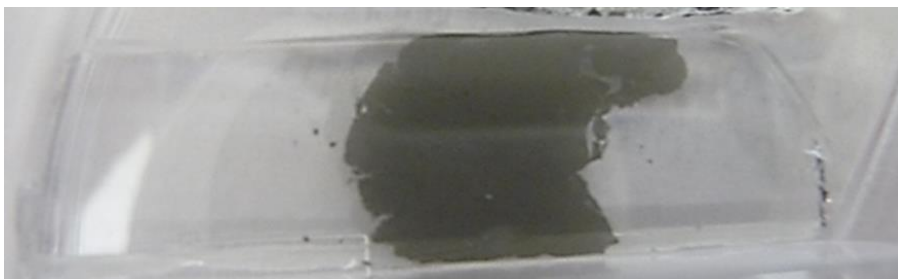
fact that the regions with more densely packed nanotubes can act as a regulator to slow the fluid flow through the filter, allowing other regions to accumulate tubes which would result in films with high degree of uniformity if all parameters, including filtration rate and filtration volumes, are optimized. Recently this method has been used to fabricate GO films[20].



**Scheme 4.1:** Schematic of the procedures involved in transferring a graphene film collected via vacuum filtration on an alumina membrane unit to a submerged substrate.

We also applied this method to make graphene films from the ME-LOGr solutions and then transferred the obtained thin films onto glass substrates. Scheme 4.1 shows the processing procedures [21]. In brief, graphene films with controlled thickness were fabricated with vacuum filtration through an alumina

membrane. The obtained thin film with the alumina membrane was placed in a NaOH bath (4M). In the same time, a substrate, onto which the graphene film would be transferred, was also placed in the bottom of the NaOH solution container. After the alumina filter is etched away, the thin film becomes float on the surface NaOH solution. NaOH is then removed by exchanging with DI water until the solution pH becomes neutral, and finally the water is slowly removed. As all water is removed, the floating film is slowly descended and attached to the pre-positioned substrate sitting at the bottom right on top of the substrate, which is preplaced on the bottom of the NaOH solution container.

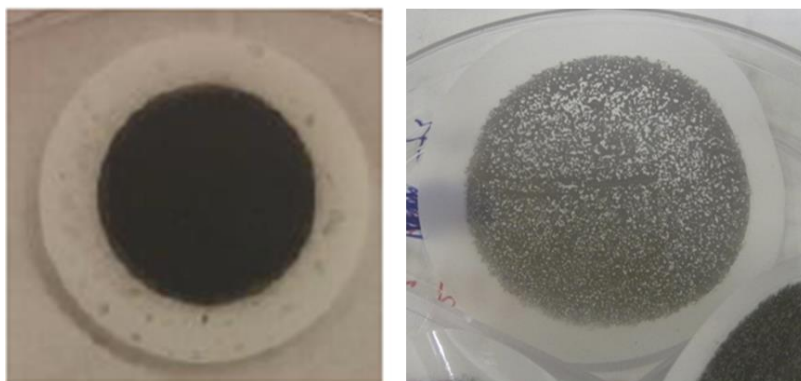


**Figure 4.2:** photograph of a successful transfer of a graphene film on to a quartz substrate.

Figure 4.2 is a digital photograph of a successful transfer of a graphene film on to a quartz substrate. The film is highly uniform and continuous. However, this method requires the removal of the filter membrane, which is generally performed in a NaOH bath. This would become a major source of contamination. In addition, purifying the base solution is a time-consuming procedure, which

consumes a large amount of water. Another immediate issue with this method is the size limitation. The size of the film is limited to the size and quality of the filter membrane.

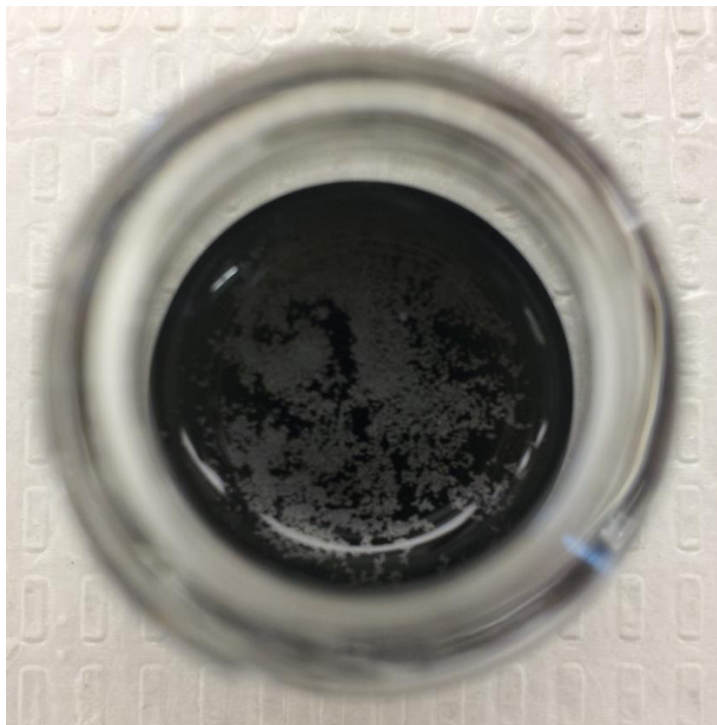
Figure 4.3 shows two attempts in fabricating graphene films on the filter membranes. It clearly shows that the film formed on the left is much more uniform than the one on the right. This problem is not fully understood yet, but we have hypothesized that this is mainly due to the different wettability of the filter membrane to the graphene suspensions. When parts of the filter membrane are not sufficiently wetted by the graphene suspension, it would result in droplets of the suspension not sticking to the membrane, rolling off to other parts that are more wettable, forming localized and more densely packed regions.



**Figure 4.3:** Digital photographs of two different attempts in fabricating graphene films on the filter membranes. It is obvious that the reproducibility of this filtration method is not perfect.

#### 4.2.2: Surface active nature of ME-LOGr graphene sheets

As discussed previously[22] (also in chapter 2), the as-synthesized ME-LOGr sheets have a majority of the graphitic surface intact. However they are slightly oxidized bearing small amount of oxygen-containing groups across the entire graphene sheet. In theory, these graphene sheets can essentially be viewed as amphiphilic materials with a large amount of hydrophobic domains surrounded with hydrophilic regions on the basal plane and edges. Amphiphilic

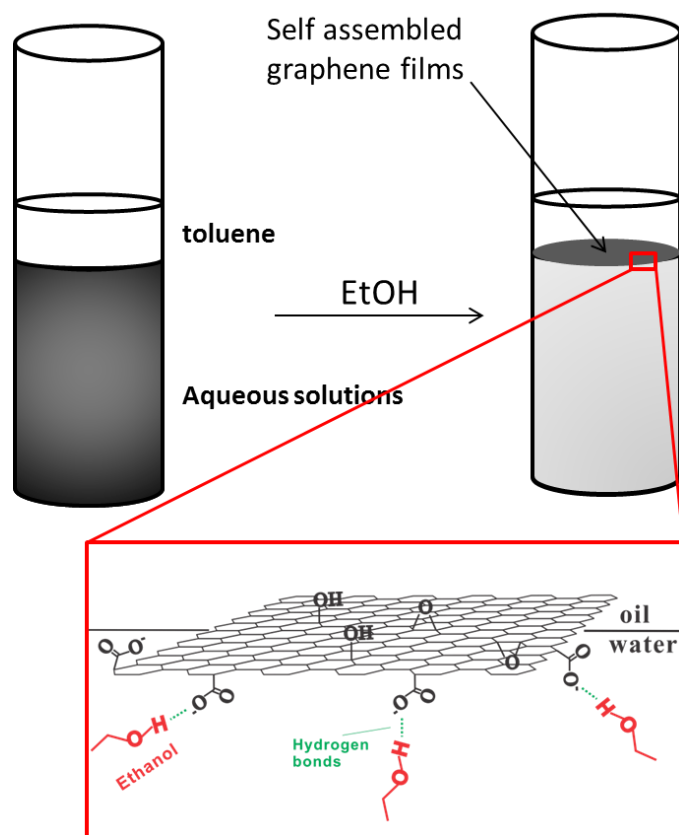


**Figure 4.4:** A Top-view digital photograph of a ME-LOGr aqueous suspension. Some surface –active graphene sheets can be clearly seen at the air-water interface.

materials are known to be surface active and are able to adhere at liquid/liquid or air/liquid interfaces[23]. If ME-LOGr graphene sheets are true amphiphiles, they should also be surface active. It was indeed what we observed. Figure 4.4 shows an as synthesized ME-LOGr suspension, and small amounts of graphene can be seen to adhere at the water/air interface, confirming the surface activity of ME-LOGr graphene sheets. It is important to note that the adhesion at the interface is a self-directed reaction, no external agitation or forces are needed.

#### **4.2.3: Self-assembly of graphene thin film at a liquid/liquid interface with ethanol as an inducer**

Inspired by the surface activity and the amphiphilic nature of the graphene sheet, self-assembly of graphene thin films at a liquid/liquid interface are studied. A liquid/liquid interface having a thickness on the order of a few nanometers to “zero” thickness has been shown to be more favorable for synthesizing thin films



**Scheme 4.2:** Illustration of the steps involved in the interfacial self-assembly using ethanol as an inducer. Ethanol reduces the charge density of graphene, promoting self-assembly at the toluene/water interface, by forming hydrogen bonds with  $\text{-COO}^-$  and  $\text{-OH}$  groups on the graphene surface.

than an air/liquid interface, because it retains special thermodynamic properties, such as viscosity and differential densities[24]. To facilitate film formation at the interface, ethanol was added as an inducer (Scheme 4.2) Figure 4.5 shows digital photographs of a graphene suspension in an aqueous phase with a toluene phase layered on top (left) before and (right) after the additions of various amounts of ethanol. It is important to mention that no continuous graphene films

can be formed at the interface without the addition of ethanol. This result suggests that the thin film self-assembly without addition of ethanol is similar to the reported results using chloroform/water interface for GO films[17].



**Figure 4.5:** Digital photographs of: (left) ME-LOGr suspension with toluene added and the same system with (from top to bottom) 1 mL, 2 mL and 5 mL of additional ethanol.

Ethanol has been reported to be able to decrease in the total interfacial energy and therefore encourages the self-assembly[25]. Vanmaekelbergh *et al.* observed a stunning phenomenon that gold nanoparticles can spontaneously self-assemble to form a uniform monolayer film at the liquid/liquid interface by adding ethanol as the inducer and that the film was extremely stable from collapsing into multilayers. According to Pieranski's thermodynamics model, the self-assembly at the liquid/liquid interface can be regarded as the reduction in the

total interfacial energy of the system[26]. Combining with the Young's equation, the total interfacial energy change can be expressed by the following equation[27]

$$\Delta E = -\pi R^2 \gamma_{OW} (1 - \cos\theta)^2 < 0$$

where  $R$  is the radius of the particles,  $\gamma_{OW}$  is the interfacial energy,  $\theta$  is the contact angle. The contact angle is based on various interfaces and can be expressed as follows:

$$\cos\theta = A(\gamma_{PO} - \gamma_{PW})/\gamma_{OW}$$

where  $A$  is the surface area of the materials being absorbed at the interface,  $\gamma_{PW}$  and  $\gamma_{PO}$  are the interfacial energies between oil phase and water phase, the particle and water and the particle and oil, respectively. From the equations above, it can be interpreted that the total energy change,  $\Delta E$ , becomes negative with the self-assembly at the interface. Thus, the self-assembly of surface-active species, such as nanoparticles, is energetically spontaneous and highly favorable when given mechanical work input.

There have been three main proposed mechanisms for the enhancement in film formations with ethanol added as an inducer. Firstly, it has been shown that when ethanol is mixed with water phase, the mixture would generate vigorous upward flows, similar to the roles that gas bubbles (such as CO<sub>2</sub> and nitrogen) in bringing GO sheets into the other oil/water interfaces[17, 28]. The small flowing gas bubbles also create new interfaces for graphene sheets to be

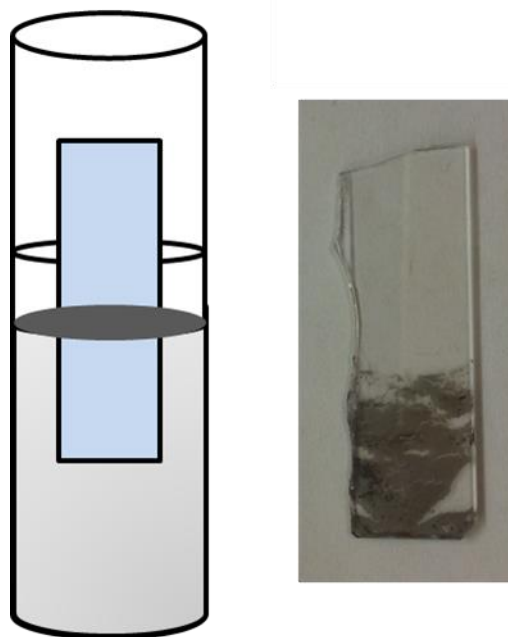


adsorbed. The second theory is that the fact that ethanol is a poor solvent for graphene-based materials[29]. When ethanol is added into a well-suspended system in water, it causes the suspended graphene to become less stabilized in the aqueous phase, promoting the adsorption at the interface to minimize the total energy change. The third proposed factor is related to the change in the charge density of graphene after the addition of ethanol. When ethanol is added into the system, the negatively charged carboxyl groups on the graphene form hydrogen bonds with the hydroxyl groups of the ethanol. These newly formed H-bonds caused a dramatic disruption of the hydrogen bonding network that is originally surrounding individual graphene sheet, which highly stabilizes them in aqueous phase by high degrees of solvation.

#### **4.2.4. Development of a simpler but better film transfer method**

For practical device applications, the self-assembled films formed at the liquid-liquid interface are required to be transferred onto different substrates. In the literature, the transfers of such films are performed generally by dip-coating[30], similar to LB film transfers. In short, a substrate is slowly immersed below the interface, and then is slowly pulled out either in the plane of or perpendicular the self-assembled film. Even though, this method is suitable with many kinds of substrates, it is not robust. A major drawback with this method is the integrity of the transferred films. During the transfer, some parts of the film at the interface are attached to the substrate when it is being immersed, while some

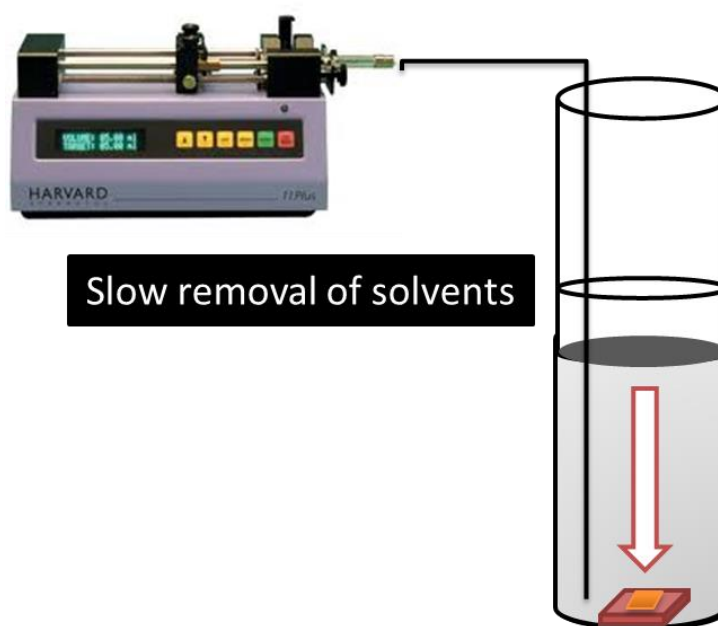
other parts are attached when it is being pulled up, or a combination of both, resulting in incomplete or overlapping transfer.



**Figure 4.6:** a schematic drawing (left) depicting a similar “pull-up” technique similar to that in LB film deposition and a digital photograph (right) of an incomplete film transfer of a self-assembled film onto a glass substrate.

In addition, modifications such as 3-aminopropyl-triethoxysilane (APTES) and ozone treatments, are needed for films to have strong affinities for different substrates. Figure 4.6 shows a schematic drawing (left) depicting a similar “pull-up” technique similar to that in LB film deposition and a digital photograph (right) of an incomplete film transfer of a self-assembled film onto a glass substrate. While there are bands of uniform and continuous film successfully transferred, the overall uniformity of the film is substantially destroyed.

To ensure a complete transfer and to overcome these issues during the transfer, we have developed a new and easy method to meticulously transfer the self-assembled film onto different substrates. Figure 4.7 is an illustration of our method of transfer. In our method, after the formation of a film at the interface, both liquid phases are slowly removed either by pipetting or by a syringe pump. As the liquids are drawn out, the film at the interface is slowly lowered and is



**Figure 4.7:** Illustration of a film deposition on to a submerged substrate utilizing a syringe pump for slow but constant rate of removal the solvents

finally attached to the substrate that is pre-positioned at the bottom of the container. This method results in complete transfer of uniform and continuous films onto any kind of substrates without any need for modifications of substrates. Another major advantage over previously mentioned methods is that our method

is not limited to the size of filter membrane. The size of films fabricated using our method goes to tens of centimeters, and is only limited by the size of the containers of the solvents.

#### **4.2.5. Comparison between films prepared by vacuum filtration and by interfacial self-assembly**

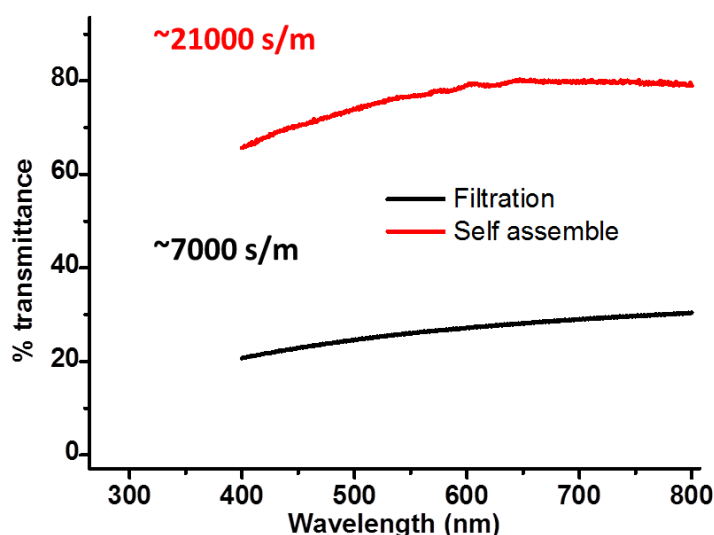
For various potential applications, high quality films, high optical transmittance and low electrical resistivities are highly desired. For instant, the current minimum requirement for transparent conducting oxide materials (mainly ITO) is the simultaneous occurrence of a transmittance of ~90% in the visible region while having an electrical conductivity in the order of  $10^4 - 10^5$  s/cm [31, 32]. To evaluate the films that were prepared using our method for their potential applications, their optical and electrical properties were examined. Figure 4.8 shows the optical properties of both films prepared using vacuum filtration (black) and self-assembly (red), and the measured electrical conductivities are shown next the each corresponding spectrum. It must be noted that the electrical conductivity ( $\sigma$ ) is calculated using

$$R_s = \frac{\rho}{t} = (\pi t / \ln 2) \frac{V}{I}$$

$$\sigma = 1/\rho$$

where  $t$  is the thickness of the films,  $R_s$  is the measured sheet resistance, and  $\rho$  is resistivity. Since thicknesses have been taken into account for the calculations of conductivity, the values can be directly compared to each other. At an incident

light wavelength of 550 nm, films prepared using vacuum filtration and our interfacial method have transmittances of 77% and 26%, respectively. Using these values, the thickness of the films can be estimated using a well-documented value of 2.3% decrease per a layer of graphene. It is surprising that the conductivity of the film prepared using our method is 300% higher than that of the film prepared by vacuum filtration, while the optical transmittance is much higher. It suggests that the quality of the interfacial film was much superior.

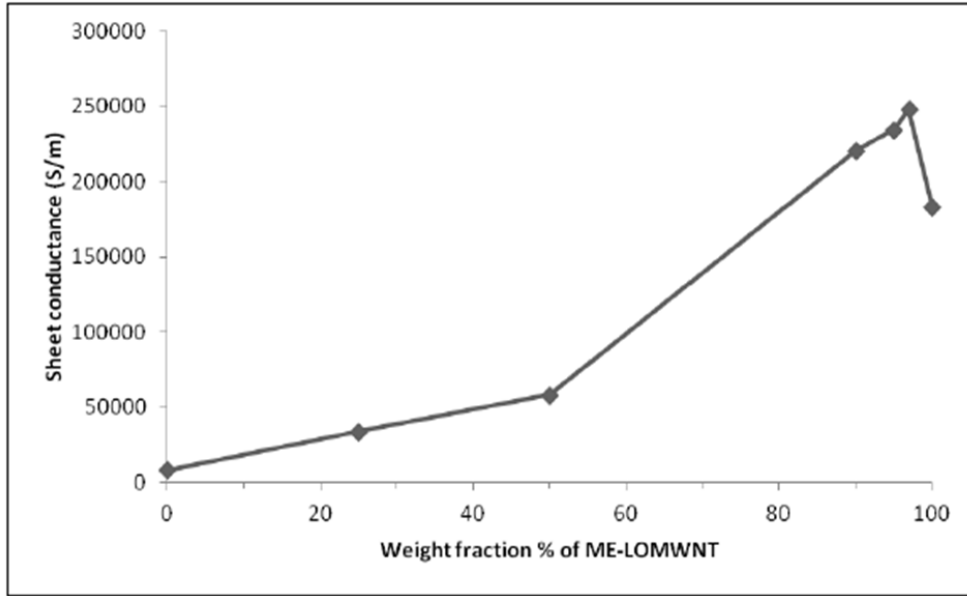


**Figure 4.8:** A plot of % transmittance of films formed by the vacuum filtration method (black) and by self-assembly (red).

#### 4.2.6. Graphene/Carbon nanotube composite films for superior performance

Recently, there have been several reports in the literature about the fabrication of hybrid films of graphene and carbon nanotubes.[33, 34] They showed that the conductivities of the hybrid films were improved compared to

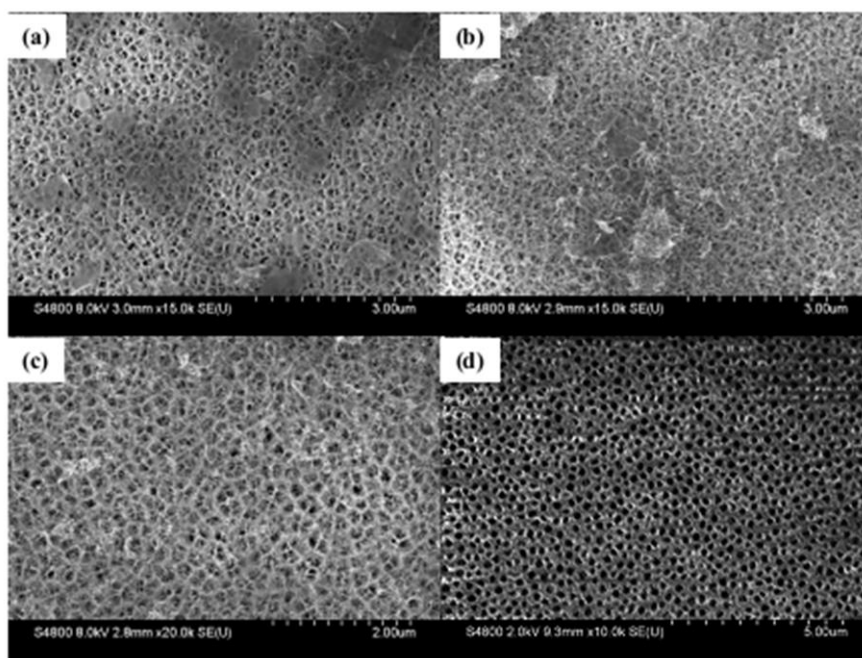
that of films fabricated solely with graphene or carbon nanotubes. It became interesting to study the electronic properties of hybrid films with our interfacial self-assembly method due to the enhanced optical transmittance and the increased electrical conductivity.



**Figure 4.9:** A plot of sheet conductance of the hybrid films as a function of the weight percentage of microwave-dispersed CNANO-MWNT.

Different amounts of graphene and carbon nanotubes were mixed to optimize the ratio for film interfacial fabrications. Figure 4.9 shows a plot of conductivity versus weight fraction percent (0-100 %) of carbon nanotube content. In agreement with some reported trends, the composite film showed a better conductivity than films consisting of only graphene ( $8.2 \times 10^4$  S/m) or only carbon

nanotube ( $1.8 \times 10^6$  S/m) at  $\sim 2.5 \times 10^6$  S/m, which is in agreement with the recent report.

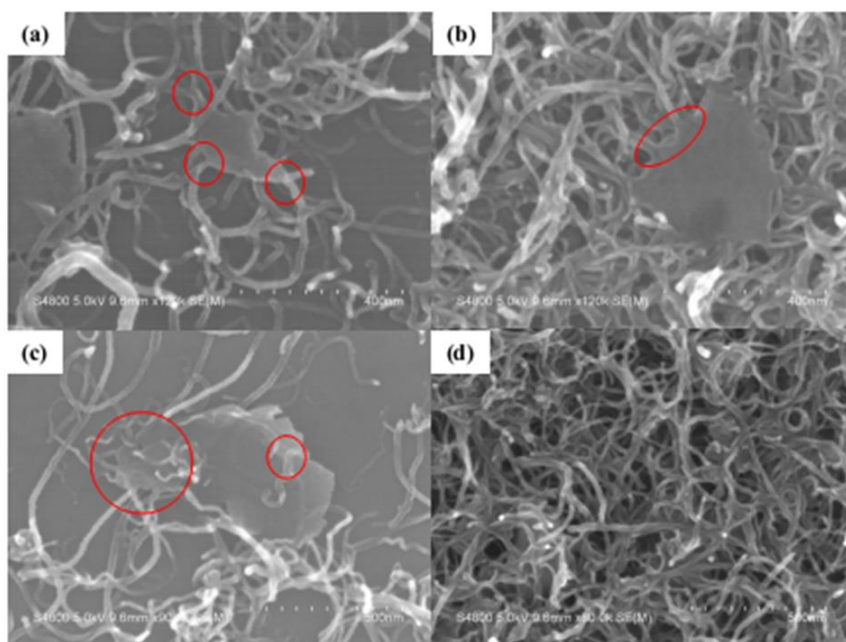


**Figure 4.10:** SEM images of hybrid films deposited on alumina membrane with a weight ratio of (ME-LOMWNTs/ME-LOGr): (a)25/75, (b)50/50, and (c)90/10. (d) A SEM image of a bare alumina membrane.

#### 4.2.7. Direct visual evidence of graphene/carbon nanotube crosslinking

With the ultra-high conductivity obtained, it is interesting to understand how the graphene and carbon nanotubes arranged during film formation. SEM was used to examine the arrangement on the hybrid films obtained via vacuum filtration on an alumina filter membrane. Figure 4.10 are SEM images of the hybrid films with different graphene/carbon nanotube ratios. These images showed that the two materials are highly entangled, connecting with each other

with numerous points, forming a well-established interconnected network. The ratio of graphene and carbon nanotube contents shown in each images roughly corresponds to the weight ratio used for the fabrications of the films.

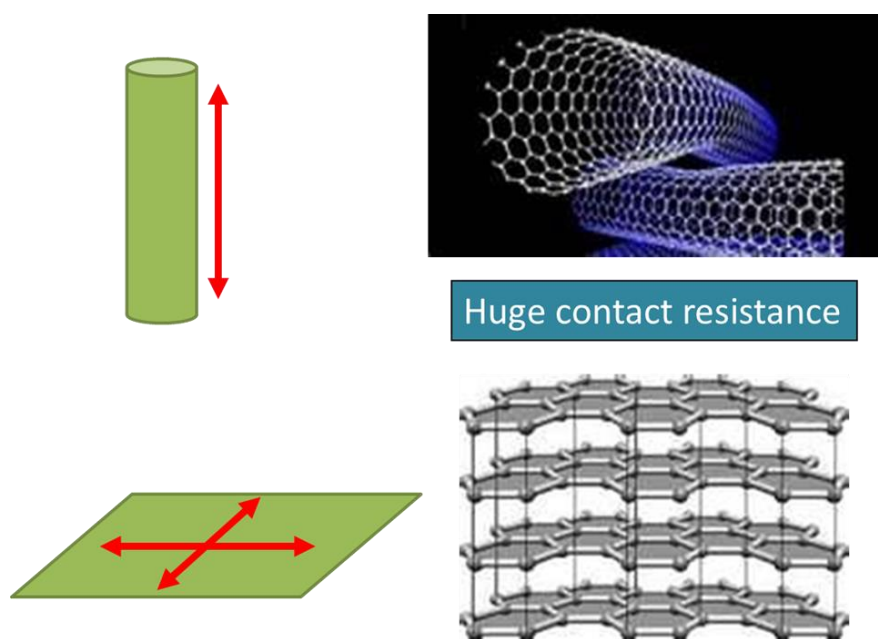


**Figure 4.11:** A series of representative SEM images showing crosslinking (in red circles) in carbon nanotube and graphene hybrid films.

With further investigation, a surprising phenomenon was revealed. Figure 4.11 shows a series of zoomed in SEM images of the hybrid structures. Surprisingly, crosslinked structures were observed at many spots throughout the films, as marked in the images. This finding could be a possible reason behind the enhanced conductivity of the hybrid films. One of the major obstacles in utilizing carbon-based materials in many fields of applications is the contact



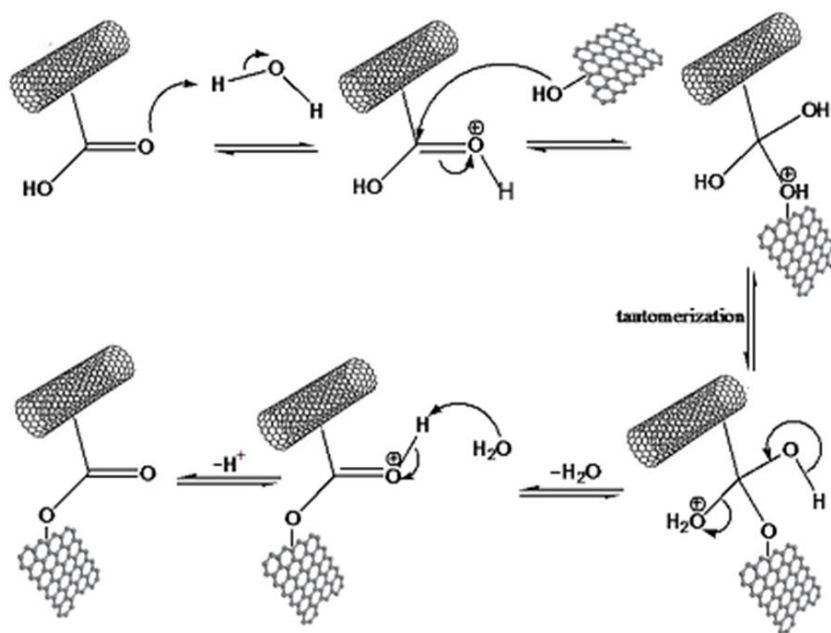
resistance that is present in the junction between two carbon nanotubes or between different layers in a graphene films, see figure 4.12. In the case of carbon nanotube, electrons can be transferred in only one dimension, while electrons are mobile in a 2-D fashion in a sheet of graphene. The crosslinks between carbon nanotubes and graphene sheets greatly improved the electronic contacts at the junctions, therefore the conductivity of the hybrid films.



**Figure 4.12:** (Left) illustrations of the 1D and 2D electron transfer pathways for carbon nanotubes (top) and graphene (bottom). (Right) Huge contact resistances are caused by the gaps between two carbon nanotubes (top) and different layers in graphene (bottom).

Though the exact mechanism of the crosslinking reaction is not fully understood, we propose that the carbon nanotubes and the graphene sheets can be crosslinked via Fischer esterification (See scheme 4.2). It is well-known that

with heat, the carboxylic acid groups on the carbon nanotubes and the hydroxyl or the epoxy groups on the graphene sheets can be readily crosslinked. The sonication process during the preparation of the materials for the synthesis of hybrid films may provide enough heat for esterification reactions. During sonication, the ultrasonic wave creates cavitation bubbles in the solvent, and when these bubbles implode, large amounts of localized heat is generated[35].



**Scheme 4.2:** A possible mechanism of Fisher esterification for the crosslinking in the carbon nanotube and graphene hybrid films.

### **4.3. CONCLUSION:**

In conclusion, a quick and easy fabrication of graphene and carbon nanotube-based thin film using an ethanol-assisted interfacial self-assembly method was developed. This method overcame many challenges faced in other thin film fabrication methods. Qualities of the films made by this method were vastly improved compared to the ones made with the common vacuum filtration method. The optical transmittance and the electrical conductivity of the interfacial self-assembled thin film were 77% @ 550 nm and ~21000 S/m, respectively, while they were 26% and ~7000 S/m by the filtration method.

This method of thin film fabrication can also be extended to prepare graphene/carbon nanotube composite for super conductive materials. By combining the merits of the two, graphene/carbon nanotube composite films showed much higher electrical conductivity than the films made solely by individual component. The results demonstrated that this method has opened opportunities to fabricate ultra-high performance thin films for potential replacement of the transparent conductive materials, such as ITO, which is used in many modern and high-end electronics.

### **4.4. MATERIALS AND METHODS:**

#### **4.4.1. Materials:**

CNTs were obtained from different sources. HiPCO SWNTs were obtained from Carbon Nanotechnologies (Austin, TX), while CNANO-SWNTs and CNANO-MWNTs were kindly supplied by CNano Technology Limited (Santa

Clara, California, USA and Beijing, China). Graphite powder was purchased from Sigma-Aldrich. Sulfuric acid and nitric acid were purchased from Pharco and were used as-received. All solutions were prepared using deionized water (18.2 M $\Omega$ ) (Nanopure water, Barnstead).

#### **4.4.2. Synthesis of graphene (ME-LOGr)**

ME-LOGr was synthesized as described previously[22]. Briefly, 20 mg of graphite were added in to a mixture of sulfuric acid and nitric acid (1:1) and was subjected to 30 seconds of microwave irradiation. The graphene product was then filtered and was extensively washed with water. Finally, the collected purified product was re-suspended into water using bath sonication for 30 minutes.

#### **4.4.3. Synthesis of carbon nanotube**

CNTs (HiPCO SWNT, CNANO-MWNT, and CNANO-SWNT) were functionalized and suspended in DI-water as described in Chapter 3. Briefly, 10 mg (unless mentioned otherwise) of CNT was mixed into a mixture of sulfuric acid and nitric acid at 1:1 ratio. This final mixture was then placed into a CEM Discover microwave reactor and irradiated for 30 seconds at a fixed power of 300 Watts. The products were then filtered and were extensively washed with DI-water. Finally, the collected purified product was re-suspended into water using bath sonication for 30 minutes.

#### **4.4.4. Graphene and graphene/CNT hybrid film via filtration**

The hybrid films were prepared using vacuum filtration method as described[36] on glass slides as substrates by Buchner vacuum filtration of the graphene/CNT suspensions onto Anodisc 47 inorganic Alumina membranes with 200 nm pores (Whatman Ltd.). After filtration, the thin films were dried in air for 15-20 min. After drying, the graphene/CNT on alumina filter was placed directly into a 1M NaOH bath. The alumina filter was completely dissolved, resulting in a thin film floating on the surface. The NaOH bath was then exchanged with DI-water by draining and refilling until neutral pH. The floating film was allowed to slowly descend and attach onto a pre-positioned glass substrate at the bottom. The film was then air dried for 30 minutes and was further dried in an oven at 60 °C overnight.

#### **4.4.5. Self-assembly of graphene and graphene/CNT hybrid thin films**

In order to form self-assembly films, typically, an aqueous solution of graphene or graphene/CNT mixture with different ratios was added into a glass vial, then a certain amount of toluene was layered on top forming a biphasic system to create an interface between the organic and aqueous phases with 4:1 (water:toluene) as the final ratio. To aid the formation of films, ethanol with desired amount was also added. It was later found that gentle shaking or mild bubbling of the mixture could result in spontaneous formation of the interfacial films. After leaving the films undisturbed for about 3 hours, all liquids were slowly removed, and the floating film was allowed to slowly descend and attach onto a

pre-positioned glass or quartz substrate at the bottom. The film was then air dried for 30 minutes and was further dried in an oven at 60 °C overnight.

#### **4.4.6. Characterizations**

Optical transmittance of thin films was measured by a Varian Cary 500 spectrophotometer in a range of 200 – 800 nm. Surface resistivity of the thin films was determined by a manual four point resistivity probe (Lucas Laboratories, model 302). SEM samples were prepared by the thin film transfer method described in details below. All SEM images were collected using a Hitachi S-4800 field emission scanning electron microscope (FE-SEM, Hitachi Co. Ltd. S-4800) under small accelerating voltage (1-2 KV) and a high probe current (15-20  $\mu$ A) to obtain images with high contrast.

#### 4.5: REFERENCES:

1. Zhu, Y., Murali, S., Cai, W., Li, X., Suk, J.W., Potts, J.R., and Ruoff, R.S., *Graphene and graphene oxide: synthesis, properties, and applications*. Adv Mater, 2010. **22**(35): p. 3906-24.
2. Eda, G. and Chhowalla, M., *Chemically derived graphene oxide: towards large-area thin-film electronics and optoelectronics*. Adv Mater, 2010. **22**(22): p. 2392-415.
3. Loh, K.P., Bao, Q., Eda, G., and Chhowalla, M., *Graphene oxide as a chemically tunable platform for optical applications*. Nat Chem, 2010. **2**(12): p. 1015-24.
4. Kim, K.S., Zhao, Y., Jang, H., Lee, S.Y., Kim, J.M., Ahn, J.H., Kim, P., Choi, J.Y., and Hong, B.H., *Large-scale pattern growth of graphene films for stretchable transparent electrodes*. Nature, 2009. **457**(7230): p. 706-10.
5. Li, X., Cai, W., An, J., Kim, S., Nah, J., Yang, D., Piner, R., Velamakanni, A., Jung, I., Tutuc, E., Banerjee, S.K., Colombo, L., and Ruoff, R.S., *Large-area synthesis of high-quality and uniform graphene films on copper foils*. Science, 2009. **324**(5932): p. 1312-4.
6. Li, X., Cai, W., Colombo, L., and Ruoff, R.S., *Evolution of graphene growth on Ni and Cu by carbon isotope labeling*. Nano Lett, 2009. **9**(12): p. 4268-72.
7. Reina, A., Jia, X., Ho, J., Nezich, D., Son, H., Bulovic, V., Dresselhaus, M.S., and Kong, J., *Large Area, Few-Layer Graphene Films on Arbitrary Substrates by Chemical Vapor Deposition*. Nano Lett, 2008. **9**(1): p. 30-35.
8. Chen, J.-H., Jang, C., Xiao, S., Ishigami, M., and Fuhrer, M.S., *Intrinsic and extrinsic performance limits of graphene devices on SiO<sub>2</sub>*. Nat Nano, 2008. **3**(4): p. 206-209.
9. Dreyer, D.R., Park, S., Bielawski, C.W., and Ruoff, R.S., *The chemistry of graphene oxide*. Chem Soc Rev, 2010. **39**(1): p. 228-40.
10. Li, D., Muller, M.B., Gilje, S., Kaner, R.B., and Wallace, G.G., *Processable aqueous dispersions of graphene nanosheets*. Nat Nanotechnol, 2008. **3**(2): p. 101-5.
11. Blake, P., Brimicombe, P.D., Nair, R.R., Booth, T.J., Jiang, D., Schedin, F., Ponomarenko, L.A., Morozov, S.V., Gleeson, H.F., Hill, E.W., Geim, A.K.,

- and Novoselov, K.S., *Graphene-based liquid crystal device*. Nano Lett, 2008. **8**(6): p. 1704-8.
12. Watcharotone, S., Dikin, D.A., Stankovich, S., Piner, R., Jung, I., Dommett, G.H., Evmenenko, G., Wu, S.E., Chen, S.F., Liu, C.P., Nguyen, S.T., and Ruoff, R.S., *Graphene-silica composite thin films as transparent conductors*. Nano Lett, 2007. **7**(7): p. 1888-92.
  13. Becerril, H.A., Mao, J., Liu, Z., Stoltenberg, R.M., Bao, Z., and Chen, Y., *Evaluation of solution-processed reduced graphene oxide films as transparent conductors*. ACS Nano, 2008. **2**(3): p. 463-70.
  14. Eda, G., Fanchini, G., and Chhowalla, M., *Large-area ultrathin films of reduced graphene oxide as a transparent and flexible electronic material*. Nat Nanotechnol, 2008. **3**(5): p. 270-4.
  15. De, S., King, P.J., Lotya, M., O'Neill, A., Doherty, E.M., Hernandez, Y., Duesberg, G.S., and Coleman, J.N., *Flexible, transparent, conducting films of randomly stacked graphene from surfactant-stabilized, oxide-free graphene dispersions*. Small, 2010. **6**(3): p. 458-64.
  16. Cote, L.J., Kim, F., and Huang, J., *Langmuir-Blodgett assembly of graphite oxide single layers*. J Am Chem Soc, 2009. **131**(3): p. 1043-9.
  17. Kim, F., Cote, L.J., and Huang, J., *Graphene oxide: surface activity and two-dimensional assembly*. Adv Mater, 2010. **22**(17): p. 1954-8.
  18. Deegan, R.D., Bakajin, O., Dupont, T.F., Huber, G., Nagel, S.R., and Witten, T.A., *Capillary flow as the cause of ring stains from dried liquid drops*. Nature, 1997. **389**(6653): p. 827-829.
  19. Wu, Z., Chen, Z., Du, X., Logan, J.M., Sippel, J., Nikolou, M., Kamaras, K., Reynolds, J.R., Tanner, D.B., Hebard, A.F., and Rinzler, A.G., *Transparent, conductive carbon nanotube films*. Science, 2004. **305**(5688): p. 1273-6.
  20. Eda, G., Fanchini, G., and Chhowalla, M., *Large-area ultrathin films of reduced graphene oxide as a transparent and flexible electronic material*. Nat Nano, 2008. **3**(5): p. 270-274.
  21. Kong, B.-S., Geng, J., and Jung, H.-T., *Layer-by-layer assembly of graphene and gold nanoparticles by vacuum filtration and spontaneous reduction of gold ions*. Chemical Communications, 2009(16): p. 2174-2176.



22. Chiu, P.L., Mastrogiovanni, D.D., Wei, D., Louis, C., Jeong, M., Yu, G., Saad, P., Flach, C.R., Mendelsohn, R., Garfunkel, E., and He, H., *Microwave- and nitronium ion-enabled rapid and direct production of highly conductive low-oxygen graphene*. J Am Chem Soc, 2012. **134**(13): p. 5850-6.
23. Myers, D., *Surfactant Science And Technology* 2006, Hoboken, NJ: Wiley-Interscience.
24. Rao, C.N.R. and Kalyanikutty, K.P., *The Liquid-Liquid Interface as a Medium To Generate Nanocrystalline Films of Inorganic Materials*. Acc Chem Res, 2008. **41**(4): p. 489-499.
25. Reincke, F., Hickey, S.G., Kegel, W.K., and Vanmaekelbergh, D., *Spontaneous assembly of a monolayer of charged gold nanocrystals at the water/oil interface*. Angew Chem Int Ed Engl, 2004. **43**(4): p. 458-62.
26. Pieranski, P., *Two-Dimensional Interfacial Colloidal Crystals*. Physical Review Letters, 1980. **45**(7): p. 569-572.
27. Lin, Y., Skaff, H., Emrick, T., Dinsmore, A.D., and Russell, T.P., *Nanoparticle assembly and transport at liquid-liquid interfaces*. Science, 2003. **299**(5604): p. 226-9.
28. Kim, J., Cote, L.J., Kim, F., Yuan, W., Shull, K.R., and Huang, J., *Graphene oxide sheets at interfaces*. J Am Chem Soc, 2010. **132**(23): p. 8180-6.
29. Paredes, J.I., Villar-Rodil, S., Martinez-Alonso, A., and Tascon, J.M., *Graphene oxide dispersions in organic solvents*. Langmuir, 2008. **24**(19): p. 10560-4.
30. Reincke, F., Hickey, S.G., Kegel, W.K., and Vanmaekelbergh, D., *Spontaneous Assembly of a Monolayer of Charged Gold Nanocrystals at the Water/Oil Interface*. Angewandte Chemie, 2004. **116**(4): p. 464-468.
31. Kim, S.-S., Choi, S.-Y., Park, C.-G., and Jin, H.-W., *Transparent conductive ITO thin films through the sol-gel process using metal salts*. Thin Solid Films, 1999. **347**(1-2): p. 155-160.
32. Al-Dahoudi, N., Bisht, H., Göbbert, C., Krajewski, T., and Aegerter, M.A., *Transparent conducting, anti-static and anti-static-anti-glare coatings on plastic substrates*. Thin Solid Films, 2001. **392**(2): p. 299-304.

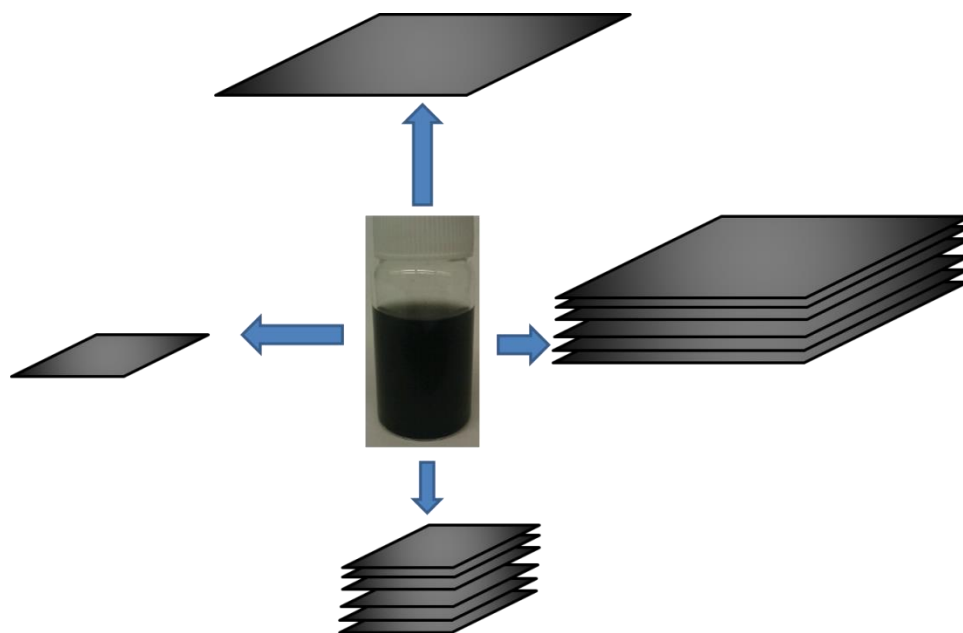
33. Tung, V.C., Chen, L.M., Allen, M.J., Wassei, J.K., Nelson, K., Kaner, R.B., and Yang, Y., *Low-temperature solution processing of graphene-carbon nanotube hybrid materials for high-performance transparent conductors*. Nano Lett, 2009. **9**(5): p. 1949-55.
34. Hong, T.K., Lee, D.W., Choi, H.J., Shin, H.S., and Kim, B.S., *Transparent, flexible conducting hybrid multilayer thin films of multiwalled carbon nanotubes with graphene nanosheets*. ACS Nano, 2010. **4**(7): p. 3861-8.
35. Suslick, K.S., *Sonochemistry*. Science, 1990. **247**(4949): p. 1439-45.
36. Kong, B.-S., Jung, D.-H., Oh, S.-K., Han, C.-S., and Jung, H.-T., *Single-Walled Carbon Nanotube Gold Nanohybrids: Application in Highly Effective Transparent and Conductive Films*. The Journal of Physical Chemistry C, 2007. **111**(23): p. 8377-8382.

## **Chapter 5: Size-dependent separation of graphene sheets**

### **5.1. INTRODUCTION:**

Graphene has been suggested as the ultimate alternative to carbon nanotubes for future technological applications in many fields, such as electronics, sensors, and batteries, due to the low cost, abundant availability and wonderful properties[1-5]. A majority of liquid phase exfoliated graphene suspensions contains a wide distribution of sizes of graphene (see scheme 5.1). However, one of the requirements for developing the aforementioned potential applications is the availability of graphene sheets with uniform and appropriate sizes, and controllable surface modifications. For examples, single-layered large-sized graphene sheets with only mild oxidation are required for many high-end applications[6-9], while applications in drug delivery fields require molecular-sized graphene nanosheets that are typically less than 100 nm with extensive oxidation for conjugation of antibodies or drugs via many coupling reactions[10, 11]. To achieve this goal, most of graphene products must then be post-treated and purified to separate the desired products from the rest. However, common separation methods are mainly based on centrifugation, which can be rather time-consuming and difficult to practice on a large scale, which would become a major obstacle for industrial purposes. Recently, a major breakthrough in separating graphene oxide sheets by different sizes has been accomplished by

isopycnic density gradient ultracentrifugation (DGU)[12] using a sucrose solution as density gradients. However, this DGU method can only be applied to only heavily oxidized graphene sheets due to the requirement of a high hydration degree around each graphene sheet[13]. Shi et al. reported another method, which separated different size of GO by adjusting the pH of the GO solution[14]. In their method, two fractions of GO solution was separated, and SEM images revealed that GO sheets with lateral size of about 10  $\mu\text{m}$  were isolated from the smaller sheets (2-6  $\mu\text{m}$ ).



**Scheme 5.1:** Schematic depicting a single suspension consists of graphene with various lateral sizes and thicknesses.

On the other hand, the biphasic extraction technique is scalable and has been used to extract gold nanoparticles from aqueous phases into organic

phases by using common phase transfer catalysts[15], This work has been further extended to show that size-selective extractions of gold nanoparticles can be achieved[16, 17]. The mechanism behind is mainly based on the electrostatic interactions. However, this method was limited to only small nanoparticles. They found that nanoparticles greater than 10 nm simply could not be transferred with ion pairs between tetra-octylammonium cations and citrate anions. The smaller the nanoparticles are, the higher specific surface area they possessed, and thus they bear higher density of ion pair in each particle, resulting in more hydrophobic forces to be exerted on these particles.

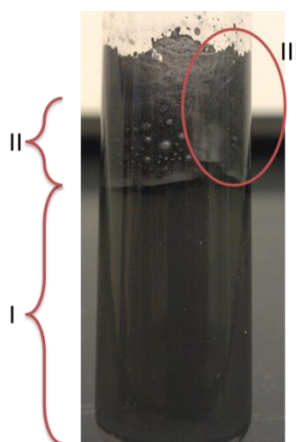
In this chapter, we report a new and easily scalable liquid-liquid interfacial separation of graphene sheets. Raman spectroscopy and scanning electron microscope are used to characterize the effect of separations. Not only is this approach much simpler than the DGU method, but the results showed that the separations at toluene-water interfaces are based on sizes and charge densities of graphene sheets.

## **5.2. RESULTS AND DISCUSSION:**

### **5.2.1. Self-separation in biphasic systems**

A typical biphasic separation system is setup by first adding desired amounts of toluene to an aqueous graphene suspension. Two distinct phases are readily formed. At this point, there is no graphene transferred to the newly created liquid/liquid interface. To initiate the transportation of graphene sheets from the bulk water phase to the interface, an input of mechanical work is

required. Figure 5.1 shows a photo of the bi-phasic system after being vigorously mixed. Immediately after vigorous agitation of the biphasic solution, different self-assembled morphologies can be observed. This external mechanical force breaks the two immiscible liquids into small droplets, which creates a large increase in interfacial area. This disturbance also generates large amounts of entropy, which preferentially promotes graphene sheets to adsorb at the liquid/liquid interface by minimizing the interfacial free energy. In general, there are three main phases: I) a clear graphene suspension in the aqueous phase, II) an organic phase with some visible bubbles in millimeter scale (see figure 5.2 for a close up) and III) a thick film of graphitic materials creeping up to the walls of the containers. These observations are similar to the phenomenon observed with gold nanoparticles at water-heptane-glass interface[18].



**Figure 5.1:** A digital photograph of graphene suspension and toluene bi-phasic system after being vigorously mixed, showing three main regions: I) a clear graphene suspension in the aqueous phase, II) an organic phase with some visible bubbles in millimeter scale and III) a thick film of graphitic materials creeping up to the walls of the containers.

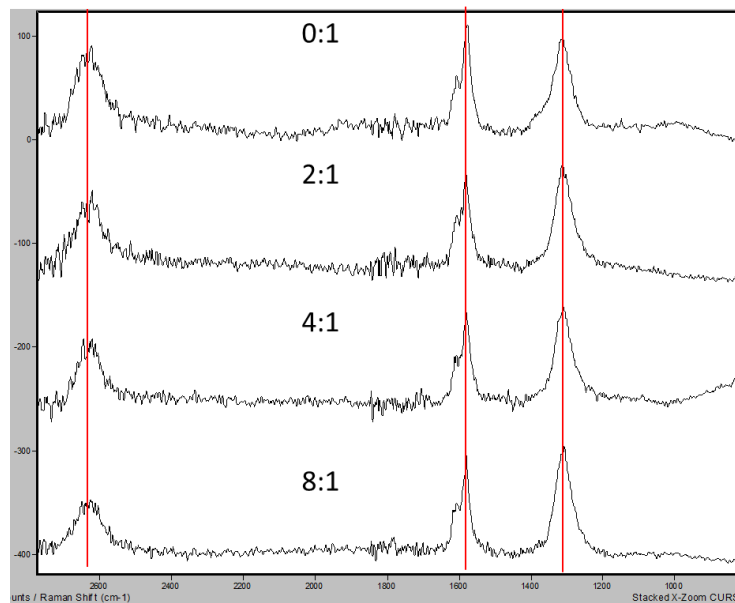


**Figure 5.2:** A zoomed in digital photograph of region II in figure 5.1, showing large emulsion at the toluene/water interface.

### 5.2.2. Raman spectroscopy

Raman spectroscopy has been extensively used for the characterization of carbon-based materials, such as graphene and carbon nanotubes[19, 20], for their electronic signatures and surface chemistries. We used Raman spectroscopy to evaluate the oxidation states of the graphene sheets using different separation parameters. Figure 5.3 shows Raman spectra of different graphene samples after separations with biphasic systems prepared with different toluene/water ratios. The electronic structure of graphene is very sensitive to Raman spectroscopy. One can easily obtain details about the electronic structure of graphene by using the D/G (D band/G band) ratio. The D band directly relates to the defects on graphene sheet, while the G band correlates with the graphitic carbons in the graphene basal planes. Thus, from

the D/G ratio shown here, the solution without interfacial trapping is much lower than all the ones after interfacial trapping, indicating that the suspended graphene has fewer defects (on average) compared to the others. However, all films cast from solutions after interfacial trapping have higher D/G ratio, indicating that the graphene in these solutions have more defects. It can then be interpreted that graphene separated



**Figure 5.3:** Raman spectra of different graphene samples after separations with biphasic systems prepared with different toluene/water ratios

from the solution via interfacial trapping method are the less defective, less oxidized. The calculated ratios are summarized in table 5.1.



### 5.2.3: Scanning electron microscopy (SEM)

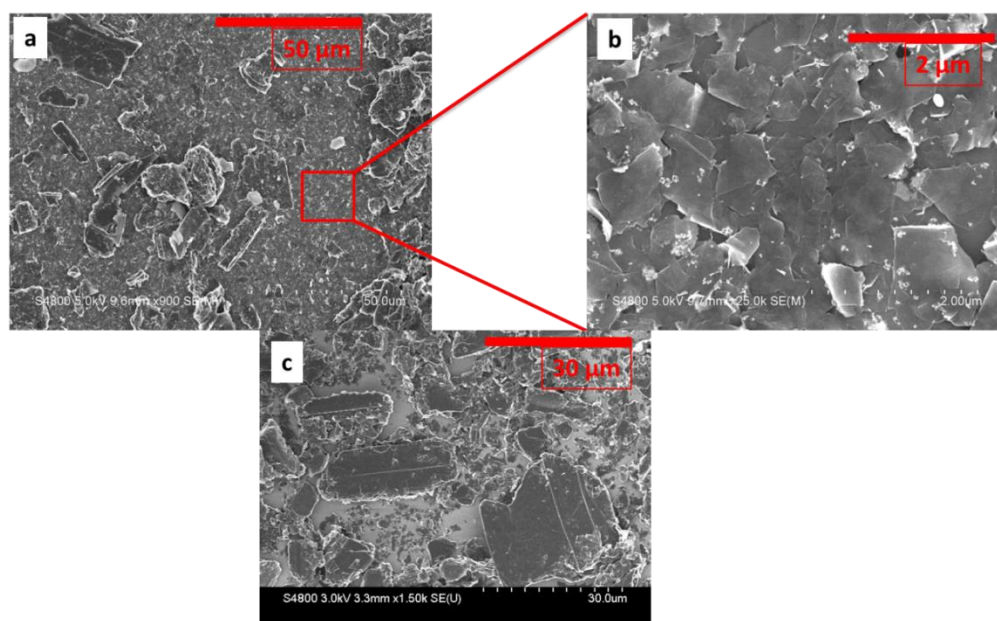
Based on the interfacial free energy theory that is discussed in previous chapters, graphene sheets with larger planar areas should be more readily trapped at the oil/water interface. We then used SEM to reveal sizes, morphology and orientation of the graphene sheet after separation. Figure 5.4a, shows the SEM image of the thick film formed on the sidewalls of the glass test tube. As shown, the whole imaged area was covered with deposits. Large pieces of unreacted graphite particles were observed. These particles can range up to 40 - 50  $\mu\text{m}$  and

| T:W | $\sim 1580\text{ (cm}^{-1}\text{)}$ | $\sim 1320\text{ (cm}^{-1}\text{)}$ | D/G   |
|-----|-------------------------------------|-------------------------------------|-------|
| 8:1 | 129                                 | 140                                 | 1.085 |
| 4:1 | 159                                 | 167                                 | 1.05  |
| 2:1 | 54                                  | 61                                  | 1.12  |
| 0:1 | 110                                 | 96                                  | 0.82  |

**Table 5.1:** List of positions of D band and G bands, and their ratios with various toluene-to-water (T:W) ratios.

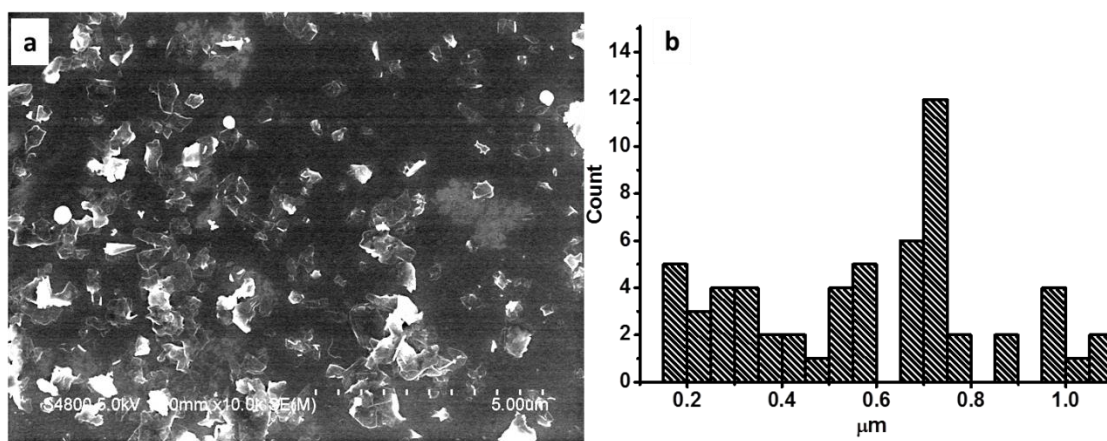
are distributed across the area. Figure 5.4b is an SEM image of the area in the box in figure 5.4a under high magnification. This image reveals that a uniform

film was underneath the unreacted graphite particles. This film indeed consisted of mainly graphene sheets in the range up to 2  $\mu\text{m}$  and was relatively uniform over a macroscopic sized area. The graphene sheets are well interconnected with wrinkles clearly observed against the dark background (bright features in images). Wrinkles appeared to be bright in the SEM images due to the strongly scattered electrons entering the detector lens[21]. This suggests that the separation reaction was a spontaneous reaction, where overlapping which requires graphene to slowly stack onto each other was not observed. Figure 5.4c shows another spot on the sample consisting only of large unreacted graphite particles.



**Figure 5.4:** SEM images of (a) the thick film formed on the sidewalls of the glass test tube. b) a high magnification image of the area in the red box, showing a uniform film was underneath the unreacted graphite particles, and c) a spot on the sample consisting only large unreacted graphite particles.

The aqueous phase of the system was also characterized using SEM. Figure 5.5a shows the graphene sheets in the bottom phase. Interestingly, no unreacted graphite particles were observed, indicating that they were completely removed from the aqueous phase via the interfacial separation. However, these graphene sheets are relatively small with a range from 0.2  $\mu\text{m}$  to about 1.2  $\mu\text{m}$ , with a mean value of about 0.7  $\mu\text{m}$  (see distribution plot in figure 5.5b).



**Figure 5.5:** a) A SEM image of the stable solution after mixing in the aqueous phase, showing no big unreacted graphite particles. b) A distribution plot for of the lateral sizes of the graphene sheets in a).

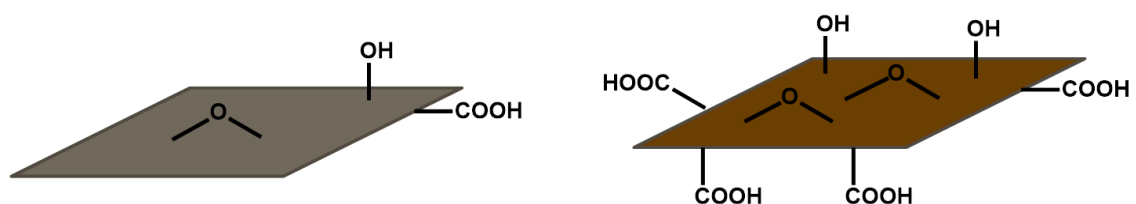
#### 5.2.4. Size- and oxidation-dependent separation of graphene sheets

Nanomaterials, including graphene, are highly mobile at the interface and an equilibrium state between the two interfaces can be rapidly achieved by self-assembly at the interface due to the tendency to reduce their interfacial energy.

As stated in previous chapter, the interfacial self-assembly reaction reduces the entropy by the Boltzmann factor[22-24]. Thus, the stability of the particles at the interface is directly related to the gain in interfacial energy, and the three interfacial energies are related to each other through the three phase contact angle, which can be expressed as follows[23]:


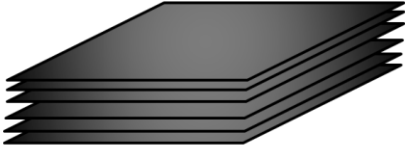


$$\cos \theta = \frac{A(\gamma_{PO} - \gamma_{PW})}{\gamma_{OW}}$$

where the  $\gamma$ 's correspond to different interfacial energies( $\gamma_{PO}$ ,  $\gamma_{PW}$ , and  $\gamma_{OW}$  are the interfacial energies between the particle and oil phase, the particle and water phase and oil phase and water phase, respectively), and  $\theta$  is the three face contact angle. In 2002, Bink and Clint reported there are two main parameters, which are influencing their interfacial energy, therefore the assembly process at the interface: 1) the surface modification, and 2) the shapes and the sizes of the materials at the interface[25]. Surface modification directly affects the hydrophilicity of the materials in the aqueous phase, while different shapes and sizes contribute variously in surface area,  $A$ , in the equation above, thus greatly varying the interfacial energy. These were in fact directly observed in the Raman and SEM data discussed above.



**Figure 5.6:** Illustrations of two same-size graphene sheets with different oxidation state, thus different amount of oxygen-containing groups on the surfaces.

For instance, as shown in figure 5.6, two graphene sheets with the same size but with different oxidation state. On the left is ME-LOGr graphene with only slight oxidation, while GO (right) is heavily oxidized, bearing many more oxygen-containing groups. According to Binks *et al.*, these two species have dramatic differences in terms of interfacial energy. GO, being heavily oxidized with its surface largely decorated with hydrophilic oxygen-containing groups, is extremely soluble in water. This high solubility results in high interfacial energy between GO and water, thus adsorption at the interface would be highly suppressed. On the other hand, the ME-LOGr being slightly oxidized, has a large amount of intact graphitic domains with only a small degree of surface modification, lowering the interfacial energy between them and water. Thus, adsorption of the slightly oxidized at the liquid/liquid interface would be greatly promoted.

|   |         |                                       |
|---|---------|---------------------------------------|
|  | 1 layer | $0.4 \times 2 \times (2L)^2$          |
|  | 6 layer | $6 \times 0.4 \times 2 \times (2L)^2$ |
|  | 6 layer | $6 \times 0.4 \times 2 \times (L)^2$  |
|  | 1 layer | $0.4 \times 2 \times (L)^2$           |

**Table 5.2:** A summary of several square graphene species with various thicknesses and sizes, and their corresponding surface areas.

Particle size and shape are also important means for a nanomaterial to gain interfacial energy at the liquid/liquid interface. Different from spherical nanoparticles, flat-shaped particles including graphene sheets are characterized by two different axes; the longer axis along the width of the graphene sheets and the ratio of the two axes along the width and the thickness of the nanosheets, thus the aspect ratio. A series of the estimations are summarized in table 2. For example, the aspect ratio of large and thin graphene sheets can be estimated to be 6250 if the thickness and the average lateral size of the thickness are taken as 5  $\mu\text{m}$  and 0.8 nm, respectively. On the other hand, the aspect ratio would dramatically decrease if the graphene sheet were both small and thick; for instance, a graphene sheet with 1  $\mu\text{m}$  and 4.8 nm (6 layers), in width and

thickness, its aspect ratio is about 208. It can be predicted that the attachment at the liquid/liquid interface of the larger and thinner graphene sheet with much higher aspect ratio, is much more favorable because of the large gain in the interfacial energy.

In combination with the Raman data, it can be concluded that we successfully separated the smaller and thin graphene sheets from other exfoliated graphene. These small and thin graphene sheets had the tendency to stay in the aqueous phase due to the fact that their surface is more oxidized (higher D/G ratio), thus more hydrophilic, minimizing the gain of interfacial energy. In addition, these small graphene sheets have smaller aspect ratio than desired for adsorption, thus it is more favorable to stay suspended in aqueous phase. However, further investigations are needed to optimize the extracting system based on the manipulation of different surface chemistries and aspect ratio of other exfoliated materials. It has also been recently shown that the combination of surface chemistry and sizes of graphene sheets were a parameter for tunable amphiphilicity[26]. Since the amphiphilicity of graphene sheets comes from the hydrophilic alcohol and carboxylic acid groups on the edges, while the hydrophobicity originates from the intact graphitic domains on their basal planes. The edge-to-plane ratio is expected to be much smaller in larger graphene sheets than that in small graphene sheets. Thus, even in the same environment, smaller graphene sheets are expected to be more hydrophilic than the larger-sized graphene sheets[26], making them more preferentially be suspended in the

aqueous phase, while the larger ones would be more kinetically favorable for adsorption at the interface with a significant gain in the interfacial energy. This promising method is now being investigated in our group.

### **5.3. CONCLUSION:**

A biphasic interfacial trapping/extraction method has been developed to separate highly-oxidized small graphene sheets from other exfoliated materials by taking advantage of their surface modification and aspect ratio. This rapid, scalable and non-destructive method results in monodispersed ME-LOGr sheets suspended in aqueous phase with high stability. The separation method opened a way of obtaining graphene sheets with suitable sizes and surface modifications in bulk quantities. Further and consecutive trappings might provide a robust method to both purify and selectively fractionalize graphene with different sizes and different properties for many future applications.

### **5.4. MATERIALS AND METHODS:**

#### **5.4.1. Materials:**

Graphite powder (synthetic; <20  $\mu\text{m}$ ) used in all experiments was purchased from Sigma-Aldrich and used as received. Anhydrous toluene (ACS grade), sulfuric acid (98 %) and nitric acid (70%) were purchased from Pharmco-AAPER and used as-received. All solutions were prepared using deionized water (18.2 M $\Omega$ ) (Nanopure water, Barnstead). All samples were cleaned and rinsed with the same deionized water.



## **5.4.2. Methods:**

### **5.4.2.1. Synthesis of graphene**

ME-LOGr was synthesized as described previously[27]. Briefly, 20 mg of graphite was added in to a mixture of sulfuric acid and nitric acid (1:1) and was subjected to 30 seconds of microwave irradiation. The graphene product was then filtered and was extensively washed with water. Finally, the collected purified product was re-suspended into water using bath sonication for 30 minutes.

### **5.4.2.2. Interfacial separation of graphene**

Size separation of water-soluble graphene into organic phases was performed by a two-phase method. Typically, a separation was done based on 8 mL of graphene suspension. Different volumes of toluene were added into a glass test tube and were mixed and shaken vigorously. For example, in the separation experiment with a ratio of 4:1, 8 mL of graphene solution was added into a glass test tube, and then 2 mL of anhydrous toluene was layered on top of the water phase, followed by vigorously mixing. The mixtures were left undisturbed for 60 minutes for the systems to reach equilibrium. Different morphologies were observed (see results and discussions), indicating that the separations were successful.

#### **5.4.2.3. Characterizations:**

Samples for Raman spectroscopy were prepared by drying the aqueous phase of graphene suspension after separations onto aluminum filter membrane. Raman spectra of films were collected in a Kaiser Optical Systems Raman Microprobe with a 785 nm solid state diode laser. Spectra were acquired using a 30 s exposure time. SEM samples were prepared by either dip-coating or drop-casting of the corresponding phase in the glass test tube on to pre-cleaned Si/SiO<sub>2</sub> substrates. The substrates were first cleaned with UV/Ozone for 10 minutes, followed by 5 minutes in piranha solution to remove any organic impurities, and finally sonicated and washed with DI water, then were dried under nitrogen stream.

## 5.5. REFERENCES:

1. Geim, A.K. and K.S. Novoselov, *The rise of graphene*. Nat Mater, 2007. **6**(3): p. 183-91.
2. Li, X., X. Wang, L. Zhang, S. Lee, and H. Dai, *Chemically derived, ultrasmooth graphene nanoribbon semiconductors*. Science, 2008. **319**(5867): p. 1229-32.
3. Dikin, D.A., S. Stankovich, E.J. Zimney, R.D. Piner, G.H. Dommett, G. Evmenenko, S.T. Nguyen, and R.S. Ruoff, *Preparation and characterization of graphene oxide paper*. Nature, 2007. **448**(7152): p. 457-60.
4. Fowler, J.D., M.J. Allen, V.C. Tung, Y. Yang, R.B. Kaner, and B.H. Weiller, *Practical chemical sensors from chemically derived graphene*. ACS Nano, 2009. **3**(2): p. 301-6.
5. Wang, L., K. Lee, Y.-Y. Sun, M. Lucking, Z. Chen, J.J. Zhao, and S.B. Zhang, *Graphene Oxide as an Ideal Substrate for Hydrogen Storage*. ACS Nano, 2009. **3**(10): p. 2995-3000.
6. Yin, Z., S. Wu, X. Zhou, X. Huang, Q. Zhang, F. Boey, and H. Zhang, *Electrochemical Deposition of ZnO Nanorods on Transparent Reduced Graphene Oxide Electrodes for Hybrid Solar Cells*. Small, 2010. **6**(2): p. 307-312.
7. Bunch, J.S., A.M. van der Zande, S.S. Verbridge, I.W. Frank, D.M. Tanenbaum, J.M. Parpia, H.G. Craighead, and P.L. McEuen, *Electromechanical resonators from graphene sheets*. Science, 2007. **315**(5811): p. 490-3.
8. Novoselov, K.S., A.K. Geim, S.V. Morozov, D. Jiang, M.I. Katsnelson, I.V. Grigorieva, S.V. Dubonos, and A.A. Firsov, *Two-dimensional gas of massless Dirac fermions in graphene*. Nature, 2005. **438**(7065): p. 197-200.
9. Ang, P.K., S. Wang, Q. Bao, J.T. Thong, and K.P. Loh, *High-throughput synthesis of graphene by intercalation-exfoliation of graphite oxide and study of ionic screening in graphene transistor*. ACS Nano, 2009. **3**(11): p. 3587-94.
10. Liu, Z., J.T. Robinson, X. Sun, and H. Dai, *PEGylated nanographene oxide for delivery of water-insoluble cancer drugs*. J Am Chem Soc, 2008. **130**(33): p. 10876-7.

11. Sun, X., Z. Liu, K. Welsher, J.T. Robinson, A. Goodwin, S. Zaric, and H. Dai, *Nano-Graphene Oxide for Cellular Imaging and Drug Delivery*. Nano Res, 2008. **1**(3): p. 203-212.
12. Sun, X., D. Luo, J. Liu, and D.G. Evans, *Monodisperse Chemically Modified Graphene Obtained by Density Gradient Ultracentrifugal Rate Separation*. ACS Nano, 2010. **4**(6): p. 3381-3389.
13. Sun, X., S.M. Tabakman, W.-S. Seo, L. Zhang, G. Zhang, S. Sherlock, L. Bai, and H. Dai, *Separation of Nanoparticles in a Density Gradient: FeCo@C and Gold Nanocrystals*. Angewandte Chemie International Edition, 2009. **48**(5): p. 939-942.
14. Wang, X., H. Bai, and G. Shi, *Size Fractionation of Graphene Oxide Sheets by pH-Assisted Selective Sedimentation*. Journal of the American Chemical Society, 2011. **133**(16): p. 6338-6342.
15. Chen, S., H. Yao, and K. Kimura, *Reversible Transference of Au Nanoparticles across the Water and Toluene Interface: A Langmuir Type Adsorption Mechanism*. Langmuir, 2001. **17**(3): p. 733-739.
16. Cheng, W. and E. Wang, *Size-Dependent Phase Transfer of Gold Nanoparticles from Water into Toluene by Tetraoctylammonium Cations: A Wholly Electrostatic Interaction*. The Journal of Physical Chemistry B, 2003. **108**(1): p. 24-26.
17. Yao, H., O. Momozawa, T. Hamatani, and K. Kimura, *Stepwise Size-Selective Extraction of Carboxylate-Modified Gold Nanoparticles from an Aqueous Suspension into Toluene with Tetraoctylammonium Cations*. Chemistry of Materials, 2001. **13**(12): p. 4692-4697.
18. Reincke, F., S.G. Hickey, W.K. Kegel, and D. Vanmaekelbergh, *Spontaneous assembly of a monolayer of charged gold nanocrystals at the water/oil interface*. Angew Chem Int Ed Engl, 2004. **43**(4): p. 458-62.
19. Dresselhaus, M.S., G. Dresselhaus, R. Saito, and A. Jorio, *Raman spectroscopy of carbon nanotubes*. Physics Reports, 2005. **409**(2): p. 47-99.
20. Dresselhaus, M.S., A. Jorio, A.G. Souza Filho, and R. Saito, *Defect characterization in graphene and carbon nanotubes using Raman spectroscopy*. Philos Transact A Math Phys Eng Sci, 2010. **368**(1932): p. 5355-77.

21. Cote, L.J., J. Kim, V.C. Tung, J. Luo, F. Kim, and J. Huang, *Graphene oxide as surfactant sheets*. Pure and Applied Chemistry, 2011. **83**(1): p. 95-110.
22. Bowden, N., A. Terfort, J. Carbeck, and G.M. Whitesides, *Self-Assembly of Mesoscale Objects into Ordered Two-Dimensional Arrays*. Science, 1997. **276**(5310): p. 233-235.
23. Lin, Y., H. Skaff, T. Emrick, A.D. Dinsmore, and T.P. Russell, *Nanoparticle assembly and transport at liquid-liquid interfaces*. Science, 2003. **299**(5604): p. 226-9.
24. Binder, W.H., *Supramolecular Assembly of Nanoparticles at Liquid-Liquid Interfaces*. Angewandte Chemie International Edition, 2005. **44**(33): p. 5172-5175.
25. Binks, B.P. and J.H. Clint, *Solid Wettability from Surface Energy Components: Relevance to Pickering Emulsions*. Langmuir, 2002. **18**(4): p. 1270-1273.
26. Kim, J., L.J. Cote, F. Kim, W. Yuan, K.R. Shull, and J. Huang, *Graphene oxide sheets at interfaces*. J Am Chem Soc, 2010. **132**(23): p. 8180-6.
27. Chiu, P.L., D.D. Mastrogiovanni, D. Wei, C. Louis, M. Jeong, G. Yu, P. Saad, C.R. Flach, R. Mendelsohn, E. Garfunkel, and H. He, *Microwave- and nitronium ion-enabled rapid and direct production of highly conductive low-oxygen graphene*. J Am Chem Soc, 2012. **134**(13): p. 5850-6.

## **Chapter 6: Thermally-responsive liquid-filled PNIPAM/graphene microsphere *via* self-assembly by O/W emulsion for drug delivery applications.**

### **6.1: INTRODUCTION**

Recently, GO and reduced GO (rGO) have been exploited to deliver hydrophobic drugs based on their exceptionally large surface area (doubled the surface area of carbon nanotubes) and partially aromatic structures. Drug loading and controlled release depend on the hydrophobic and  $\pi$ - $\pi$  interactions between the drug molecules and GO or rGO surface. However, a slight structural change of the drugs or the surface structures of graphene causes a dramatic change of drug loading efficiency and the capability for controlled release. It is difficult to simultaneously deliver multiple drugs in controlled drug ratios and quantities with a time programmed release profiles, which are critical factors for efficient combination therapeutics. In this chapter, we develop a novel approach to encapsulate hydrophobic drugs by exploiting the intrinsic amphiphilic properties of the microwave enabled low oxygen graphene (ME-LOGr). By conjugating a thermal-sensitive polymer, here poly(*N*-isopropylacrylamide) amine-terminated (PNIPAM), onto ME-LOGr, a controlled release of the drug can be realized. In this preliminary study, we used a hydrophobic dye to demonstrate the concept,

demonstrating the great potential in developing multifunctional drug delivery systems.

## **6.2: RESULT AND DISCUSSION:**

### **6.2.1: Amphiphilicity of ME-LOGr at an oil-water interface**

As discussed previously[1] and in **Chapter 2**, the graphene used here contained a small number of hydroxyl and epoxy groups on its basal planes, and with carboxylic acid groups on their edges. These functional groups enhanced its solubility and dispersion in aqueous solutions. On the other hand, the unfunctionalized regions, on its basal plane, are mainly  $\pi$ - $\pi$  conjugated networks of polyaromatic hydrocarbons. Thus, it is reasonable that the ME-LOGr can be viewed as amphiphiles[2, 3] which would act just like surfactants at an oil-water interface. To demonstrate this idea, we studied its ability to form of emulsion in water-toluene biphasic systems. The stability of an emulsion is generally defined as the ability for the formed emulsion droplets from collapsing. There are two primary destabilization mechanisms that describe the changes in the droplet size distribution. The first one is coalescence, which is caused when the continuous film between two emulsion droplets is ruptured, causing the two droplets to fuse together into one single larger droplet. The second mechanism is known as “Ostwald ripening”, which is a diffusive migration of dispersed phase in smaller droplets into bigger droplets driven by the differences in the Laplace pressures[4].

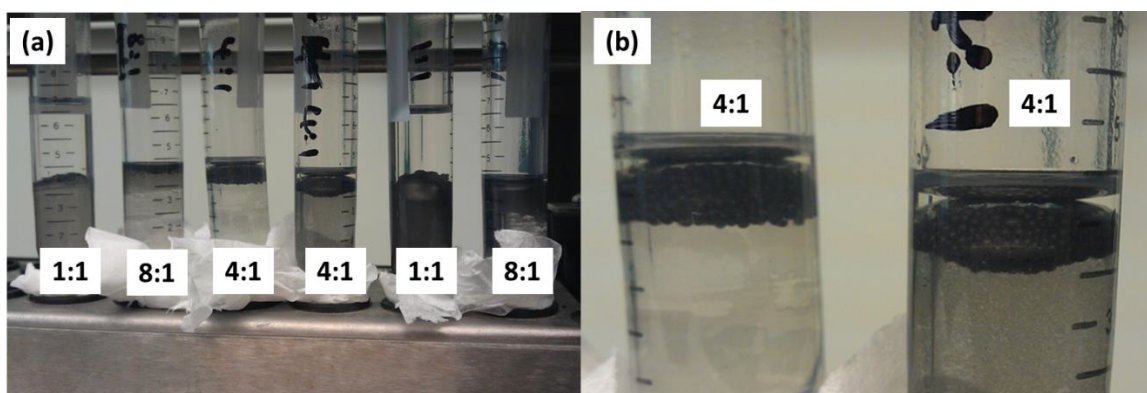
To form stable graphene stabilized oil (toluene) in water emulsions, two major parameters[5] (phase volume ratio and pH) governing the formation of stable emulsion were optimized. Most of anticancer drugs, such as camptothecin (CPT) and its derivatives[6] are only soluble in organic solvents.

It is essential to optimize the ratio of toluene to water to obtain the most stable emulsion. It has been reported that the type of emulsion is dependent on the relative volume of the two phases in the system[7, 8]. With an aim to encapsulate hydrophobic drugs, such as camptothecin (CPT) and its derivatives[6], that are only soluble in organic solvents. To achieve this, oil-in-water (O/W) emulsions are desired, thus the toluene volumes were always purposely kept less than that of the water phase. Figure 6.1 shows two trials of emulsion formation experiments with varied phase volume ratios done in parallel after a gentle mixing by vortex for 2 hours. It was obvious that 1:4 was the best ratio for emulsion formation, while the other two ratios resulted in self-assembled films of graphene at the interfaces. However, it should be noted that immediately after the mixing, all three mixtures exhibited spherical bubbles at the interface. The emulsion formed with 1:1 and 1:8 ratios were extremely instable against coalescence and ripening, and were completely broken and collapsed, leaving thin graphene films at the toluene/water interface. It was reported by Ostwald that if the phase volume ratios, which are generally accepted as water-to-oil ratios (WORs), were not optimized, the formed emulsion would be instable, and then break via coalescence[7, 8]. In most cases, when the WOR changes, the involvement of the amphiphilic species around the emulsion droplets would be



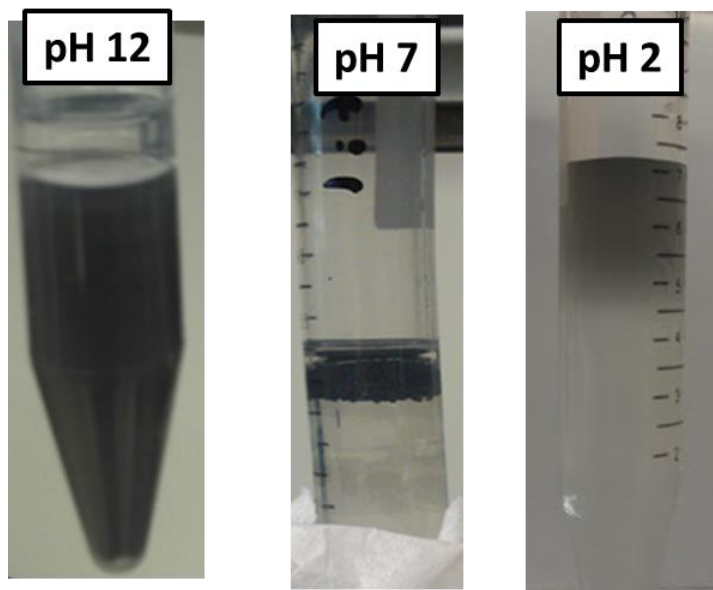
different due to the induced amphiphilicity-WOR coupling[9, 10]. If WOR is too small (1:1 in our case), the system now contains two bi-continuous phases, which are known to produce unstable emulsions,[11-13] because the interfacial tension between the toluene phase and the water phase is large, the formation of any interfacial curvatures is prohibited, resulting in a thin-film at the interface.

On the other hand, if the WOR is too large (8:1 in our case), the toluene phase required to form droplets for graphene sheets to go around becomes inadequate, causing a competitive environment for emulsion formation. The emulsion would be overpacked than it is possible for the continuous phase to stabilize it. The emulsion must result in breaking or collapsing[7, 8], resulting in critical phase separation. The formation of emulsion in a biphasic system confirms the amphiphilic nature of ME-LOGr.



**Figure 6.1:** Digital photographs of a) two trials of emulsion formation experiments with varied phase volume ratios done in parallel after a gentle mixing by vortex for 2 hours, and b) emulsion formed at 4:1 (water:toluene) ratio, showing stable and small emulsion bubbles at the toluene/water interface.

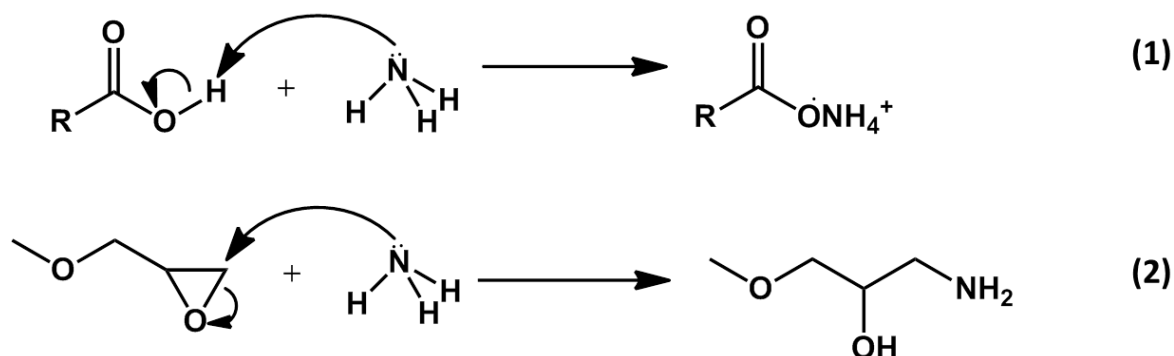
After discovering the optimized phase volume ratio to create stable emulsion, pH values were tuned since the amphiphilicity of graphene sheet is largely dependent on pH of the graphene solutions[2, 3]. The changing in pH has an effect in the degree of ionization of the -OH and -COOH groups on the surfaces of graphene. For example, at low pH values, -COOH and -OH groups are more protonated, graphene would be less charged, and hydrophobicity would dominate the surface property of graphene. In fact, when the pH was lowered to 2, all graphene was extracted into the toluene phase, leaving a clear and colorless water phase (figure 6.2 right). On the other hand, if the pH was increased, deprotonation of the functional groups is highly encouraged and the graphene should be more hydrophilic. Undoubtedly, when pH values were adjusted to 13, graphene was observed predominantly to stay in the aqueous phase, leaving the toluene phase clear. Interestingly, a thin film of a white cream-like substance was observed to be trapped and stabilized at the interface in between the two phases (see figure 6.2 left), which was indeed the microsphere found in microemulsions.[14, 15]



**Figure 6.2:** Effect of pH in emulsion formation.

It was surprising that a small amount of microspheres can be formed by simply adjusting the pH, and they are remarkably smaller than the emulsion formed at pH 7 (see figure 6.2 middle). It has been reported that GO can also form microsphere in basic ammonia water[16]. When GO (bearing  $\text{-COOH}$ ,  $\text{-OH}$ , and epoxy groups) solution is mixed with oil (toluene), due to its amphiphilic nature, the graphene would be supported by the oil/water interface and would self-assemble around the toluene droplets. There were two proposed mechanisms of the formation of stable graphene microspheres in aqueous ammonia (see scheme 6.1). Firstly, ammonia, which was used to adjust the pH of the solution, would interact with carboxylic acid groups on the edge of graphene as Bronsted acids, forming  $\text{NH}_4^+$  around  $\text{-COO}^-$ . Electrostatic interactions promote a formation of an interlocking system, holding the GO sheets together. On another

hand, the interaction between ammonia and epoxy would result in the formations of amine and phenol groups. These groups help graphene sheets to self-assemble into outer shells of microspheres via hydrogen bonding with the water molecules at the interface.



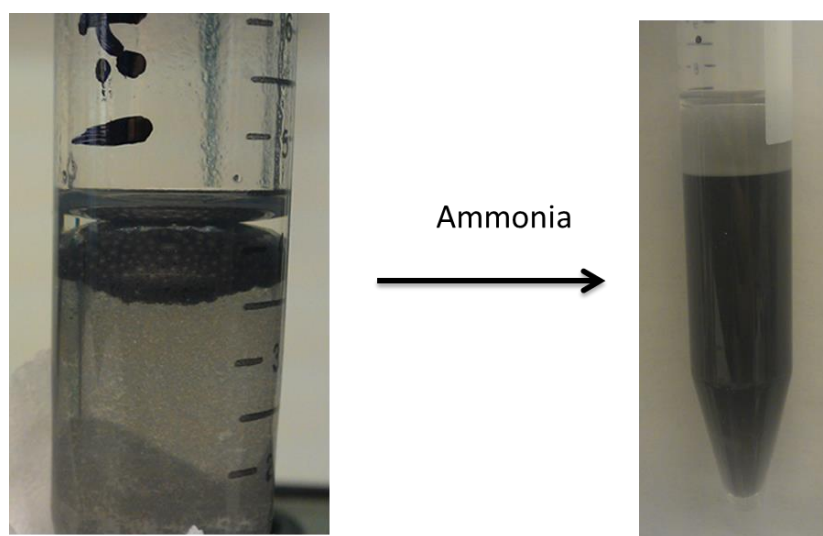
**Scheme 6.1:** Two proposed mechanisms of the formation of stable graphene microspheres in aqueous ammonia

### 6.2.2: Effect of sonication

There are many ways of preparing emulsions. Emulsification is usually achieved by some sort of mechanical energy. Stirring and vortexing have been the major methods in mixing and emulsifying two liquids that are immiscible.

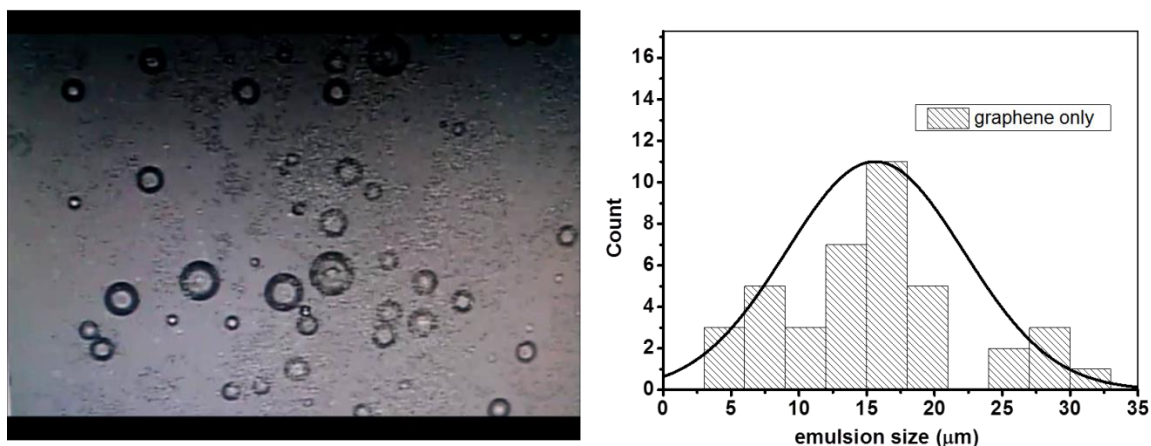
However, small droplet size at least in the micron scale is critical for drug delivery purposes. Among different emulsions, microemulsion and nanoemulsion spheres have been considered as carriers for pharmacological applications. These emulsions generally require energy input to be produced. Different methods have been introduced and studied at laboratory and industrial scale, including strong mechanical stirring, high-pressure homogenization and ultrasonication[17, 18].

We then chose ultrasonication as the high-shear energy input for the formation of smaller emulsion. Figure 6.3 shows the immediate differences in the microsphere sizes in the emulsion at pH 12 without (left) and with sonication (right), both pictures were taken at least 6 hours after emulsification to ensure the systems had reached equilibrium. With the aid of ultrasonication, cream-like emulsions spanned through the whole volumes of the biphasic system, and later on settle and lightly separate (figure 6.3).



**Figure 6.3:** Digital photographs showing the effect of the use of sonication for stable emulsion synthesis.

After reaching equilibrium, the formation of these sub-micron sized microsphere droplets are stable against breaking and collapsing for around a week. This is a main characteristic of Pickering emulsions which are stabilized by colloidal particles[19-23], suggesting that graphene acts as a colloidal surfactant[24]. The



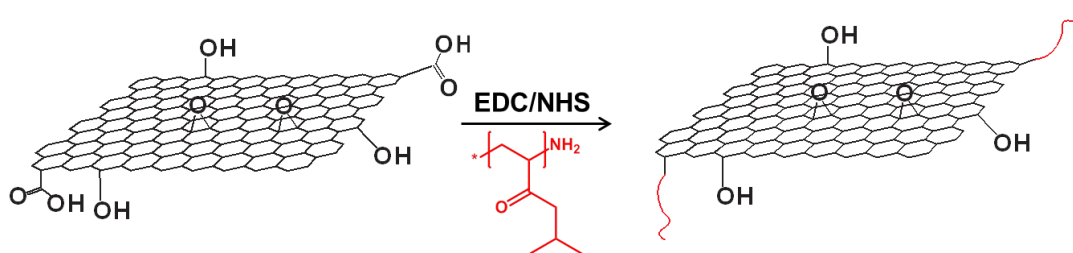
**Figure 6.4:** (left) A light micrograph of the emulsion stabilized by graphene; b) a plot of the distribution of sizes of the emulsion shown on the left

sizes of these microspheres were determined by light microscopy, as shown in figure 6.4, the images indicate that the microspheres had an average diameter of  $\sim 10 \mu\text{m}$ , however the sizes are poly-dispersed. It is also interesting to note that the microspheres became unstable against the light source of the light microscope, unlike the ones formed with GO.[15, 16] This instability could mainly be due to the fact that the graphene that made up these microspheres were only mildly oxidized, resulting in weak interlocking networks between the graphene sheets.

### 6.2.3: Modifying graphene with PNIPAM for improvement in stability and thermal-controllability

Inspired by the works that have recently been done to improve the properties of graphene by chemical modification , especially grafting of polymers onto

graphene to improve its solubility, interfacial activity and electronic properties, we studied the effect in stability and thermal stability on emulsions formed by the graphene grafted with a thermal-sensitive polymer, poly (*N*-isopropylacrylamide) (PNIPAM).



**Scheme 6.2:** Schematic showing the coupling of PNIPAM polymer onto the –COOH groups on the edge of graphene via EDC/NHS coupling reaction.

PNIPAM amine-terminated ( $M_n = \sim 2500$ ) was grafted onto graphene using EDC/NHS coupling reaction, [25, 26] as shown in scheme 6.2. An excess of PNIPAM polymer was used to ensure the complete consumption of the activated coupling species. After the coupling reaction reached completion, excess of free chemicals were removed by dialysis, resulting in a stable PNIPAM/graphene composite solution for emulsification. Similar to graphene-only suspension, the solution with PNIPAM-grafted graphene was also found to be extremely stable against precipitation forming homogenous suspension over a longer period of about two days.



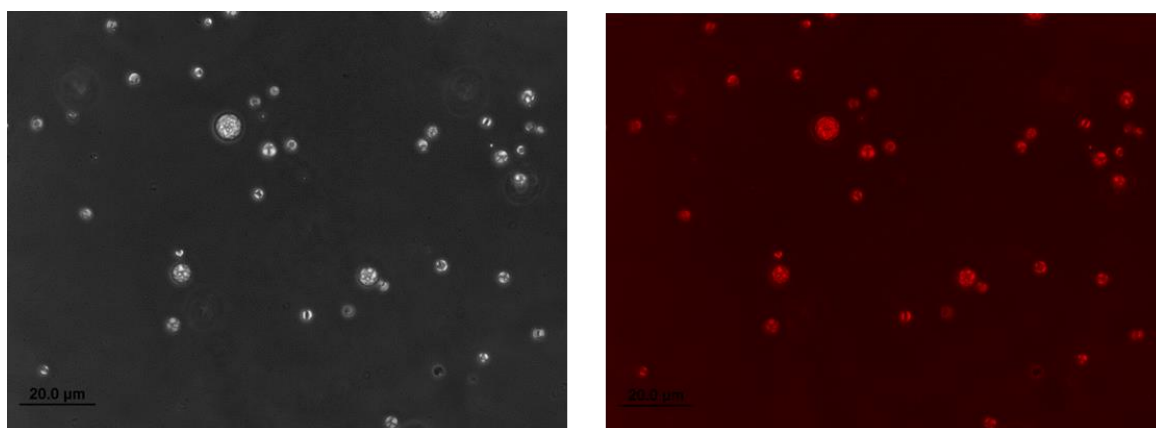
**Figure 6.5:** Emulsion prepared using ultrasonication at pH 13

Borrowing the optimized parameters optimized for the ME-LOGr described above, emulsion was prepared with PNIPAM/graphene composites at pH 13 with the aid of ultrasonication, as shown in figure 6.5. The emulsion showed a cream-like emulsion, similar to the one with ME-LOGr only. However, the amount of stable emulsion and the stability was much more improved. This could be due to the fact that PNIPAM itself can also act as Pickering emulsifiers in forming microspheres[27]. With the polymer backbone of the grafted PNIPAM interacting with each other around oil droplets, it provided a stronger network in the formed graphene/ PNIPAM shells, resulting in a more stable emulsion against collapsing.



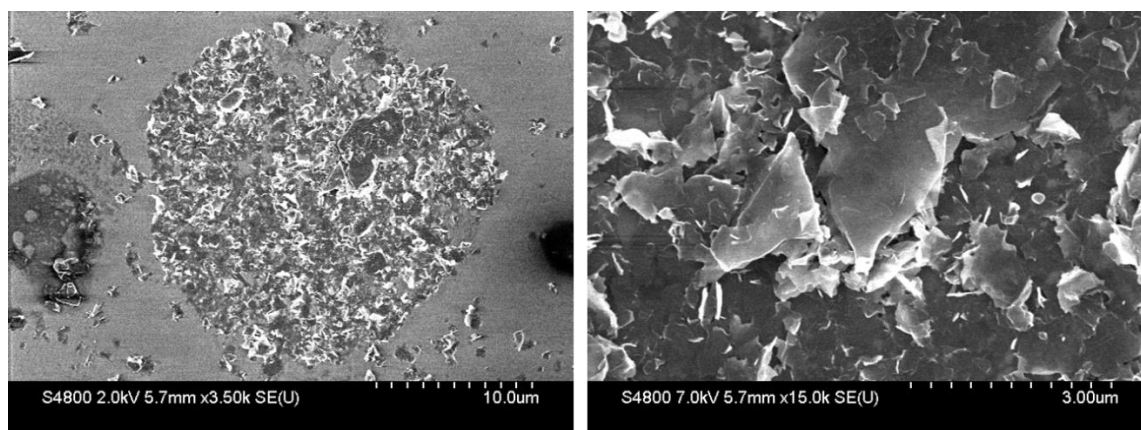
#### 6.2.4: Physical composition and morphological structures of microspheres

After studying the effects of phase volume ratio and the pH, and determining the best conditions to make a stable emulsion, the next step is to confirm the type of emulsion formed in this system. It was decided to dye the organic phase (toluene) using Oil Blue N (insoluble in water), because it enabled the observation of the encapsulations under fluorescence microscopes. In our case, if the microsphere cores contain oil droplets, the cores should fluoresce with a dark background. On the other hand, if the cores contain water-based droplet, the whole background with the dye should strongly fluoresce, leaving the microspheres to appear dark.



**Figure 6.6:** (Left) Regular optical image and (right) a typical fluorescence microscopic images of the emulsion microspheres. It clearly demonstrates a strong fluorescent signal from the microsphere cores, suggesting the encapsulation of the Oil Blue N dyed toluene

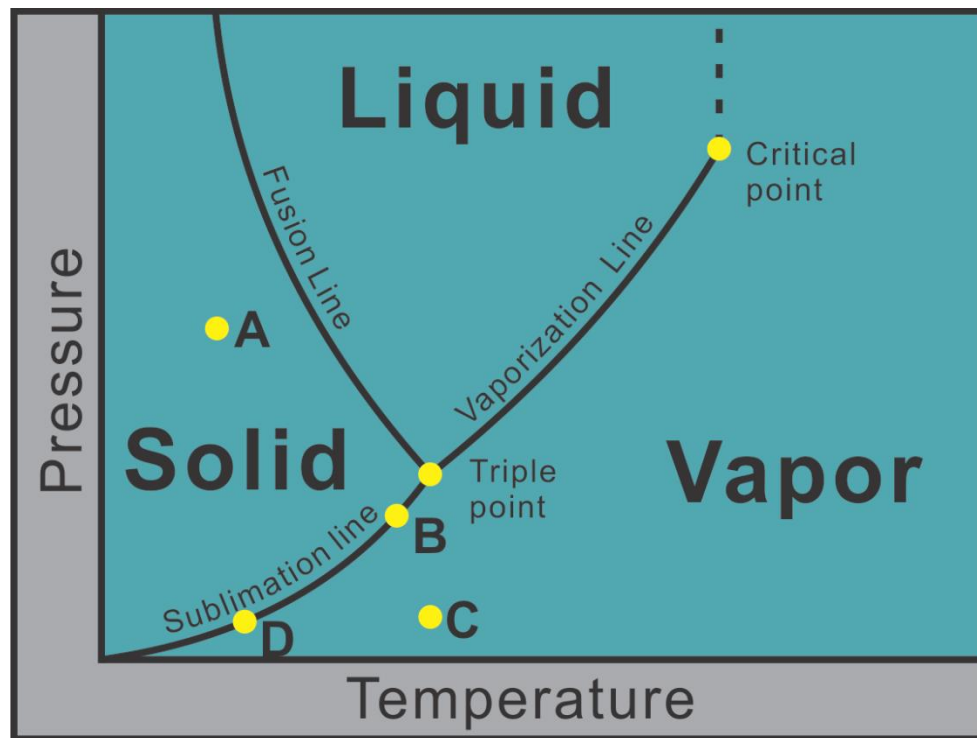
In figure 6.6, on the left is a regular optical and on the right is a typical fluorescence microscopic images of the emulsion microspheres. It clearly demonstrates a strong fluorescent signal from the microsphere cores, suggesting the encapsulation of the Oil Blue N dyed toluene within the microspheres protected with graphene shells. This result clearly evidenced that the emulsions were oil-in-water (O/W) emulsions. It is noteworthy that with the removal of all the free dye in the toluene phase, the large background signal in the images (Figure 6.6b) obtained from the fluorescence microscope was completely avoided, and the visibility of the emulsion was drastically improved.



**Figure 6.7:** a SEM image of the sample prepared by dropping and vacuum drying a volume of 10 uL of the emulsion on a Si substrate.

Scanning electron microscope (SEM) has been applied to characterize the microspheres prepared with the above mentioned parameters. Figure 6.7 shows a SEM image of the sample prepared by dropping and vacuum drying a volume of 10 uL of the emulsion on a Si substrate. It is obvious that all the microspheres

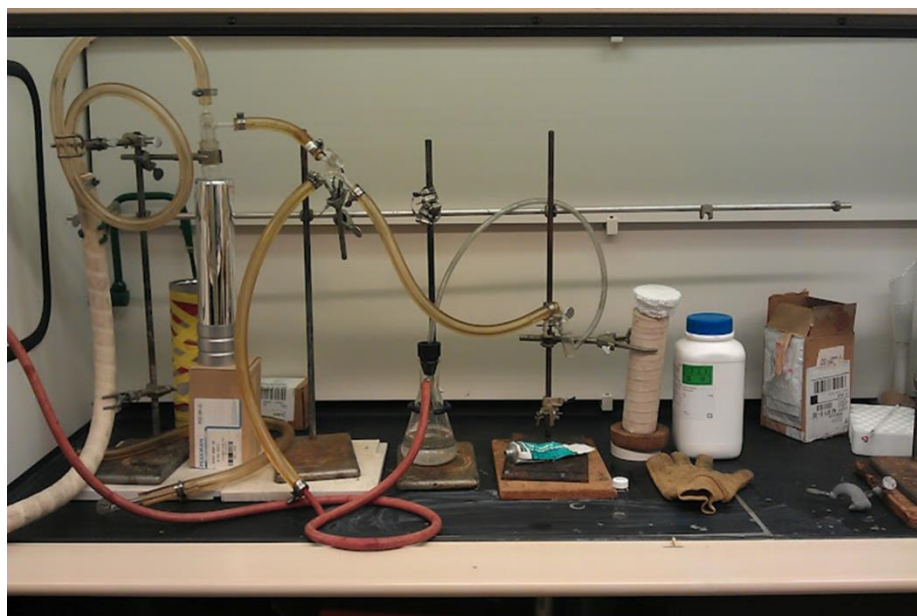
were deformed and collapsed due to the phase transition effect. Freeze-drying has been shown to have the ability to conserve the intact physical morphologies of the sample by eliminating the unnecessary phase transitions.



**Figure 6.8:** A typical phase diagram

By studying a typical phase diagram, shown in figure 6.8, to completely prevent samples from collapsing, the product should be frozen below its triple point down to the critical temperature (point B) under reduced pressure. After the product is frozen, high vacuum (1-5 torr) is applied to create an environment to allow sublimation to occur (from point B to point C). After a good vacuum had been established, slight heat can be input into the system to enhance the sublimation. It is also important to know that the vapor pressure of the product

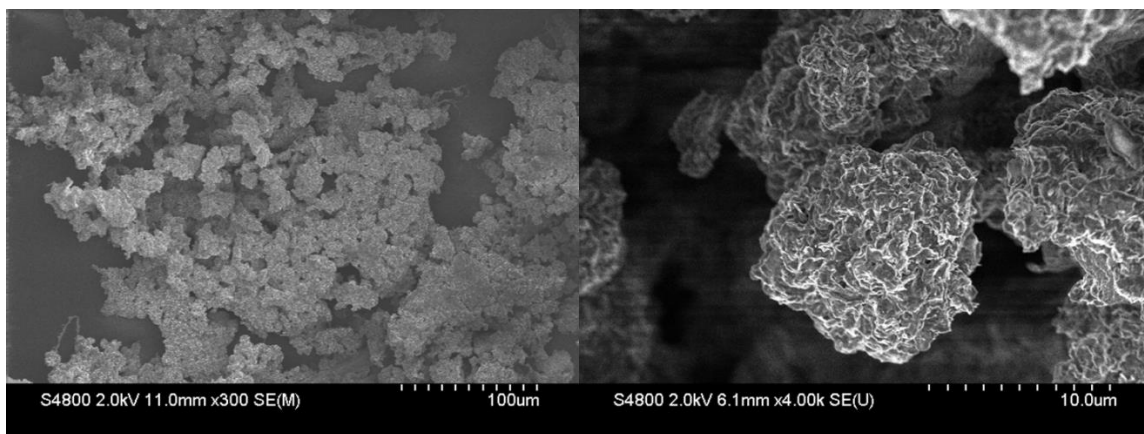
directly enhances the sublimation, thus a collector or a trap should be placed in significantly lowered temperature (point D). By understanding the theory behind freeze-drying, a home-built freeze-dryer is presented figure 6.9.



**Figure 6.9:** Photograph of the home-built freeze-drying apparatus.

Freeze-drying was confirmed to be able preserve the intact physical morphologies of the emulsion microsphere. The freeze-dried sample was characterized using SEM (figure 6.10). The emulsion samples collected with freeze-drying method are much more three-dimensional, confirming that the physical structures were preserved and intact. Microspheres exhibited a relatively rough, but spherical morphology, which is in agreement with others' findings. The rough surface morphology is due to the lack interaction between graphene sheets at the interface. Strong interactions through covalent bonding, hydrogen bonding and electrostatic forces have been shown to help formation of more

spherical microspheres[16]. This also indeed is evident that ME-LOGr graphene sheets are not heavily oxidized in the process.



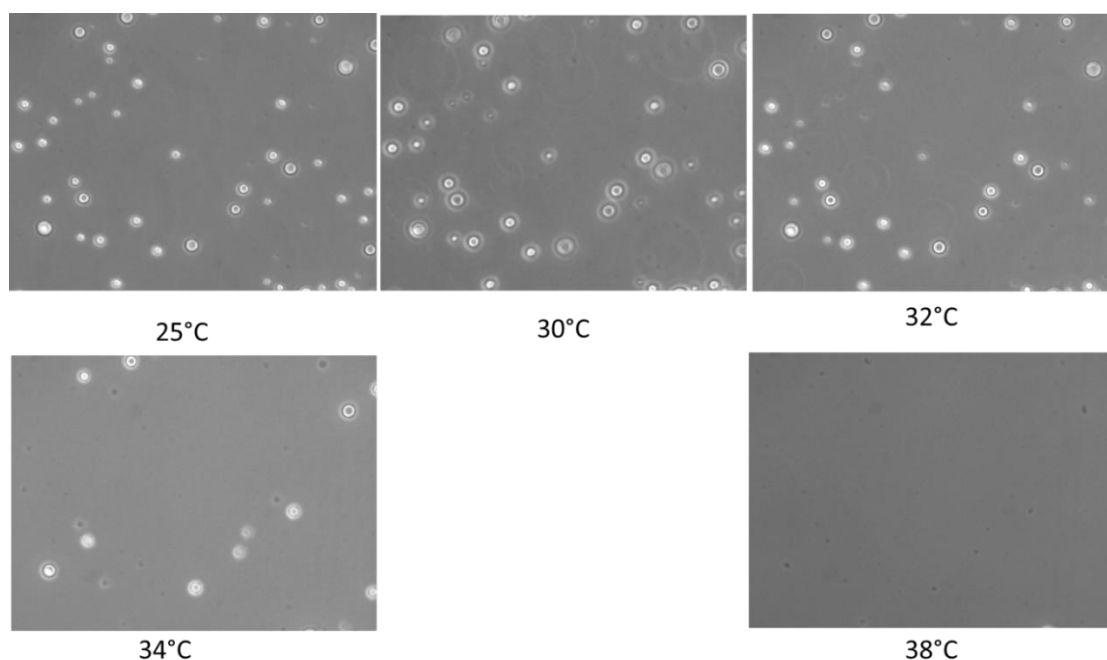
**Figure 6.10:** SEM images of the freeze-dried graphene-polymer sample,

### 6.2.5: Thermal Controlled release study

The dynamic thermo-responsive controlled release of Oil Blue N from emulsion microspheres was studied during a heating cycle. In each cycle, the environmental temperature was controlled using a warming plate, heating from room temperature to 38 °C. As a control experiment, we also studied the thermal-responsive controlled release behavior of PNIPAM only microspheres. In theory, when the environmental temperature is heated above the volume phase transition temperature (VPTT), PNIPAM undergoes a transition from being hydrophilic (swelling) to hydrophobic (shrinking).[28, 29] This swelling/shrinking behavior corresponds to the encapsulation/release behaviors of the drugs inside

the microspheres. In other words, the microsphere should encapsulate oil droplets below the VPTT but it should release the oil above the VPTT.

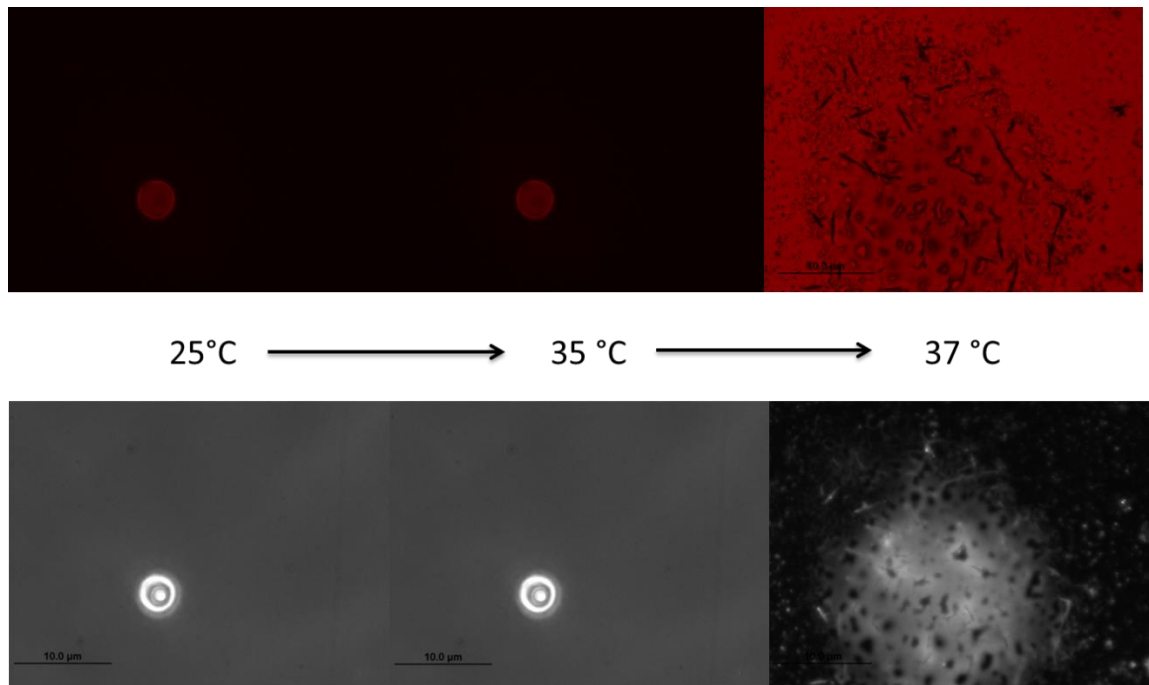
Figure 6.11 shows a series of light microscopic images of PNIPAM-only emulsion obtained at different temperatures. As shown, there was no visible change heating from 25 °C to 30 °C. However, when the emulsion was heated to about 32 °C, some small microspheres seem to have started to undergo phase transition releasing the oil droplets into the aqueous continuous phase, indicating that small microspheres were less stable than larger ones against heat. More



**Figure 6.11:** a series of light microscopic images of PNIPAM-only emulsion obtained at different temperatures.

dramatic release was seen when the emulsion was heated to 34 °C. At 38 °C no more microspheres were observed, indicating that a complete release had been

achieved. Compared to PNIPAM-only emulsion, PNIPAM/graphene emulsion showed an increase in the release temperature (see Figure 6.12). Top half of figure 6.12 shows the fluorescence images of a PNIPAM/graphene microsphere, and the bottom half shows the its corresponding light microscopic images. The fluorescence images once more confirmed the oil-in-water nature of the microsphere, showing that the reproducibility of O/W fabrications. As shown, it was surprising that the PNIPAM/graphene microsphere did not undergo phase transition, thus the release of the dye, until above 36 °C, which was about 4 °C higher than PNIPAM-only microspheres. This could be due to the fact that graphene itself is an excellent heat sink material and a good heat spreader[30, 31], and also that intact graphene sheets have been shown to have outstanding thermal conductivity. Thus, graphene sheets served a role as the temperature



**Figure 6.12:** (Top) Fluorescence images of a PNIPAM/graphene microsphere, and (bottom) their corresponding light microscopic images at different temperatures.

quencher around the emulsion oil droplet, keeping PNIPAM from undergoing the phase transition from swelling to shrinking at its VPTT ( $\sim 32$  °C) by increasing it to  $\sim 36$  °C. It is important to mention that with the aid of graphene, PNIPAM/graphene microsphere can now be stabilized up to  $\sim 36$  °C, which is very close to the physiological temperature. It is believed that these microspheres can be used in any application that requires drugs to be released with a slight increase in the body temperature, such as inflammations and fever.

### 6.3: CONCLUSION:

In summary, we have successfully demonstrated that ME-LOGr can be used as an amphiphilic colloidal surfactant that can adsorb at the interface in a biphasic system. By tuning the phase volume ratio and pH values, this amphiphilic surfactant can form Pickering emulsions with organic solvent droplets surrounded by water. Freeze-drying was found to be required to preserve the integrity of the physical morphology when drying is needed. A thermal-responsive polymer, PNIPAM, was used to enhance the stability of the emulsion. Emulsion formed by PNIPAM/graphene composite increased its VPTT from  $32$  °C to  $\sim 36$  °C, which opened a new path for developing drug delivery systems that require the release of drugs at the physiological temperature.



## **6.4: MATERIALS AND METHODS:**

### **6.4.1: Materials:**

Ammonia, Poly(*N*-isopropylacrylamide) amine terminated (PNIPAM) with an average molecular weight ( $M_w$ ) of 2500 Dalton, 1-Ethyl-3-[3-dimethylaminopropyl] carbodiimide hydrochloride (EDC), *N*-hydroxysulfosuccinimide (NHS) and Oil Blue N (97% dye content) were purchased from Sigma-Aldrich and were used as-received. Toluene (ACS grade) was purchased from Pharmco and was used as-received. All solutions were prepared using deionized water (18.2 M $\Omega$ ) (Nanopure water, Barnstead). For composite purification, Amicon Centrifugal Filter Units (Millipore) of molecular weight cut off 8000 Da were used. The homogenizer used for the emulsion formation steps was a Sonics VC130 probe-tip sonicator (2mm tip; 45% amplitude). To modify the pH, ~1 M NH<sub>4</sub>OH and ~1 M HCl solutions were used.

### **6.4.2: Methods:**

#### **6.4.2.1: Synthesis of graphene**

ME-LOGr was synthesized as described previously[1]. In short, 20 mg of graphite was added in to a mixture of sulfuric acid and nitric acid (1:1) and was subjected to 30 seconds of microwave irradiation. The graphene product was then filtered and was extensively washed with water. Finally, the collected purified product was re-suspended into water using bath sonication for 30 mins.

#### **6.4.2.2: Synthesis of PNIPAM/graphene composite via EDC/NHS coupling reaction**

To covalently graft PNIPAM onto graphene sheets, EDC/NHS coupling reaction was carried out to link polymers with  $\text{-NH}_2$  groups in the polymer with the  $\text{-COOH}$  groups on the edges of graphene sheets *via* peptide bonds.

In a general EDC/NHS coupling reaction (Note: Fresh solutions were prepared prior to each reaction), 10 mL graphene solution with a concentration of  $\sim 70\text{-}90$  mg/L was mixed and vortexed for 1 hour with 3.2 mg of EDC and 8 mg of NHS to form an amine-reactive *O*-acylisourea intermediate. After an hour, the amine-terminated PNIPAM was added and was vortexed for two hours for the coupling reaction. After the reaction has completed, free reagents and free polymer molecules were extensively dialyzed using Amicon units (MWCO = 8 kDa) against deionized water, resulting in graphene/PNIPAM composite solution.

#### **6.4.2.3: The preparation of O/W emulsion**

To prepare oil-in-water (O/W) emulsion, 4 mL of stable graphene suspension was pipetted into a polyethylene centrifuge tube, followed by 1 mL of toluene. This mixture was then mixed vigorously with a horn-sonicator for 1 minute at amplitude of 40%. The resulting creamy emulsions were left undisturbed for 4-6 hours before removed for any other experiments.

#### **6.4.2.4: Optimization of emulsion formations**

The stabilities of the emulsion formed were studied against the pH of graphene solution and graphene solution to toluene phase volume fractions. In brief, the ratio of 2:1, 4:1 and 8:1 were accordingly adjusted using 4 mL of the aqueous graphene solution. pH values of 2 and 12 were adjusted using diluted HCl (1 M) and ammonia (1 M).

#### **6.4.2.5: Enhanced stability of graphene emulsion by crosslinking with PNIPAM**

4 mL of PNIPAM/graphene solution at about 70-90 mg/L of graphene was used for each emulsion and the pH of the solution was adjusted to pH 12 using ammonia and was thoroughly mixed. Then, 1 mL of toluene was added on top of the aqueous phase. This mixture was then treated with a cup-horn sonicator for two minutes at 40% amplitude in an ice-bath with an aim not to let the thermal sensitive polymer to undergo phase transition in the hot cavitation bubble generated by the ultrasound[32]. As this biphasic system was sonicated, an emulsion with a milky appearance was observed, confirming formation of emulsion system with small microspheres.

#### **6.4.2.6: Characterization of morphological O/W emulsion microstructure:**

Emulsion microspheres prepared using the optimized conditions were characterized for size and morphology by scanning electron microscope (SEM), and both optical and fluorescence microscopy.

The emulsion specimen for SEM studies were frozen rapidly in liquid nitrogen and freeze-dried for more than 5 hours. The freeze-dried samples were scrapped off the container and were directly deposited onto the carbon tape for SEM investigation. The microstructures were observed using SEM (Hitachi S-4800) at an accelerating voltage of 5 kV and a probe current at 20  $\mu$ A. Fluorescence microscopy was utilized to determine the type of the emulsion of the sample and to study the capability to thermally controlled release the encapsulated dyes. (see below). First, the organic phase (toluene) was dyed using Oil Blue N at a concentration of about  $\sim$ 4 mg/L with the aid of 10 minutes of sonication. The emulsion was then directly observed under an Olympus IX81 fluorescence microscope and the fluorescent measurements were taken using 485 nm excitation and 535 nm emission wavelengths.

#### **6.4.2.7: Characterization of thermo-responsive behaviors of the composites and controlled release experiment.**

Fluorescent images of during the dynamic thermo-responsive release process were studied also under the same Olympus IX81 microscope, but equipped with a thermostatic stage with a temperature control unit (TokaiHit, Inc, Japan; HeatPlate MATS-U55R30). Freshly prepared emulsion dyed with Oil Blue N (see above) at a concentration of 4 mg/L of the dye in toluene was found to be

adequate enough for the visualization of the encapsulation and release study. At the beginning of the observation, the concentrated emulsion was diluted in deionized water and the diluted dyed emulsion samples were placed inside different chambers and were placed on top of the heating plate then was heated from 23 °C to 38 °C. Images were taken at a scanning rate of 2 s per image.

## 6.5: REFERENCES:

1. Chiu, P.L., Mastrogiovanni, D.D., Wei, D., Louis, C., Jeong, M., Yu, G., Saad, P., Flach, C.R., Mendelsohn, R., Garfunkel, E., and He, H., *Microwave- and nitronium ion-enabled rapid and direct production of highly conductive low-oxygen graphene*. J Am Chem Soc, 2012. **134**(13): p. 5850-6.
2. Kim, F., Cote, L.J., and Huang, J., *Graphene oxide: surface activity and two-dimensional assembly*. Adv Mater, 2010. **22**(17): p. 1954-8.
3. Kim, J., Cote, L.J., Kim, F., Yuan, W., Shull, K.R., and Huang, J., *Graphene oxide sheets at interfaces*. J Am Chem Soc, 2010. **132**(23): p. 8180-6.
4. Taylor, P., *Ostwald ripening in emulsions: estimation of solution thermodynamics of the disperse phase*. Adv Colloid Interface Sci, 2003. **106**: p. 261-85.
5. M. Bourrel, R.S.S., *Microemulsions and Related Systems: Formulation, Solvency, and Physical Properties*. Surfactant Science Series. Vol. 11. 1988, New York: Marcel Dekker, Inc.; New York and Basel. nil + 483.
6. Muggia, F.M., Dimery, I., and Arbuck, S.G., *Camptothecin and its analogs. An overview of their potential in cancer therapeutics*. Ann N Y Acad Sci, 1996. **803**: p. 213-23.
7. Ostwald, W., Kolloid-Zeitschrift, 1910. **6**: p. 103-109.
8. Ostwald, W., Kolloid-Zeitschrift, 1910. **7**: p. 64.
9. Graciaa, A., Anderez, J., Bracho, C., Lachaise, J., Salager, J.L., Tolosa, L., and Ysambertt, F., *The selective partitioning of the oligomers of polyethoxylated surfactant mixtures between interface and oil and water bulk phases*. Adv Colloid Interface Sci, 2006. **123-126**: p. 63-73.
10. Graciaa, A., Lachaise, J., Sayous, J.G., Grenier, P., Yiv, S., Schechter, R.S., and Wade, W.H., *The partitioning of complex surfactant mixtures between oil/water/microemulsion phases at high surfactant concentrations*. J Colloid Interface Sci, 1983. **93**(2): p. 474-486.
11. Binks, B.P., Cho, W.G., Fletcher, P.D.I., and Petsev, D.N., *Stability of Oil-in-Water Emulsions in a Low Interfacial Tension System*. Langmuir, 1999. **16**(3): p. 1025-1034.

12. Bourrel, M., Graciaa, A., Schechter, R.S., and Wade, W.H., *The relation of emulsion stability to phase behavior and interfacial tension of surfactant systems*. J Colloid Interface Sci, 1979. **72**(1): p. 161-163.
13. Salager, J.L., Quintero, L., Ramos, E., and Anderez, J., *Properties of surfactant/oil/water emulsified systems in the neighborhood of the three-phase transition*. J Colloid Interface Sci, 1980. **77**(1): p. 288-289.
14. Liang, F., Shen, K., Qu, X., Zhang, C., Wang, Q., Li, J., Liu, J., and Yang, Z., *Inorganic Janus nanosheets*. Angew Chem Int Ed Engl, 2011. **50**(10): p. 2379-82.
15. Liang, F., Liu, J., Zhang, C., Qu, X., Li, J., and Yang, Z., *Janus hollow spheres by emulsion interfacial self-assembled sol-gel process*. Chem Commun (Camb), 2011. **47**(4): p. 1231-3.
16. Guo, P., Song, H., and Chen, X., *Hollow graphene oxide spheres self-assembled by W/O emulsion*. Journal of Materials Chemistry, 2010. **20**(23): p. 4867-4874.
17. Jafari, S.M., Assadpoor, E., He, Y., and Bhandari, B., *Re-coalescence of emulsion droplets during high-energy emulsification*. Food Hydrocolloids, 2008. **22**(7): p. 1191-1202.
18. Landfester, K., Tiarks, F., Hentze, H.-P., and Antonietti, M., *Polyaddition in miniemulsions: A new route to polymer dispersions*. Macromolecular Chemistry and Physics, 2000. **201**(1): p. 1-5.
19. Pickering, S.U., *CXCVI.-Emulsions*. Journal of the Chemical Society, Transactions, 1907. **91**: p. 2001-2021.
20. Velev, O.D., Furusawa, K., and Nagayama, K., *Assembly of Latex Particles by Using Emulsion Droplets as Templates. 1. Microstructured Hollow Spheres*. Langmuir, 1996. **12**(10): p. 2374-2384.
21. Kutuzov, S., He, J., Tangirala, R., Emrick, T., Russell, T.P., and Boker, A., *On the kinetics of nanoparticle self-assembly at liquid/liquid interfaces*. Phys Chem Chem Phys, 2007. **9**(48): p. 6351-8.
22. Boker, A., He, J., Emrick, T., and Russell, T.P., *Self-assembly of nanoparticles at interfaces*. Soft Matter, 2007. **3**(10): p. 1231-1248.
23. Aveyard, R., Binks, B.P., and Clint, J.H., *Emulsions stabilised solely by colloidal particles*. Advances in Colloid and Interface Science, 2003. **100-102**(0): p. 503-546.

24. Kim, J.-W., Lee, D., Shum, H.C., and Weitz, D.A., *Colloid Surfactants for Emulsion Stabilization*. Advanced Materials, 2008. **20**(17): p. 3239-3243.
25. Olde Damink, L.H., Dijkstra, P.J., van Luyn, M.J., van Wachem, P.B., Nieuwenhuis, P., and Feijen, J., *Cross-linking of dermal sheep collagen using a water-soluble carbodiimide*. Biomaterials, 1996. **17**(8): p. 765-73.
26. Nam, K., Kimura, T., and Kishida, A., *Preparation and characterization of cross-linked collagen-phospholipid polymer hybrid gels*. Biomaterials, 2007. **28**(1): p. 1-8.
27. Tsuji, S. and Kawaguchi, H., *Thermosensitive pickering emulsion stabilized by poly(N-isopropylacrylamide)-carrying particles*. Langmuir, 2008. **24**(7): p. 3300-5.
28. Wu, C., *A comparison between the 'coil-to-globule' transition of linear chains and the "volume phase transition" of spherical microgels*. Polymer, 1998. **39**(19): p. 4609-4619.
29. Wu, J., Zhou, B., and Hu, Z., *Phase Behavior of Thermally Responsive Microgel Colloids*. Phys Rev Lett, 2003. **90**(4): p. 048304.
30. Balandin, A.A., Ghosh, S., Bao, W., Calizo, I., Teweldebrhan, D., Miao, F., and Lau, C.N., *Superior thermal conductivity of single-layer graphene*. Nano Lett, 2008. **8**(3): p. 902-7.
31. Jang, W., Chen, Z., Bao, W., Lau, C.N., and Dames, C., *Thickness-dependent thermal conductivity of encased graphene and ultrathin graphite*. Nano Lett, 2010. **10**(10): p. 3909-13.
32. Suslick, K.S., *Sonochemistry*. Science, 1990. **247**(4949): p. 1439-45.



## CURRICULUM VITA

### Pui Lam Chiu

**Date of Birth**            October 13<sup>th</sup>, 1981

**Birth Place**            Hong Kong

#### Education:

Ph. D. in Chemistry, Rutgers University, 2012  
Mentor: Professor Huixin He

B.S. in Chemistry, Rutgers University, 2006

#### Publications:

1. In situ fabrication of a water-soluble, self-doped polyaniline nanocomposite: the unique role of DNA functionalized single-walled carbon nanotubes  
Yufeng Ma, Shah R Ali, Ling Wang, **Pui Lam Chiu**, Richard Mendelsohn, Huixin He  
*Journal of the American Chemical Society* 128 (37), 12064-12065
2. The electronic role of DNA-functionalized carbon nanotubes: efficacy for in situ polymerization of conducting polymer nanocomposites  
Yufeng Ma, **Pui Lam Chiu**, Arnaldo Serrano, Shah R Ali, Alex M Chen, Huixin He  
*Journal of the American Chemical Society* 130 (25), 7921-7928
3. Improved conductivity of carbon nanotube networks by in situ polymerization of a thin skin of conducting polymer  
Yufeng Ma, William Cheung, Dongguang Wei, Albert Bogozzi, **Pui Lam Chiu**, Lin Wang, Francesco Pontoriero, Richard Mendelsohn, Huixin He  
*ACS nano* 2 (6), 1197-1204
4. Photosensitized singlet oxygen production upon two-photon excitation of single-walled carbon nanotubes and their functionalized analogues

Naveen Gandra, **Pui Lam Chiu**, Wenbing Li, Yolanda R Anderson,  
Somenath Mitra, Huixin He, Ruomei Gao  
*The Journal of Physical Chemistry C* 113 (13), 5182-5185

5. Fabrication of high performance conducting polymer nanocomposites for biosensors and flexible electronics: summary of the multiple roles of DNA dispersed and functionalized single walled carbon nanotubes  
William Cheung, **Pui Lam Chiu**, Rishi R Parajuli, Yufeng Ma, Shah R Ali, Huixin He  
*J. Mater. Chem.* 19 (36), 6465-6480
6. Production of Graphene Sheets by Direct Dispersion with Aromatic Healing Agents  
Ming Zhang, Rishi R Parajuli, Daniel Mastrogiovanni, Boya Dai, Phil Lo, William Cheung, Roman Brukh, **Pui Lam Chiu**, Tao Zhou, Zhongfan Liu, Eric Garfunkel, Huixin He  
*Small* **2010**, 6 (10), 1100-1107
7. Microwave and Nitronium Ion Enabled Rapid and Direct Production of Highly Conductive Low Oxygen Graphene  
**Pui Lam Chiu**, Daniel DT Mastrogiovanni, Dongguang Wei, Cassandre Louis, Min Jeong, Guo Yu, Peter Saad, Carol R Flach, Richard Mendelsohn, Eric Garfunkel, Huixin He  
*Journal of the American Chemical Society* **2012**, 134 (13), pp 5850–5856